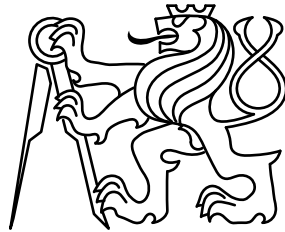


CZECH TECHNICAL UNIVERSITY IN PRAGUE

Faculty of Electrical Engineering
Department of Electromagnetic Field



Doctoral Thesis

Microwave Methods for Interferometric Measurements

Milan Příhoda

Ph.D. Programme: **Electrical Engineering and Information Technology**

Branch of study: **Radioelectronics**

Supervisor: **prof. Ing. Karel Hoffmann, CSc.**

Supervisor-Specialist: **doc. Ing. Přemysl Hudec, CSc.**

Prague, May 2016

Acknowledgement

I would like to sincerely thank to my supervisor Karel Hoffmann and to all colleagues at the Department of Electromagnetic Field for important advices and exciting discussions related to the microwave measurements which were substantial for my work.

Declaration

I declare that I worked out the presented thesis independently and I quoted all used sources of information in accord with Methodical instructions about ethical principles for writing academic thesis.

Abstract

Interferometrická mikrovlnná měření mohou najít uplatnění v celé řadě aplikací jako jsou měření malých fázových rozdílů, měření vysokých impedancí nebo nedestruktivní testování. Ačkoliv jsou interferometrická měření dobře známá například z optiky, v mikrovlnné technice mají svá specifika.

Jak ukazují různé práce publikované v nedávné době, je zde několik nevyřešených problémů týkající se interferometrických měření. Jedním z takových problémů je přítomnost systematických chyb, která je v řadě prací opomíjena a systémy jsou považovány za ideální. S tím souvisí i fakt, že nebyly vyvinuty vhodné kalibrační techniky a vhodné kalibračních standardy pro taková měření. V případě přesného měření fází zcela chybí metodika pro absolutní měření, protože doposud publikované práce používaly interferometrické systémy jen pro relativní měření.

Cílem této disertační práce je vyřešit problém absolutního měření pro přesné měření fází, analyzovat systematické chyby použitých systémů a navrhnout vhodnou kalibrační/korekční techniku pro odstranění těchto systematických chyb.

Tyto cíle jsou v práci systematicky řešeny, od základních rozborů a analýz systémů s idealizovanými parametry, přes rozbor systematických chyb, díky němuž bylo možné navrhnout zcela speciální kalibrační techniku, která využívá frekvenčně závislých modelů pro kalibrační standardy a vyhodnocuje měřená data přes celé kmitočtové pásmo zároveň narozdíl od běžných kalibračních technik.

Navržená kalibrační technika byla experimentálně ověřena pomocí interferometrického systému ve frekvenčním pásmu $8 \div 10$ GHz. Výsledky prokázaly, že navržená technika umožňuje kalibraci interferometrického systému pro přesné měření fází. Dále bylo ukázáno, že nejhorší případ nejistoty měření s takto zkalibrovaným systémem je téměř dvakrát menší v porovnání s přímým měřením pomocí vektorového obvodového analyzátoru.

Klíčová slova

Interferometrické měření, měření fází, kalibrační techniky, vektorový obvodový analyzátor

Abstract

The microwave interferometric measurements can be used in the several applications such as measurement of the small phase differences, measurement of the extreme impedances or near-field sensing. Although the interferometric measurements are well-known from the optics but there are specific aspects of such a measurement in the microwaves.

As was shown in the recently published works, there are several problems regarding these measurements, which haven't been solved yet. One of the problems is the existence of the systematic errors which were in the most cases completely neglected and the interferometric system was assumed as ideal. It is very closely related to the fact that there is no suitable calibration technique as well as calibration standards for such a systems. Finally, for the case of precise phase measurement or measurement of small phase differences there is lack of the method for the absolute measurement. Works published until now utilized interferometric measurement only for the relative phase measurement.

The main aim of this thesis is to find an approach for the absolute measurement of the phase, to analyze the effect of the systematic errors and to design a suitable calibration technique to eliminate these systematic errors.

These goals are successively analyzed and solved. Starting with the analysis of the idealized systems through the systematic errors analysis which helped to design new calibration technique, which utilize the parametric frequency dependant model and moreover contrary to the ordinary calibration techniques it evaluate the measured data simultaneously over the entire bandwidth.

This technique was experimentally verified using the interferometric system in the frequency range $8 \div 10$ GHz. The results prove that the proposed technique enables the precise interferometric measurement of the phase. Additionally it was shown that the worst case of the uncertainty using the calibrated interferometric system is roughly twice smaller in comparison with the direct VNA measurement.

Keywords

Interferometric measurements, phase measurements, calibration techniques, vector network analyzer

Contents

1. Introduction	1
2. Current state-of-the-art	3
2.1. Measurement of high and low impedances	3
2.2. Near field sensing – scanning microwave microscopy	5
2.3. Distance measurement	7
2.4. Thesis objectives	10
3. Uncertainty analysis	11
3.1. Measurement of the phase of the reflection coefficient	11
3.2. Uncertainty of an interferometric measurement	14
4. Interferometric measurements	18
4.1. 180° Interferometer – ideal case	19
4.1.1. Phase measurement using interferometer	21
Perfect match in the test or reference channel	22
Condition for interference	22
4.1.2. Terminating impedance	26
4.1.3. Effects of the finite frequency step size	28
4.1.4. Sensitivity analysis	30
4.2. Ideal 90° interferometer	34
4.3. Ideal 3dB divider interferometer	36
4.4. Non-ideal hardware	37
4.4.1. The full 16-term model	38
4.4.2. The reciprocal model with omitted reflections	39
4.4.3. Influence of parasitic terms to the result	40
5. System calibration	44
5.1. Model based auto-calibration	45
5.2. Experimental verification	47
5.2.1. The results obtained by idealized approach	51
5.2.2. The results obtained using proposed calibration technique	53
5.2.3. Summary	59
6. Conclusion	60
6.1. Additional remarks and the future work	61
6.2. Authored and co-authored results dealing with the topic of the dissertation	61
6.3. Other authored or co-authored and published results	61
Bibliography	63
A. Appendix	67
A.1. 16-term model of an four port interferometer	67
A.2. Measured parameters of the WR90 interferometer (180° hybrid coupler)	69
A.3. Measured S-parameters for each setup	72

A.4. Calibration results	79
B. List of candidates's works relating to the doctoral thesis	82
B.1. Publications in impacted journals	82
B.2. Publications in WOS database	82
B.3. Peer-reviewed publications	82
B.4. Other publications	82
B.5. Responses and citations	82

Abbreviations

VNA	Vector network analyzer
DUT	Device under test
SMM	Scanning microwave microscope / scanning microwave microscopy
AFM	Atomic force microscope
S-parameters	Scattering parameters
RBW	Resolution bandwidth filter
TEM	Transverse electromagnetic mode
TE	Transverse electric mode

List of Figures

2.1. Arrangement of the measurement system – ideal components [11].	3
2.2. The principle of Agilent’s SMM [24].	5
2.3. Interferometric setup using a 3 dB power divider [7].	6
2.4. Interferometric setup using a hybrid coupler [8].	6
2.5. Microwave interferometric system for distance measurement according to [17].	7
2.6. S_{21} measurement of the interferometric system. The frequency of the minimum depends on the measured distance [17].	8
2.7. The dependence of the distance on the cancellation frequency. Measured vs expected trace [17].	9
2.8. Microwave interferometric system for the distance measurement according to [17].	9
3.9. Rohde&Schwarz ZVA-67 Vector Network Analyzer.	11
3.10. Measurement scenario. A two transmission lines with different length, connected to the VNA and terminated by an impedance Z_L which is close to short circuit.	13
3.11. Phase of S_{11} parameter for both lines including uncertainty regions.	13
3.12. Smith chart with S_{11} parameter for both lines including uncertainty regions. .	14
3.13. Measurement scenario with an ideal interferometric extender connected the VNA.	15
3.14. Expected values assuming ideal interferometer.	15
3.15. Smith chart with selected frequency points of the S_{21} parameter measured by the interferometric system including uncertainty regions.	16
3.16. Smith chart with selected frequency points of the S_{21} parameter measured by the interferometric system including uncertainty regions.	16
3.17. Example of phase to magnitude measurement conversion using an interferometric setup. Each color represents measurement of the same DUT	17
4.1. Interferometric setup with a homogeneous line as a DUT.	18
4.2. Interferometer approach using 180° hybrid coupler	19
4.3. An example of phase-to-magnitude measurement conversion using an interferometric setup. Each color represents measurement of the same DUT	20
4.4. Interferometer approach using 180° hybrid coupler	21
4.5. Vectors of waves from the <i>test</i> (blue) and <i>reference</i> (green) channels in the left figure, measured $ S_{21} $ trace in the right.	23
4.6. Two DUTs different in the phase measured using interferometer setup with 180° hybrid coupler	24
4.7. Vectors of waves from the <i>test</i> (blue) and <i>reference</i> (green) channels in the left figure, measured $ S_{21} $ trace in the right. The case when the vectors differs more then one wavelength.	24

4.8. Vectors of waves from the <i>test</i> (blue) and <i>reference</i> (green) channels in the left figure, measured $ S_{11} $ trace in the right.	25
4.9. Vectors of waves from the <i>test</i> (blue) and <i>reference</i> (green) channels in the left figure, measured $ S_{11} $ trace in the right. The case when the vectors differs more then one wavelength.	26
4.10. Effect of the reflection magnitude in the <i>test</i> and <i>reference</i> channel.	26
4.11. Effect of the reflection magnitude in <i>reference</i> channel for the case when the $\Gamma_T = 0.6$	27
4.12. Circuit diagram in the CST Design Studio.	28
4.13. $ S_{21} $ obtained from the simulation with an ideal 180° hybrid coupler.	29
4.14. $ S_{11} $ obtained from the simulation with an ideal 180° hybrid coupler.	30
4.15. Two identical measurements with very small phase change in the <i>test channel</i>	31
4.16. $ S_{21} $ traces showing the frequency of the minima due to small phase change in the <i>test channel</i>	31
4.17. $ S_{21} $ simulated in CST Design Studio assuming an ideal system. The $\delta\Delta l = 100 \mu\text{m}$	32
4.18. $ S_{21} $ simulated in CST Design Studio assuming an ideal system. The $\delta\Delta l = 100 \mu\text{m}$	32
4.19. Circuit diagram in the CST Design Studio.	34
4.20. $ S_{11} $ and $ S_{21} $ obtained from the simulation with an ideal 90° hybrid coupler.	34
4.21. Circuit diagram in the CST Design Studio.	36
4.22. $ S_{11} $ obtained from the simulation with an ideal 3 dB divider.	36
4.23. Measurement scenario with the non-ideal system where all parasitic terms are present.	37
4.24. Flow graph for the full 16-term model of the interferometer.	38
4.25. Flow graph for the reciprocal model with omitted reflections	40
4.26. Circuit simulation in CST Design Studio.	40
4.27. Simulated $ S_{21} $ (dB) traces for an ideal and non-ideal cases of interferometric system.	41
4.28. Simulated $ S_{11} $ (dB) traces for an ideal and non-ideal cases of interferometric system	42
4.29. Detail of simulated $ S_{11} $ (dB) traces for an ideal and non-ideal cases of interferometric system.	43
4.30. Simulated $ S_{21} $ (dB) traces for an ideal case and case where only cross-talks m_{12} , m_{21} are omitted.	43
5.31. Uncertainty areas in S_{21} measurement.	46
5.32. Experimental verification using VNA and WR90 interferometer.	47
5.33. Experimental verification — measurement setup.	47
5.34. Experimental verification — setup in detail	48
5.35. Complete S-matrix data for the first data set	49
5.36. The measured $ S_{21} $ with markers on the minima	52
5.37. Measured $ S_{21} $ and fitted trace obtained from the calibration and corresponding least square error.	55
5.38. Measured $ S_{21} $ and fitted trace obtained from the calibration and corresponding least square error.	56

5.39. Measured $ S_{21} $ and fitted trace obtained from the calibration and corresponding least square error.	57
5.40. Error terms of the interferometer. Values obtained from the direct measurement on the VNA versus values returned from calibration technique	58
5.41. Resulting phase diagrams for the WR90 offset short 100 mm and 101 mm	59
A.42. Flow graph for the full 16-term model of the interferometer	67
A.43. Parameters m_{41} and m_{31} , magnitude and phase	69
A.44. Parameters m_{42} and m_{32} , magnitude and phase	70
A.45. Cross-talk m_{12} and m_{21} , magnitude and phase	70
A.46. Cross-talk m_{34} and m_{43} , magnitude and phase	71
A.47. Reflections m_{11} , m_{22} , m_{33} , m_{44} , magnitude and phase	71
A.48. Setup 1. Four measured S-parameters.	72
A.49. Setup 2. Four measured S-parameters.	73
A.50. Setup 3. Four measured S-parameters.	74
A.51. Setup 4. Four measured S-parameters.	75
A.52. Setup 5. Four measured S-parameters.	76
A.53. Setup 6. Four measured S-parameters.	77
A.54. Setup 7. Four measured S-parameters.	78
A.55. Measured S_{21} and fitted trace obtained from the calibration and corresponding least square error.	79
A.56. Measured S_{21} and fitted trace obtained from the calibration and corresponding least square error.	80
A.57. Measured S_{21} and fitted trace obtained from the calibration and corresponding least square error.	81

List of Tables

3.1. Selected uncertainties for reflection measurement on R&S ZVA-67 VNA. Specifications are based on an isolating DUT, a measurement bandwidth of 10 Hz, and a nominal source power of -10 dBm. [33].	12
3.2. Selected values for transmission measurement on R&S ZVA-67 VNA. Specifications are based on a matched DUT, a measurement bandwidth of 10 Hz, and a nominal source power of -10 dBm [33].	12
4.1. Theoretical and simulated values with the finite frequency step size - S_{21} . . .	29
4.2. Theoretical and simulated values with the finite frequency step size - S_{11} . . .	30
4.3. Theoretical and simulated values with the finite frequency step size - S_{11} . . .	35
4.4. Theoretical and simulated values with the finite frequency step size - S_{21} . . .	35
4.5. Comparison of cancellation frequencies of S_{21} simulations.	41
5.6. Measured set-ups.	49
5.7. WR90 segments used for the experimental verification	50
5.8. Evaluated values from the measurement	51
5.9. The results given using the proposed calibration technique 20000 points. . . .	54
5.10. The results given using the proposed calibration technique 500 points	55

1. Introduction

The measurement on the radio frequency and millimeter-waves involves numerous tasks, techniques, principles and equipment. This thesis deals with the interferometry measurement using Vector Network Analyzer. Not so long ago, Vector Network Analyzers were exclusively used in research and development departments for the measurement of RF and microwave components, antennas, etc. Since 1968, when the first VNA was launched, this device has undergone great development. This applies both to the hardware which the device consists of and the calibration techniques which are currently necessary for any VNA measurement as well. While the first VNA was able to measure up to 12 GHz and it was able to compensate for only very few systematic errors, the modern VNA can measure up to 500GHz [1] using converters and it offers more than ten various calibration techniques in the control software. Thanks to this, the VNA is very versatile and precise device which can be used for various tasks, even those that are not directly related to the measurement of microwave components, amplifiers and antennas; including for example permittivity measurement of various liquids or biological samples [2],[3], gas spectroscopy [4], nanotechnology [5, 6], near field sensing [7, 8, 9], etc.

However these mentioned applications are pushing the modern VNA to the edge or even behind the edge of its capabilities, so for some specific applications it is impossible to use the VNA as it is, because the uncertainty of the measurement is for some reason greater than can be accepted. Currently it seems that interferometric approach which will be explained in this work can overcome the problems and decrease uncertainty of measurement. Recent works in this field independently prove that it.

Although the interference is usually perceived as an unwanted phenomenon, in many of measurement tasks is this phenomenon utilized, especially in optics. Even in the RF and microwaves the interferometric approach is very well known. At the beginning, before the VNAs were available, RF engineers used to use so called *measuring bridges* for the impedance measurement. Despite the sensitivity and miscellaneous advantages of this interferometry approach, the measurement using such bridges was very tedious and prone to operator's error thus this approach was replaced by the VNA. Now it appears that for some of the state-of-the-art applications it is necessary to combine the advantages of the VNA and interferometric approach advantages.

The aim of this work is to describe original contribution in the field of interferometric measurements in millimeter-wave frequencies. Usually these measurements are performed using VNA with an external components, which act as an interferometer. This topic became interesting in the recent years, when the VNA started to be utilized by above mentioned challenging applications focused on measurement of electrical or even non-electrical quantities in the range of millimeter waves. Although, as indicated, interferometric measurements are commonly used in various fields, the measurement in the RF and microwave range has its specific aspects. Even though it may seem that the interferometric measurement is a well-known task; in the combination with the VNA and microwave components generally, there may arise a number of obstacles which have to be analyzed and solved. This work focuses

on the precise measurement of the phase of the reflection coefficient with an interferometer. Such a measurement is directly utilized in applications briefly described in the chapter 2, then chapter 3 depicts the limits of current VNA and need for the interferometry. Afterwards, chapter 4 illustrates basic principles of microwave interferometry in the theory and in the examples and various issues and obstacles are discussed. Finally, the fifth chapter presents the proposed calibration technique which is designed to overcome specific issues of the microwave interferometer.

2. Current state-of-the-art

This chapter briefly lists the selected state-of-the-art applications and approaches where interferometry is used for the measurement purposes in the RF and millimeter-wave band. The common aspect of all this following applications is that they utilize a VNA with a supplementary hardware component which acts as an interferometer. Based on the several recent works referred in [10], it can be seen that this kind of approach is mainly used for high and low impedance measurement where VNA itself has a worse accuracy [11, 12, 10, 13, 14], near field sensing [8, 15, 16], and also for applications where sensitive measurement of phase is required [17, 18, 19]. The sensitive and precise measurement of phase is usually required in the applications which are focused on the measurement of a non-electrical quantity such as distance or length, but in some isolated cases, the interferometry principle is used directly for the sensitive phase measurement as described in [20].

All works show great sensitivity and advantages of an interferometric measurements, but these works do not address, or only partially solve the problem of the systematic errors caused by the non-ideality of used hardware. So the common aspect for all these works is the lack of calibration techniques.

2.1. Measurement of high and low impedances

Classical measurement of impedances by measuring the reflection coefficient of the impedance provides poor resolution for impedances that are substantially smaller or substantially greater than the reference impedance of the VNA, that is usually $50\ \Omega$ [11, 12]. Limited stability of VNA itself (drifts) together with limited reproducibility of connection of a device under test (DUT) and calibration standards are the most limiting factors in extreme impedances measurements [11, 21].

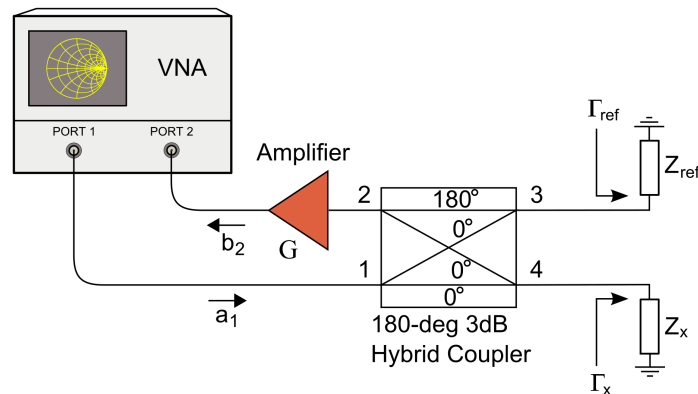


Figure 2.1. Arrangement of the measurement system – ideal components [11].

This technique uses 180° hybrid coupler as an interferometer in the following way. The

method is based on subtracting the reference reflection coefficient Γ_{ref} from the reflection coefficient of the DUT, Γ_x , amplifying this difference by an amplifier with gain G and measuring the resulting signal by a standard VNA as a transmission coefficient S_{21} . In the case of ideal components of the measurement system the measured transmission coefficient S_{21} is given by the equation

$$S_{21} = \frac{G}{2} (\Gamma_x - \Gamma_{ref}) \quad (2.1)$$

From this equation the value of the reflection coefficient Γ_x of the DUT is

$$\Gamma_x = \frac{2S_{21}}{G} + \Gamma_{ref} \quad (2.2)$$

The value of the transmission coefficient S_{21} is measured with the uncertainty ΔS_{21} which will cause that the true value of the reflection coefficient Γ_x of the DUT is changed by $\Delta\Gamma_x$.

$$\Gamma_x + \Delta\Gamma_x = \frac{2(S_{21} + \Delta S_{21})}{G} + \Gamma_{ref} \quad (2.3)$$

By subtracting equations 2.2 and 2.3 we obtain the value of uncertainty of the measured reflection coefficient.

$$\Delta\Gamma_x = \frac{2\Delta S_{21}}{G} \quad (2.4)$$

It is obvious that by using an amplifier with high gain G the uncertainty of the VNA can be significantly reduced. Maximum value of gain that can be used is limited by the difference of the reference reflection coefficient Γ_{ref} and the reflection coefficient Γ_x of the DUT and by hardware requirements and constraints of the VNA used.

Nevertheless, it is evident that ΔS_{21} includes only uncertainties caused by the random errors in the VNA. Moreover, it assumes an ideal behavior of the used elements so it is evident that for a real measurement systematic errors will play a role. This is also mentioned in the thesis [21], which is completely focused to this topic. The author of that thesis recommends development of calibration techniques and standards for such a system, because currently used standards are not sufficient to deal with this. There are several very recent works in this field dealing with the design of a new calibration standards and the calibration technique for such kind of system [22, 23]. It is evident that dealing with the systematic errors of the interferometer and its calibration is very actual problem.

2.2. Near field sensing – scanning microwave microscopy

Microwave sensing techniques are attractive for several different fields of research including biology, nanotechnology or non-destructive testing.

Despite the excellent performance of current existing microwave methods, most applications require measurement techniques that combine both high spatial resolution and measurement sensitivity. Thus one of the leaders in microwave measurement development – Agilent Technologies¹ introduced the unique device which combines the comprehensive electrical measurement capabilities of a VNA with the outstanding spatial resolution of an atomic force microscope (AFM). SMM Mode outperforms traditional AFM-based scanning capacitance microscopy techniques, offering far greater application versatility, the ability to acquire quantitative results, and the highest sensitivity and dynamic range in the industry. In SMM Mode, the performance network analyzer sends an incident microwave signal through a diplexer to the sub-7 nm conductive tip of a platinum-iridium cantilever. The signal is reflected from the tip and measured by the VNA. The magnitude and phase of the ratio between the incident and reflected signals are calculated and a model is then applied in order to calculate the electrical properties of the sample. The AFM scans the sample and moves the tip to specific locations to perform point probing. Operation frequencies up to 20GHz are supported. [24]

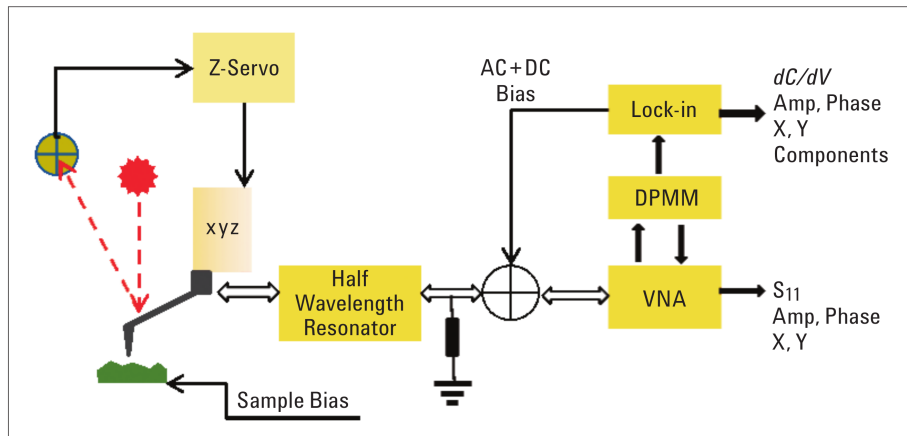


Figure 2.2. The principle of Agilent's SMM [24].

However, even here the problem of the measurement of high and low impedances is encountered, because the impedance of the measurement tip is far away from 50Ω , it is rather an open end. Firstly this was resolved in a way that the tip was connected in parallel to a load to match the 50Ω as shown in Fig 2.2. But it is obvious that this approach decrease measurement dynamics. So the efforts to improve the sensitivity of the measurement led to the different interferometry techniques and the near field microwave sensing is still the subject of the research.

Reference [7] utilizes a power divider as an interferometer as shown in the Fig. 2.3 and other work uses hybrid coupler for the near-field microwave microscopy [8].

¹At the time when author worked on this thesis, the company named Keysight Technologies was spun off of Agilent Technologies, bringing with it the product lines focused on electronics and radio including the Vector Network Analyzer, leaving Agilent with the chemical and bio-analytical products. So it would be correct to say, that the leader in the microwave measurement is the Keysight Technologies.

The principle of the measurement described in these works is as follows. The impedance tuner is used for the balancing of the interferometer. So the tuner is adjusted during the measurement process to reach sharp minimum at desired frequency in the $|S_{21}|$ (or $|S_{11}|$ for the setup with Wilkinson 3dB divider). When the interference is reached, the reflection coefficient of the tuner is given as a measured reflection from the tip. Nevertheless, in each of the works of the authors assume ideal parameters of the interferometric system.

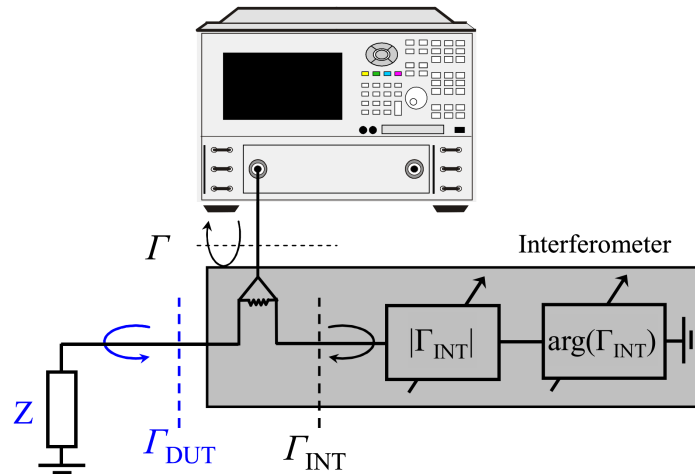


Figure 2.3. Interferometric setup using a 3 dB power divider [7].

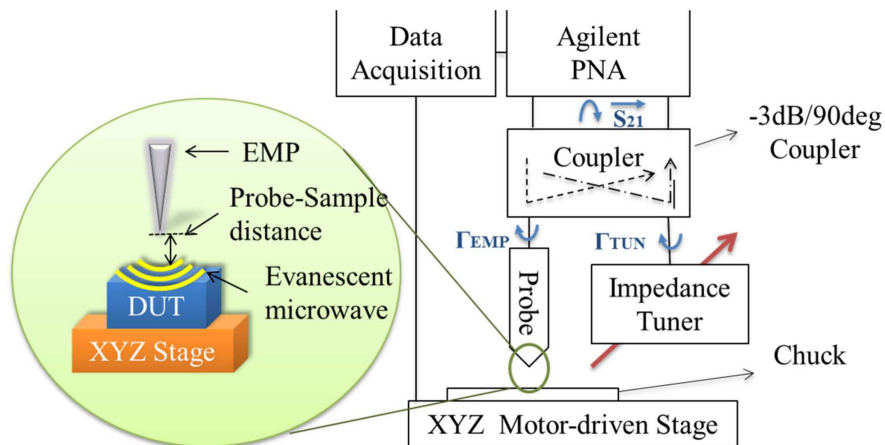


Figure 2.4. Interferometric setup using a hybrid coupler [8].

2.3. Distance measurement

The precision measurement of the distance or length is one of the fundamental and frequently used tasks, hence currently exist numerous techniques for such a measurement. These techniques differ by the measurement range, precision and accuracy, sensitivity, etc. For a variety of applications non-contacting measurement is required [25]. Laser sensors offer unparalleled accuracy, but they can be affected by the dirt on the sensor head or may not penetrate smoke, dust, and flying debris which might surround the target. This task could be well solved using the sensor utilizing millimeter waves instead of light.[26].

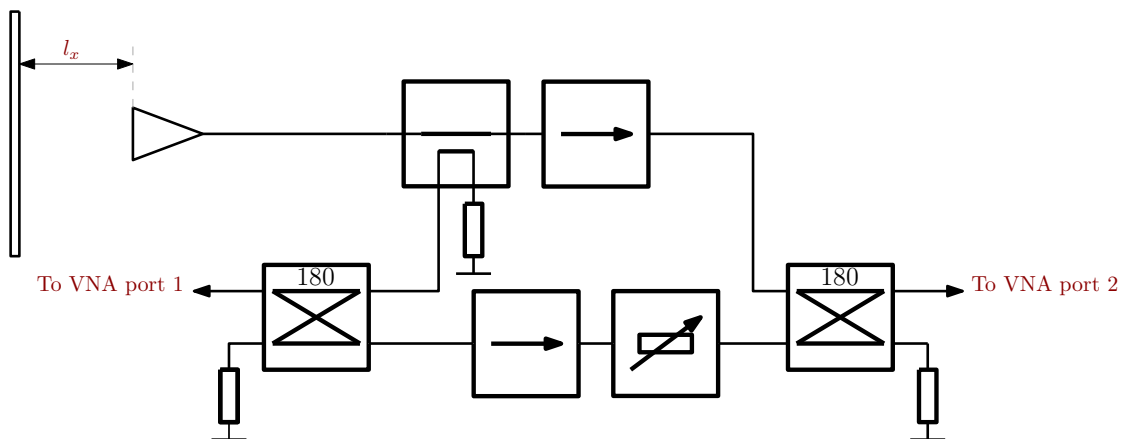


Figure 2.5. Microwave interferometric system for distance measurement according to [17].

Microwave non-contact distance measurement has been discussed in several recent articles [27, 26, 17, 25, 18, 19]. Every aforementioned work solved this issue in a different way and at different frequency range. Articles [17],[18],[19] use the interferometric methods for sensitive distance measurements. These works describe systems operating in the X-band whose sensitivity of distance measurement is in the range of micrometers.

Block diagram of one of this system is depicted in the Fig. 2.5 and the photograph of the same system is in the Fig. 2.8.

The principle of its function is as follows. Wave generated by the VNA (port 1) is divided by the 180° hybrid coupler into two paths. One of the paths consist of the isolator and the attenuator. This path is called the *reference channel*. The remaining path is the *test channel*. The wave passing through the test channel is headed towards the antenna and then reflected from the target. Wave reflected from the target returns back to the antenna and continues to the second hybrid coupler. In this coupler the wave from test channel is combined with the wave from the *reference channel*. When at specific frequency, both waves are exactly in the anti-phase, they destructively interfere with each other resulting in the zero energy at the output as depicted in Fig. 2.6. The output is connected to the second port of the VNA. Thanks to this, the direct measurement of S_{21} brings the information about interference over the frequency range.

While the wave passing through the *reference channel* has still the same delay, the delay of the *test channel* differs depending on the distance of the target in front of the sensor (antenna). Since the phase of these waves depends on the frequency, the mentioned destructive interference occurs only on the specific frequencies and any delay change in the *test channel*

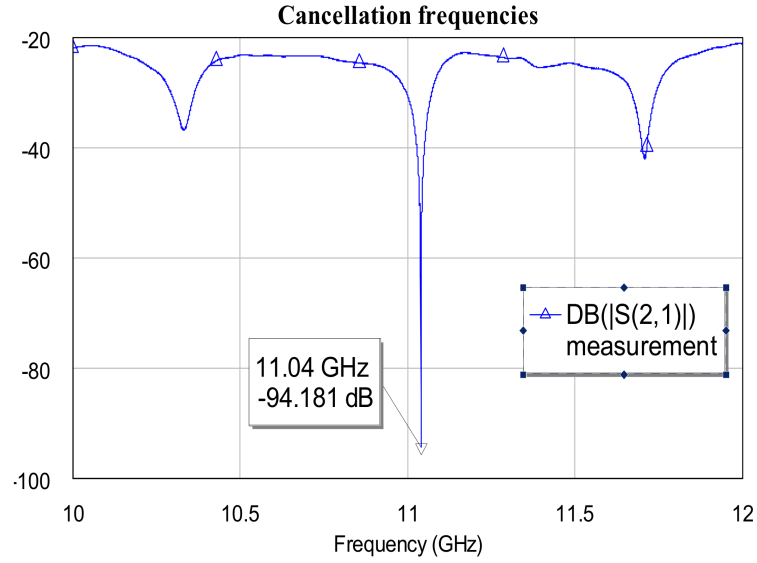


Figure 2.6. S_{21} measurement of the interferometric system. The frequency of the minimum depends on the measured distance [17].

(or *reference channel* as well) results in the frequency shift of the minimum energy to another frequency. Basically, the frequency at which the minimum occurs directly depends on the measured distance as shown in the Fig. 2.7.

In reference [17] there is described experimental verification of such a measurement approach. It was measured by the VNA Agilent PNA E8364A. The measurement system was assembled from the WR90 components as depicted in 2.8. As a sensor, a WR90 horn antenna was used. For the verification there was a reflective surface formed by a metal sheet in the distance of ≈ 20 mm from of the horn antenna. The sheet was mounted on the top of a micro-positioner, enabling to set up its distance with a resolution of one micrometer.

Although the results presented in this work prove the high sensitivity of such system, authors mention that the system works only in very narrow band. Outside this band, the parasitic properties of the system cause unexpected behavior and the cancellation frequencies are no longer linearly dependent to the distance. Moreover this work brings the approach only for the relative measurement – the absolute distance of the reflective sheet to the sensor was unknown and only small movement of the sheet was measured.

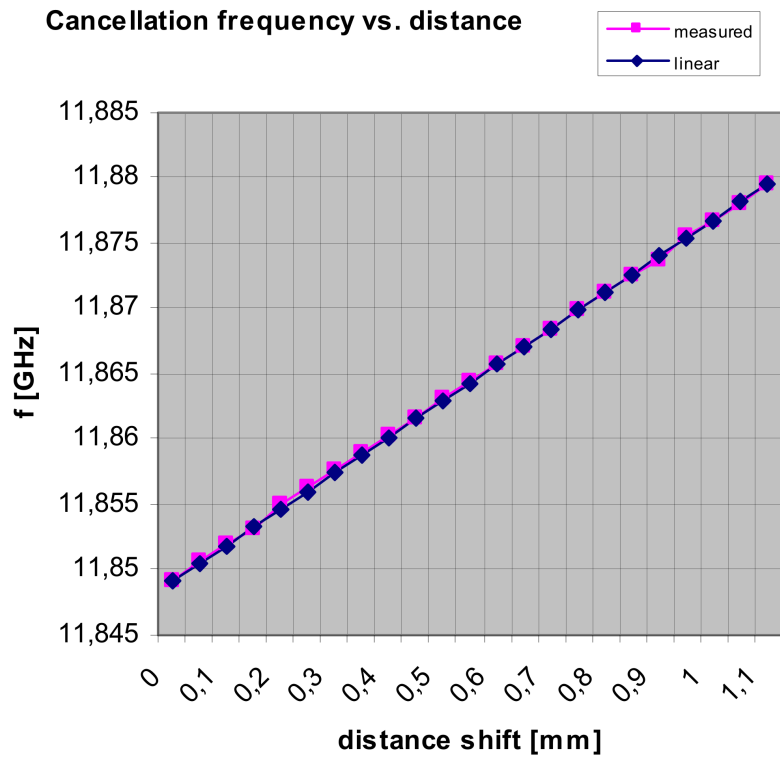


Figure 2.7. The dependence of the distance on the cancellation frequency. Measured vs expected trace [17].

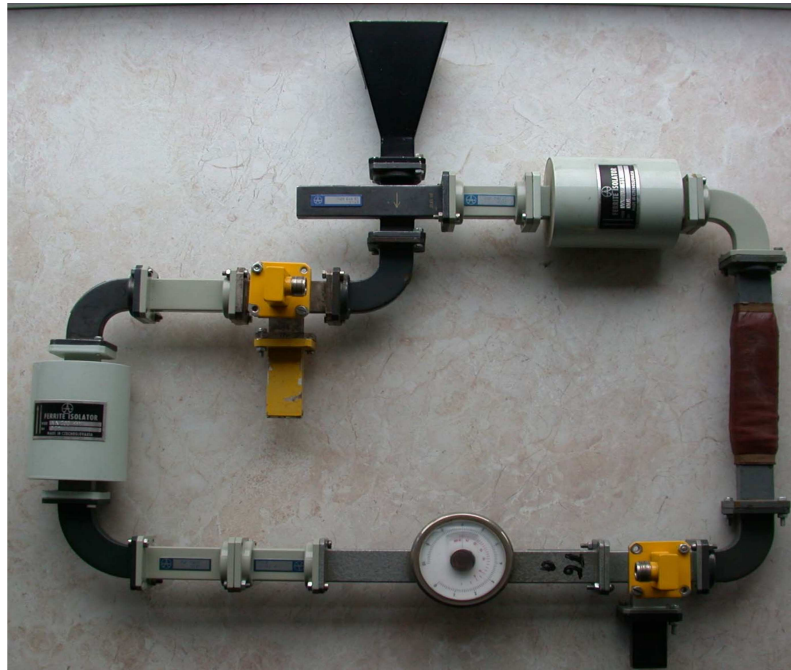


Figure 2.8. Microwave interferometric system for the distance measurement according to [17].

2.4. Thesis objectives

As it is evident from the current work in this area, microwave interferometry measurement is currently on the rise. There are several challenging applications which are only made feasible using an interferometric approach. Nevertheless, it is evident that many of above mentioned works are more like a proof of concept than the solution of the problem. Works using phase-shifting interferometry neglect completely all the effects of systematic errors caused by the non-ideal hardware and use the interferometer as an ideal device. Furthermore, the works using the interferometric approach for the phase/distance measurement utilize that technique only for the relative measurement of the phase/distance, so an approach for the absolute phase/distance measurement is missing. The aim of this work is to deal with the known problems of such measurement. Especially to develop suitable calibration technique.

Briefly, the objectives of this thesis are:

1. Full model description and analysis of microwave interferometric system
2. Analysis of the systematic errors
3. Approach for the absolute phase measurement
4. Design of calibration methods for microwave interferometer

3. Uncertainty analysis

Prior to any measurement it is necessary to discuss the uncertainty of measurement. The uncertainty of the measurement with and without an interferometric system is the key factor in decision whether the interferometry setup is suitable for such measurement.

In this chapter a case of measurement using VNA will be shown wherein even the very modern VNA is very close to the limit of applicability. Comparing the uncertainties of the measurement with and without the interferometric system will be shown, how an interferometric approach can help to push the limit of the VNA a little further.

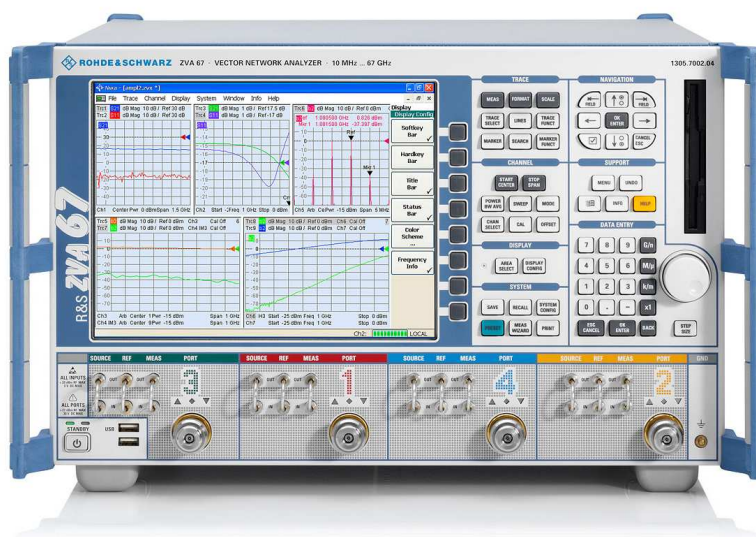


Figure 3.9. Rohde&Schwarz ZVA-67 Vector Network Analyzer.

3.1. Measurement of the phase of the reflection coefficient

Vector Network Analyzers are the nearly versatile devices which allow numerous measurements in the RF and microwave frequency range. Despite the complexity of the device, there are cases of measurement, where the measured data contain fairly high uncertainty. Prior to each measurement or experiment, it is necessary to address the question of measurement errors or uncertainties.

The uncertainty evaluation for a VNA measurement is the subject of research in the several laboratories [28, 29, 30, 31, 32]. Nevertheless the problem of VNA residual uncertainty is still lacking of a comprehensive and uniform theory [32]. Therefore it seems to be adequate to use the uncertainty values given by the vendor of VNA.

Let's look at the parameters of modern VNA. Rohde&Schwarz ZVA 3.9 high-end VNA with lot of features and also with state-of-the-art hardware [1]. In the datasheet of R&S ZVA

50 MHz to 67 GHz	for +10 dB to +3 dB	< 0.4 dB or < 4°
	for +3 dB to -15 dB	< 0.4 dB or < 3°
	for -15 dB to -25 dB	< 1 dB or < 6°
	for -25 dB to -35 dB	< 3 dB or < 20°

Tab. 3.1. Selected uncertainties for reflection measurement on R&S ZVA-67 VNA. Specifications are based on an isolating DUT, a measurement bandwidth of 10 Hz, and a nominal source power of -10 dBm. [33].

2 GHz to 24 GHz	for +15 dB to +5 dB	< 0.3 dB or < 3°
	for +5 dB to -55 dB	< 0.1 dB or < 1°
	for -55 dB to -70 dB	< 0.2 dB or < 2°
	for -70 dB to -85 dB	< 1 dB or < 6°
24 GHz to 32 GHz	for +15 dB to +5 dB	< 0.3 dB or < 3°
	for +5 dB to -45 dB	< 0.2 dB or < 2°
	for -45 dB to -60 dB	< 0.3 dB or < 3°
	for -60 dB to -75 dB	< 1 dB or < 6°
32 GHz to 40 GHz	for +15 dB to +5 dB	< 0.4 dB or < 4°
	for +5 dB to -40 dB	< 0.2 dB or < 2°
	for -40 dB to -55 dB	< 0.4 dB or < 4°
	for -60 dB to -70 dB	< 1 dB or < 6°
40 GHz to 50 GHz	for +15 dB to +5 dB	< 0.4 dB or < 4°
	for +5 dB to -35 dB	< 0.2 dB or < 2°
	for -35 dB to -50 dB	< 0.4 dB or < 4°
	for -50 dB to -65 dB	< 1 dB or < 6°
50 GHz to 67 GHz	for +15 dB to +5 dB	< 0.4 dB or < 4°
	for +5 dB to -30 dB	< 0.2 dB or < 2°
	for -30 dB to -45 dB	< 0.4 dB or < 4°
	for -45 dB to -60 dB	< 1 dB or < 6°

Tab. 3.2. Selected values for transmission measurement on R&S ZVA-67 VNA. Specifications are based on a matched DUT, a measurement bandwidth of 10 Hz, and a nominal source power of -10 dBm [33].

measurement accuracy section can be found. There is written in the datasheet:

This data is valid between +18 °C and +28 °C, provided the temperature has not varied by more than 1 K after calibration. Validity of the data is conditional on the use of a suitable calibration kit. This calibration kit is used to achieve the effective system data specified below. Frequency points, measurement bandwidth and sweep time have to be identical for measurement and calibration (no interpolation allowed) [33].

And in the tables 3.2 and 3.1 there are selected values from the datasheet concerning the measurement accuracy using this device. For the following examples the R&S ZVA67 datasheet values will be used, because the identical VNA was used for the experimental verification. However, the another manufacturer of the VNAs, the Keysight Technologies, presents very similar values in the datasheets for the Keysight Technologies VNAs [34, 35].

Now imagine the example of measurement scenario as shown in the Fig. 3.10. There are two almost identical homogeneous lines connected to the completely identical VNAs and the

VNAs are used for the measurement of the phase of the reflection coefficient.

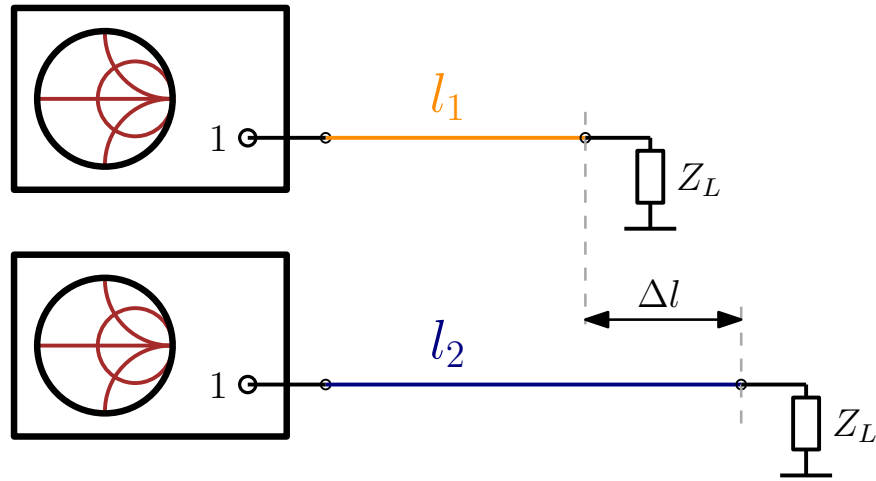


Figure 3.10. Measurement scenario. A two transmission lines with different length, connected to the VNA and terminated by an impedance Z_L which is close to short circuit.

The only difference between the homogeneous lines is the length of both lines. The difference in lengths of lines is about 1 mm. Repeatability effects are omitted. VNA is set according to the datasheet, so the power level is -10 dBm and the resolution bandwidth is 10 Hz. Then we can expect that the worst case of uncertainty corresponds to the values in the table 3.1. Assuming lossless line, terminated with the impedance causing reflection approx $\Gamma \approx 0.9$, we can expect incident power ≈ -11 dBm, so the worst case of uncertainty is 0.4 dB for the magnitude and 3° for the phase.

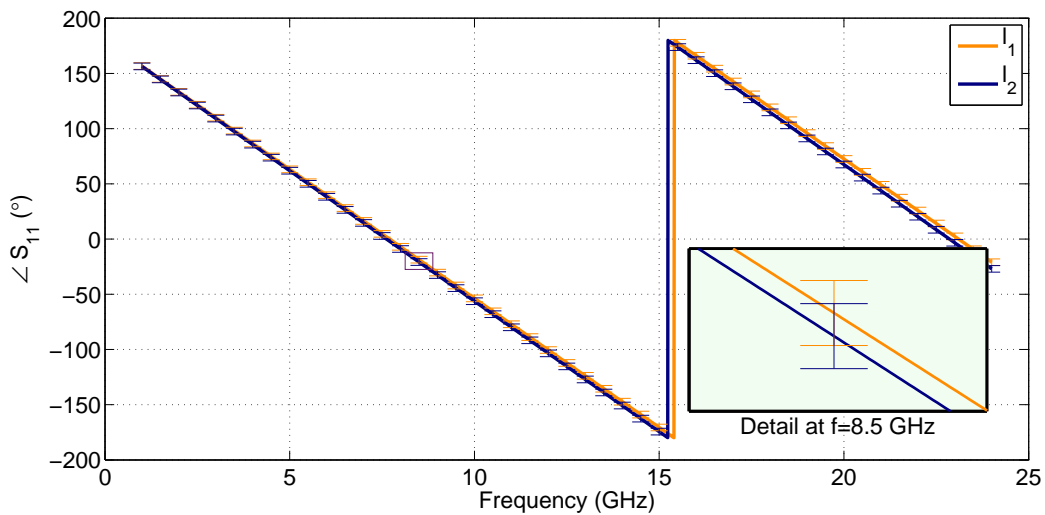


Figure 3.11. Phase of S_{11} parameter for both lines including uncertainty regions.

The result of such measurement is shown in the Fig. 3.11 including the 3° uncertainty regions. Magnified window in Fig. 3.11 shows clearly the overlapping areas of uncertainties. This example demonstrates the impossibility of measuring and recognition of small phase

differences directly using VNA. The same result is evident from the Smith chart 3.12. There are shown selected impedances at the frequencies 7.5, 8.5, and 9.5 GHz and there are also magnified windows with the detail of uncertainty region.

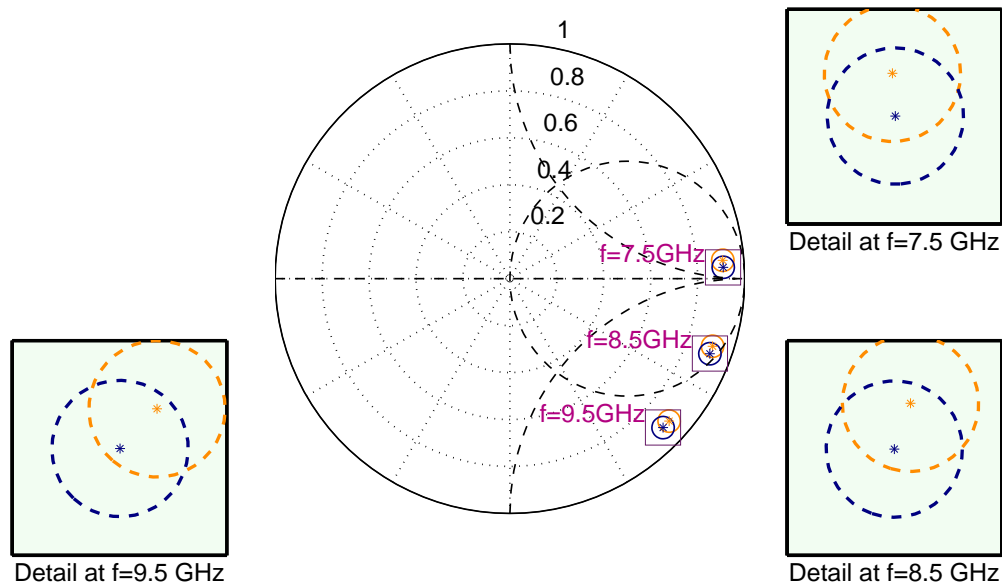


Figure 3.12. Smith chart with S_{11} parameter for both lines including uncertainty regions.

3.2. Uncertainty of an interferometric measurement

As previous example has shown, in the direct phase measurement of the two very similar DUTs with very small difference in the phase of reflection coefficient, the results can't be distinguished. That is because of overlapping uncertainty regions.

Therefore the main aim is to decrease the uncertainty of phase measurement. In this work interferometric principle will be used for this purpose. The key idea is to convert direct phase measurement to amplitude measurement. This idea is very simply shown in the Fig. 3.17. Fig. 3.17a. depicts phases of reflection coefficients measured by the VNA according to setup in the Fig. 3.10.

Now, let's suppose there is an ideal interferometric system connected to the VNA as shown in Fig. 3.13. This box act as an additional instrument for the VNA. The homogeneous lines are the same as were used in the previous example with direct VNA measurement.

For this moment, let's leave aside what exactly is inside this mentioned interferometer. This mentioned device can convert information about phase to magnitude as shown in the Fig. 3.17. The general principle of operation is as follows. Wave passing from the VNA is equally or unequally split in two parts in the interferometer. It means that there are two separate paths. Then the first wave continues towards DUT where it is reflected. Second wave propagates through *reference channel* inside the interferometer towards the output and then is somehow combined with the reflected wave from the DUT. Therefore the output from

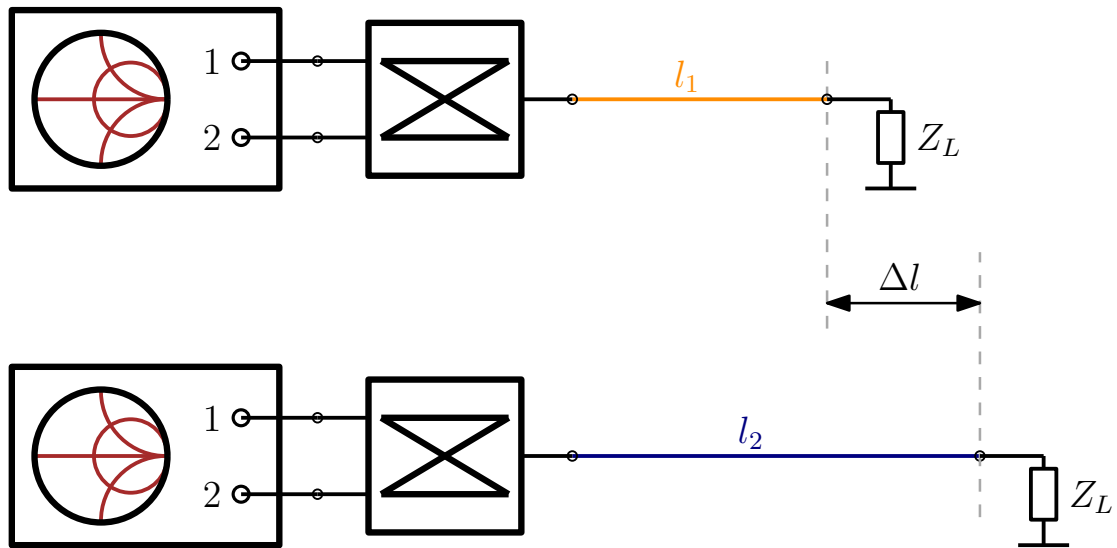


Figure 3.13. Measurement scenario with an ideal interferometric extender connected the VNA.

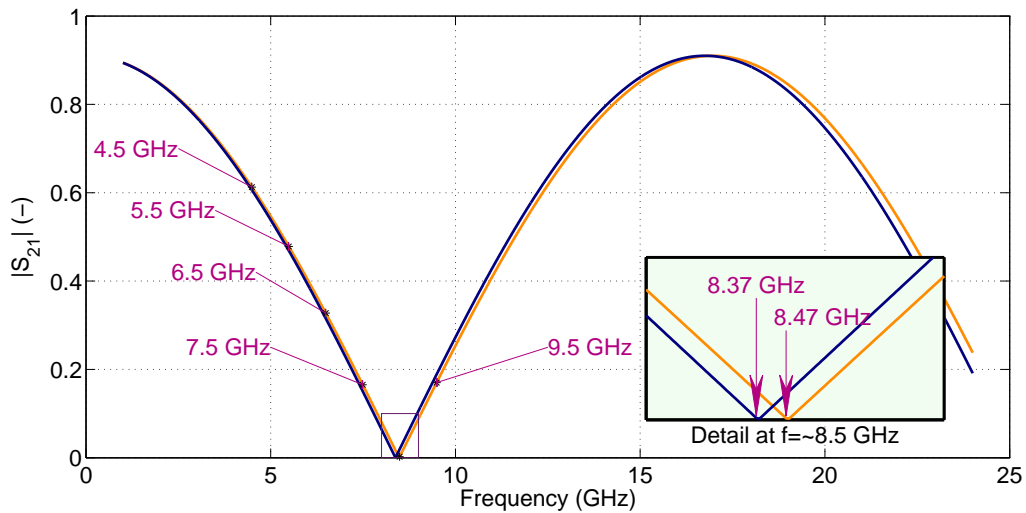


Figure 3.14. Expected values assuming ideal interferometer.

the interferometer contains resulting combination of both waves. If the waves are in the anti-phase, waves interfere in the destructive way resulting in zero energy at the output. Thanks to this, there are the mentioned sharp minima in the magnitude of S_{21} .

When the phase of the DUT is changed somehow (e.g. different length of a homogeneous line), it will produce minimum on the different frequency. This is the most important information. Small change in the phase will result in change of the sharp minimum of magnitude measurement. This behavior is shown in the Fig. 3.14. Traces of the S_{21} in this figure represent expected ideal measurement and there is clearly depicted how sensitively the minimum is shifted to different frequency with the very small change in the measured phase. Moreover, Fig. 3.15 and 3.16 displays the selected frequency points of the S_{21} measurement in the complex plane, again with the worst case of uncertainty. There is very illustratively shown

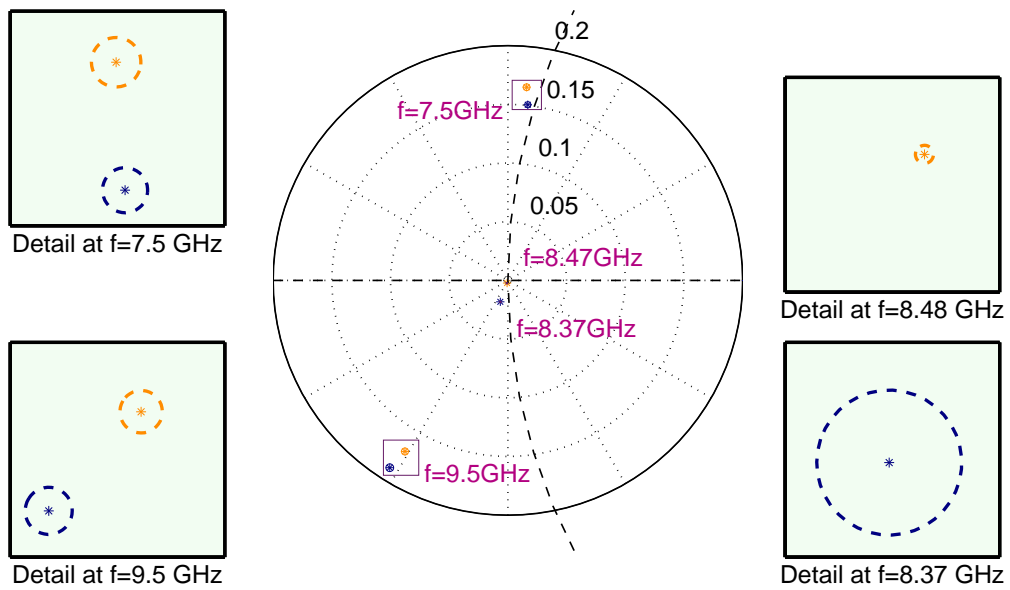


Figure 3.15. Smith chart with selected frequency points of the S_{21} parameter measured by the interferometric system including uncertainty regions.

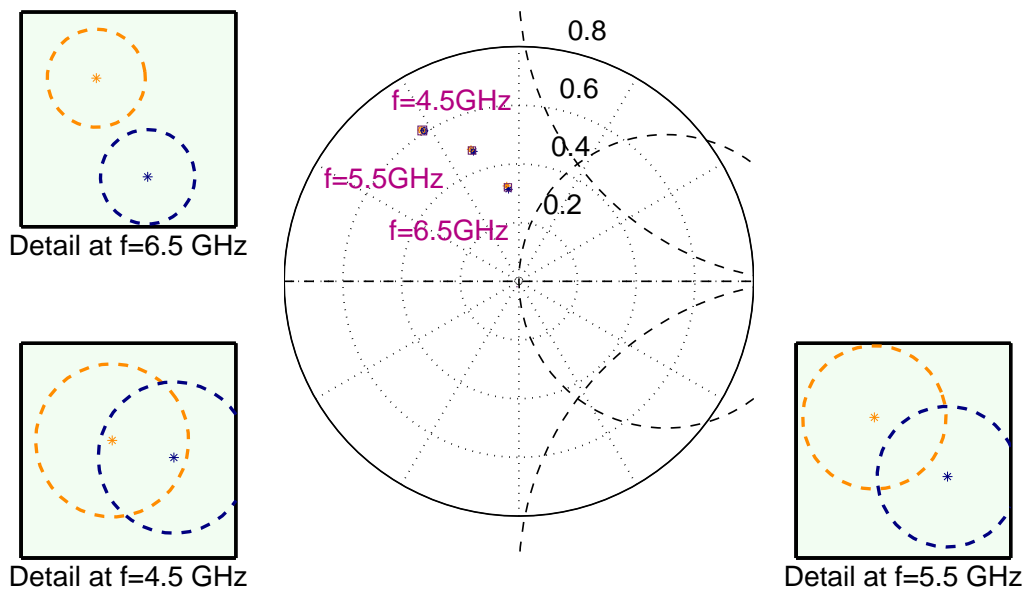
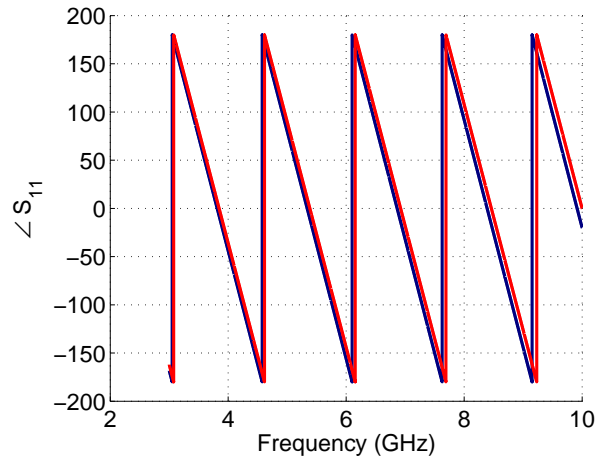


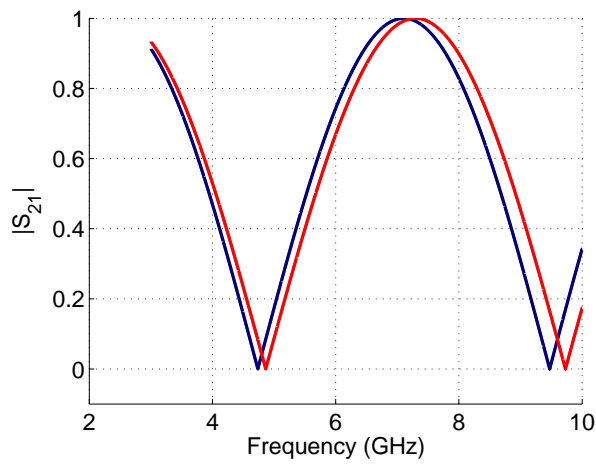
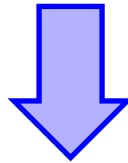
Figure 3.16. Smith chart with selected frequency points of the S_{21} parameter measured by the interferometric system including uncertainty regions.

how the interferometric measurement decrease the uncertainty of the measurement. Since the uncertainty regions are the smallest in the minima of the S_{21} , the measurement at the

frequency where the minimum occurs can be very suitable in term of the uncertainty. However the values close to the minimum have also non overlapping uncertainty regions and this knowledge will be used in the mentioned calibration technique.



a.) Phase diagram of two similar DUTs. Direct S_{11} measurement on a VNA



b.) Amplitude diagram of an interferometric setup using mentioned DUTs

Figure 3.17. Example of phase to magnitude measurement conversion using an interferometric setup. Each color represents measurement of the same DUT

4. Interferometric measurements

This chapter successively describes the principles and methods of the interferometric measurements. Since this work was motivated by precise phase measurement and the distance measurement, emphasis is placed on the measurement of the phase of reflection coefficient. That is because distance measurement is directly proportional to the phase measurement. Thus it was necessary to choose a proper general model for any DUT, which allows to convert distance to phase and vice versa. This conditions are met using the model of a homogeneous line terminated with an impedance as shown in the Fig. 4.1.

$$\Gamma_{DUT}(f) = e^{-2l_0(i\beta(f)+\alpha(f))} \frac{Z_L(f) - Z_0(f)}{Z_L(f) + Z_0(f)} \quad (4.1)$$

Where $\Gamma_{DUT}(f)$ is the reflection coefficient measured in the plane marked in the Fig 4.1. Then $\beta(f)$ is phase constant and $\alpha(f)$ is attenuation constant. Z_0 is the line impedance. Assuming that terminating impedance Z_L as well as line impedance Z_0 are frequency independent, it is obvious that the phase of $\Gamma_{DUT}(f)$ is proportional to the length of line l_0 .

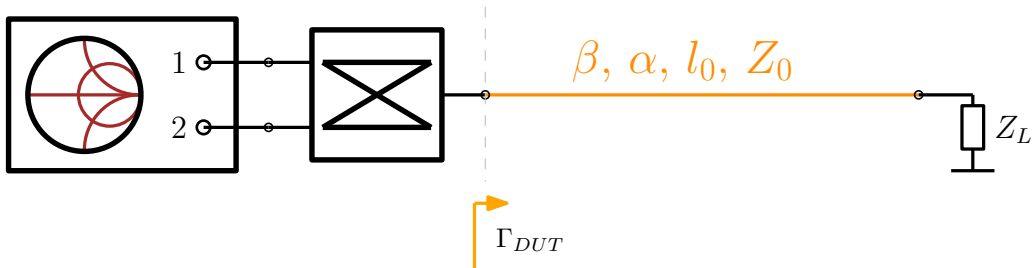


Figure 4.1. Interferometric setup with a homogeneous line as a DUT.

Due to mentioned reasons the model of a homogeneous transmission line will be used in the entire derivation. The detailed derivation will be done with a 180° hybrid coupler. That is because 180° hybrid coupler is the most often used component for the microwave interferometry. However, the principles of other devices such a 90° hybrid coupler or 3 dB power divider are very similar and will be very briefly presented as well. But this is certainly not the only component that could be used in a microwave interferometer. There are plenty of structures and devices with similar properties which could be utilized. And it is obvious that is impossible to show the behavior of all these structures as well as the derived equations. To avoid this, a general model was derived for the microwave interferometer. It can apply to the 180° hybrid coupler, 90° hybrid coupler or for combination of more components which together form an interferometer.

4.1. 180° Interferometer – ideal case

In this section, the previous general considerations will be presented and discussed on a system which utilizes 180° hybrid coupler as an interferometer. Ports of coupler are numbered in accordance with the matrix 4.2. It is apparent that, there are no reflections or crosstalk. Real case containing crosstalk and reflections will be discussed later. This idealized example serves to derive and explain the basic principles.

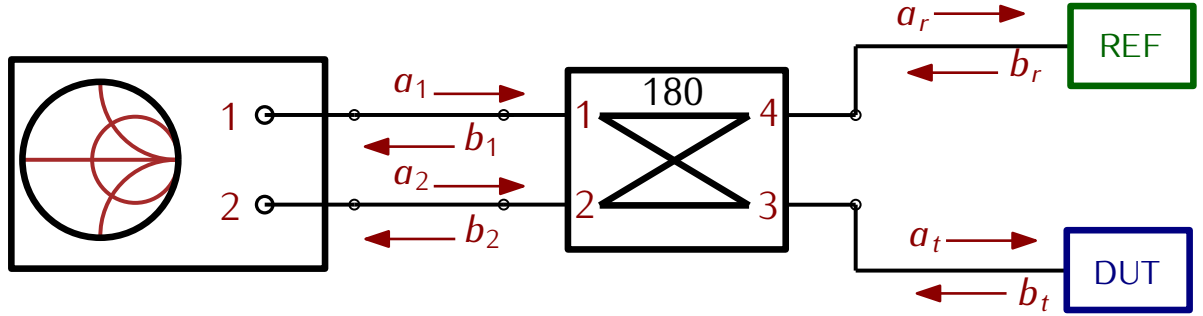


Figure 4.2. Interferometer approach using 180° hybrid coupler

An ideal VNA is used as a measurement device in this case. Ideal VNA means there is no systematic or random error during the measurement.

$$S_{h180} = \begin{pmatrix} 0 & 0 & \frac{1}{\sqrt{2}} & -\frac{1}{\sqrt{2}} \\ 0 & 0 & \frac{1}{\sqrt{2}} & \frac{1}{\sqrt{2}} \\ \frac{1}{\sqrt{2}} & \frac{1}{\sqrt{2}} & 0 & 0 \\ -\frac{1}{\sqrt{2}} & \frac{1}{\sqrt{2}} & 0 & 0 \end{pmatrix} \quad (4.2)$$

From the block diagram it is evident, there is chance to measure four S-parameters directly using VNA:

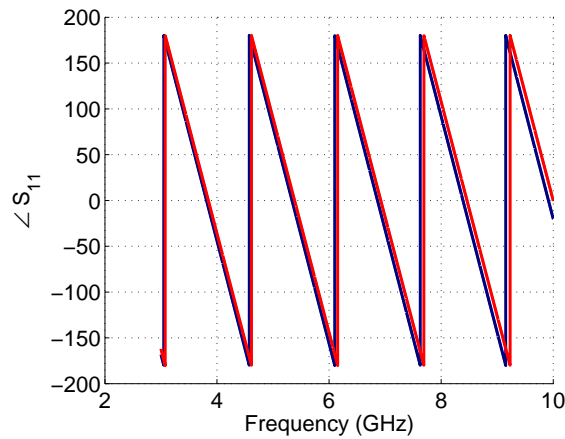
$$S_{11} = \frac{b_1}{a_1} = \frac{1}{a_1} \left(b_t \frac{1}{\sqrt{2}} - b_r \frac{1}{\sqrt{2}} \right) = \left(\frac{1}{\sqrt{2}} \frac{1}{\sqrt{2}} \Gamma_D + \frac{1}{\sqrt{2}} \frac{1}{\sqrt{2}} \Gamma_R \right) = \frac{1}{2} \Gamma_D + \frac{1}{2} \Gamma_R \quad (4.3)$$

$$S_{21} = \frac{b_2}{a_1} = \frac{1}{a_1} \left(b_t \frac{1}{\sqrt{2}} + b_r \frac{1}{\sqrt{2}} \right) = \left(\frac{1}{\sqrt{2}} \frac{1}{\sqrt{2}} \Gamma_D - \frac{1}{\sqrt{2}} \frac{1}{\sqrt{2}} \Gamma_R \right) = \frac{1}{2} \Gamma_D - \frac{1}{2} \Gamma_R \quad (4.4)$$

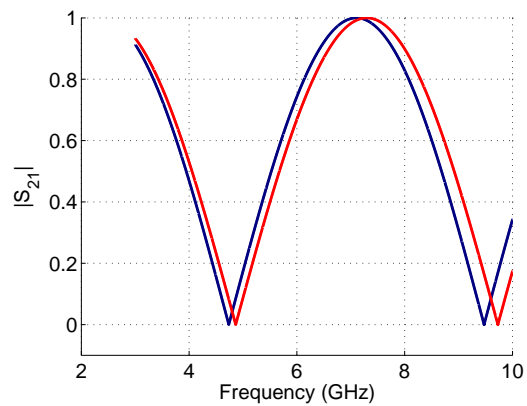
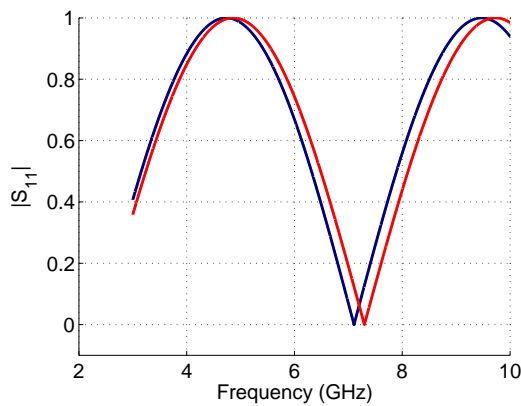
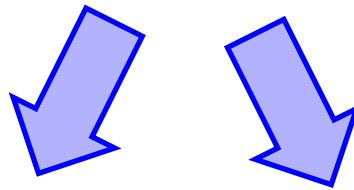
$$S_{12} = \frac{b_1}{a_2} = \frac{1}{a_2} \left(b_t \frac{1}{\sqrt{2}} - b_r \frac{1}{\sqrt{2}} \right) = \left(\frac{1}{\sqrt{2}} \frac{1}{\sqrt{2}} \Gamma_D - \frac{1}{\sqrt{2}} \frac{1}{\sqrt{2}} \Gamma_R \right) = \frac{1}{2} \Gamma_D - \frac{1}{2} \Gamma_R \quad (4.5)$$

$$S_{22} = \frac{b_2}{a_2} = \frac{1}{a_2} \left(b_t \frac{1}{\sqrt{2}} + b_r \frac{1}{\sqrt{2}} \right) = \left(\frac{1}{\sqrt{2}} \frac{1}{\sqrt{2}} \Gamma_D + \frac{1}{\sqrt{2}} \frac{1}{\sqrt{2}} \Gamma_R \right) = \frac{1}{2} \Gamma_D + \frac{1}{2} \Gamma_R \quad (4.6)$$

It follows that, in such a measuring arrangement it is possible to obtain several equivalent results during one measurement. It may be beneficial for some data processing techniques that can benefit from overdetermined set of data. On the other hand, it also points to the possibility of simplifying measurement hardware - for example, to measure only S_{11} using one-port VNA. Nevertheless, the choice of the measured parameter (S_{21} or S_{11}) also brings the need to deal with the uncertainty of measurement of these parameters using VNA itself. In the Fig. 4.3a. there are measured phases of the reflection coefficient according to the setup described in the 3.10. In the remaining figures 4.3b. and 4.3c. the measured $|S_{11}|$ and $|S_{21}|$ traces are depicted.



a.) Phase diagram of two similar DUTs. Direct S_{11} measurement on a VNA



b.) $|S_{11}|$ measured using an interferometric setup. c.) $|S_{21}|$ measured using an interferometric setup.

Figure 4.3. An example of phase-to-magnitude measurement conversion using an interferometric setup. Each color represents measurement of the same DUT

4.1.1. Phase measurement using interferometer

The setup shown in the Fig. 4.4 will be used to derive relationships and principles for the measurement using interferometer. The major part is an ideal 180° hybrid coupler.

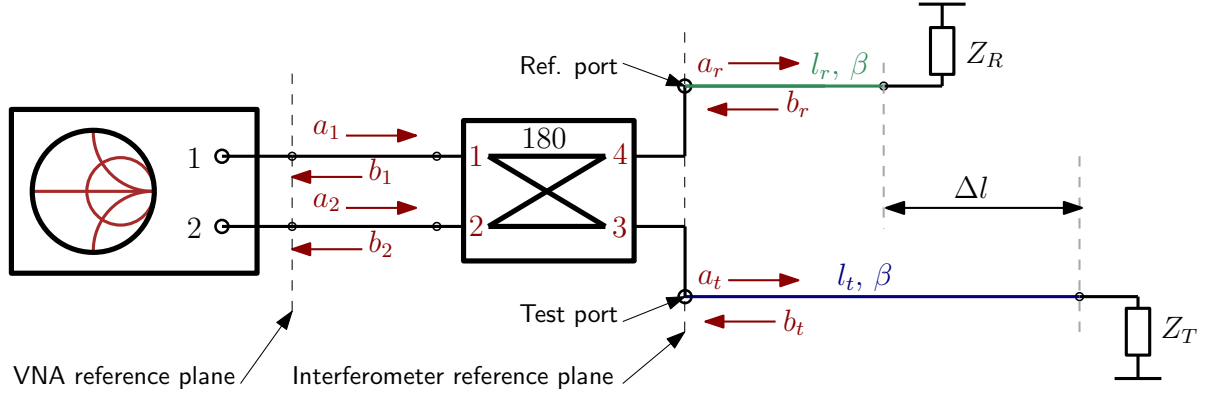


Figure 4.4. Interferometer approach using 180° hybrid coupler

Furthermore, the setup contains the *test channel* and *reference channel* and there are two terminated homogeneous lines connected to *test* and *reference port* respectively.

The both impedances connected to the reference plane of the interferometer consist of homogeneous line and a terminating impedance. The reflection coefficient of reference impedance is adjusted prior the measurement in such way to achieve desired behavior of the system. It means to achieve proper interference which is required. In this case the homogeneous lines are lossless, $\beta(f)$ is phase constant and l_r and l_t are lengths of reference and test channel respectively. Thus the phase of the reflection coefficient of such homogeneous line is proportional to the length. The $\beta(f)$ depends on the used environment where the wave propagates. The $\beta(f)$ is different for the line with mode TEM, TE₁₀, etc. Thanks to this assumption it is possible to easily convert the length to phase coefficient and vice versa.

The following derivation serves to exact demonstration of the origin of the interference in such system. This derivation serves to comprehension of the principle of the phase measurement using microwave interferometer.

Both terminating impedances in the reference plane of the interferometer can be written as:

$$\Gamma_R(f) = \frac{Z_R(f) - Z_0(f)}{Z_R(f) + Z_0(f)} e^{-2i\beta(f)l_r} \quad (4.7)$$

$$\Gamma_T(f) = \frac{Z_T(f) - Z_0(f)}{Z_T(f) + Z_0(f)} e^{-2i\beta(f)l_t} \quad (4.8)$$

Putting 4.7 and 4.8 to 4.3 and 4.4 the equations for the transmission and reflection measurement are obtained:

$$S_{11}(f) = \frac{1}{2} \left(\frac{Z_T(f) - Z_0(f)}{Z_T(f) + Z_0(f)} e^{-2i\beta(f)l_t} + \frac{Z_R(f) - Z_0(f)}{Z_R(f) + Z_0(f)} e^{-2i\beta(f)l_r} \right) \quad (4.9)$$

$$S_{21}(f) = \frac{1}{2} \left(\frac{Z_T(f) - Z_0(f)}{Z_T(f) + Z_0(f)} e^{-2i\beta(f)l_t} - \frac{Z_R(f) - Z_0(f)}{Z_R(f) + Z_0(f)} e^{-2i\beta(f)l_r} \right) \quad (4.10)$$

In the case when $Z_R = Z_T$, the equations 4.9 and 4.10 can be simplified in following way:

$$S_{11}(f) = \frac{1}{2} \frac{Z_T(f) - Z_0(f)}{Z_T(f) + Z_0(f)} \left(e^{-2i\beta(f)l_t} + e^{-2i\beta(f)l_r} \right) \quad (4.11)$$

$$S_{21}(f) = \frac{1}{2} \frac{Z_T(f) - Z_0(f)}{Z_T(f) + Z_0(f)} \left(e^{-2i\beta(f)l_t} - e^{-2i\beta(f)l_r} \right) \quad (4.12)$$

This case, when $Z_R = Z_T$ cannot be always achieved in practice, but is very handy to be close to this condition during practice measurements. This aspect will be briefly discussed in the section 4.1.2.

Since this technique is based on the measurement of the position of minima at the frequency axis (as proposed in the [17]), the desired result could be derived putting:

$$S_{11}(f) = 0 \quad (4.13)$$

and

$$S_{21}(f) = 0 \quad (4.14)$$

At the first glance, the each equation can be satisfied by two ways. First way is following equation

$$0 = \frac{Z_T(f) - Z_0(f)}{Z_T(f) + Z_0(f)} \quad (4.15)$$

Perfect match in the test or reference channel

The equation 4.15 is satisfied for $Z_T = Z_0$ ($Z_T = Z_R = Z_0$) which is the case when both impedances are perfectly matched to interferometer. It simply means that no wave is reflected in *reference* as well as *test channel*. Thus no waves can interfere each other.

More generally, from equations 4.9 and 4.10 is evident, that matching of any single channel leads to cancellation of any interference at all. That is because there is need to have two waves for the interferometry principle. This is unwanted scenario, because this setup does not produce any sharp minima.

Condition for interference

There is a second way how to satisfy the equations 4.13 and 4.14. The equations 4.16 and 4.17 are the terms describing origin of minima in the amplitude measurement of S_{11} and S_{21} respectively. The derivation and results of these equations will illustrate the basic principle of operation of this technique

$$0 = \left(e^{-2i\beta(f)l_t} + e^{-2i\beta(f)l_r} \right) \quad (4.16)$$

$$0 = \left(e^{-2i\beta(f)l_t} - e^{-2i\beta(f)l_r} \right) \quad (4.17)$$

The equation 4.17 is expressed in Fig 4.5. This diagram illustrates two rotating vectors that are present in the equation 4.17 and also illustrates the case when the vectors are exactly

in the antiphase. The diagram 4.5 is in the accordance with the setup in the Fig. 4.6a. The green vector represents the *reference channel* and the blue vector represents the *test channel*.

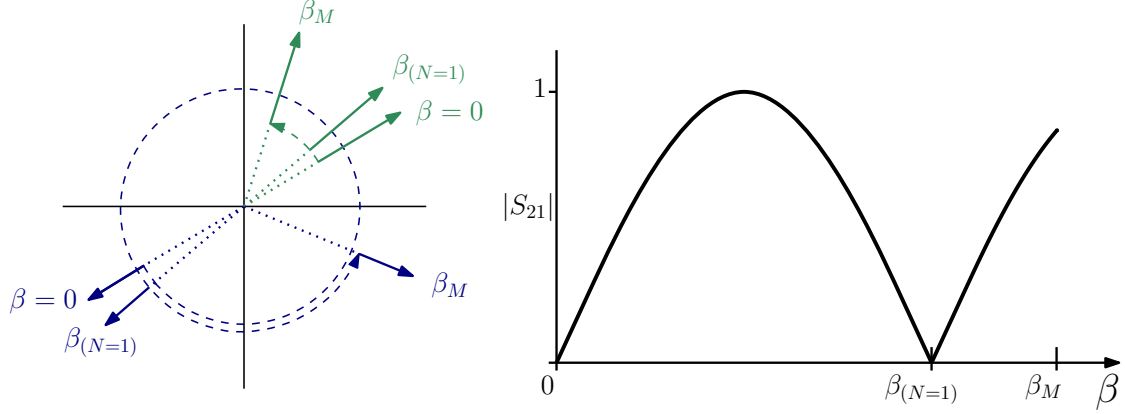


Figure 4.5. Vectors of waves from the *test* (blue) and *reference* (green) channels in the left figure, measured $|S_{21}|$ trace in the right.

Simplifying the (4.17) leads to equation:

$$\log \left(e^{-2i\beta(f)l_r} \right) = \log \left(e^{-2i\beta(f)l_t} \right) \quad (4.18)$$

$$i(-2\beta(f)l_r + 2\pi N_r) = i(-2\beta(f)l_t + 2\pi N_t) \quad (4.19)$$

$$(4.20)$$

And then desired result can be easily derived.

$$\Delta l = (l_t - l_r) = \frac{\pi(N_t - N_r)}{\beta(f_N)} \quad (4.21)$$

The equation 4.21 illustrates the relationship between phase constant $\beta(f)$ at frequency f where minimum was measured and length difference Δl between homogeneous line in the *test* and *reference channels*. N_t and N_r represents extension of *test* and *reference channels* in number of wavelengths. It can be simplified to $N = N_t - N_r$ and then N represents the order of the minima in the $|S_{21}|$ interferogram.

$$\Delta l = (l_t - l_r) = \frac{\pi N}{\beta(f_N)} \quad (4.22)$$

Furthermore Fig. 4.5 depicts lengths of the homogeneous lines used in the *reference* and *test channels*. Both vectors rotate at the same time from zero frequency where $\beta(0) = \beta_0$ to the frequency where $\beta(m) = \beta_m$, but blue vector (*test channel*) rotates faster than green vector. It means, that physical length of *test channel* is greater than the physical length in the *reference channel*. Thanks to this is possible to observe destructive interference on the frequency where $\beta(f) = \beta_{(N=1)}$.

Then Fig. 4.7 depicts a situation in which the physical length of the *test channel* is greater

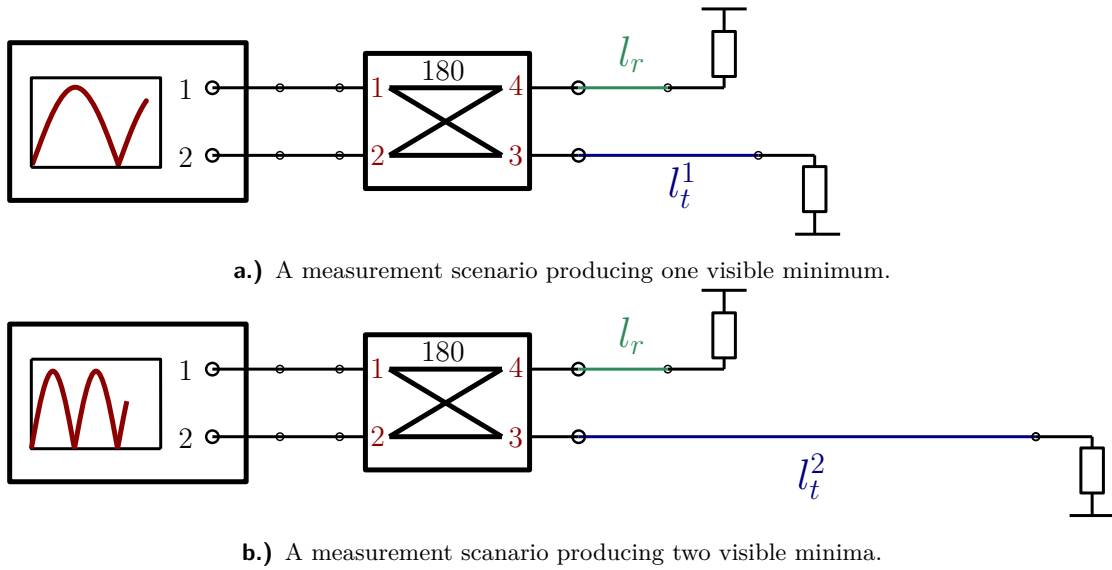


Figure 4.6. Two DUTs different in the phase measured using interferometer setup with 180° hybrid coupler

then it was in the previous scenario depicted on the Fig. 4.5. The *reference channel* is still the same. The result is that vector representing *test channel* rotates faster than it rotates in the previous case in the Fig. 4.5, thus the first minimum in the S_{21} interferogram occurs on the lower frequency. In addition, vectors of *test* and *reference channels* are in the antiphase multiple times and there are more than one minimum in the S_{21} interferogram. The corresponding setup is in the Fig. 4.6b..

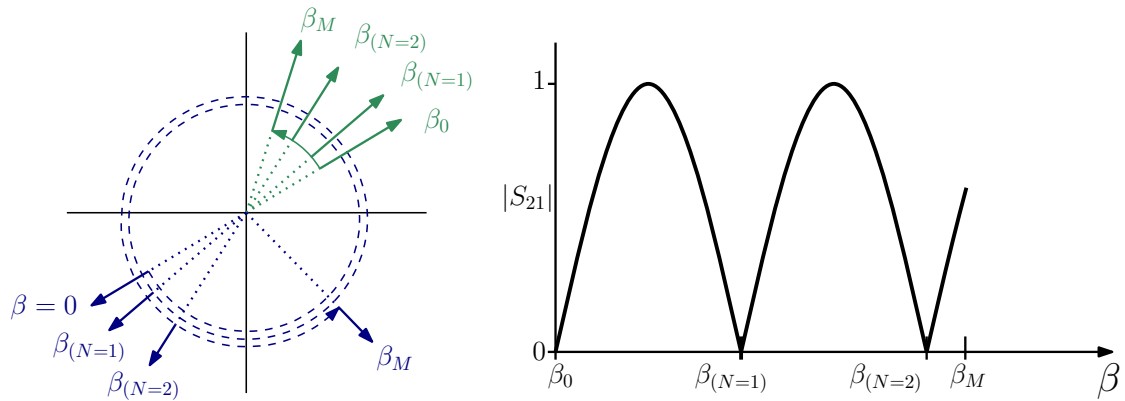


Figure 4.7. Vectors of waves from the *test* (blue) and *reference* (green) channels in the left figure, measured $|S_{21}|$ trace in the right. The case when the vectors differ more than one wavelength.

Let's return to the equation 4.22. It allows to calculate Δl from the frequency at which the minimum was measured and from order (N) of the minimum. The order is counted from zero frequency.

Nevertheless in practice it is usual to measure in a frequency band which might not start in zero. Thus it is impossible to directly enumerate order of minima which are measured.

For the case when the interferogram contains at least two minima, it is possible to determine

Δl and N as well. It is possible to use the following relationship based on 4.22.

$$|l_r - l_t| = \Delta l = \frac{N_i - N_j}{\beta_i - \beta_j} \pi = \frac{\Delta N}{\Delta \beta} \pi \quad (4.23)$$

Where N_i and N_j are the orders of minima and β_i and β_j are the phase coefficients at the frequencies of those minima.

The very similar scenario can be used for S_{11} equation. The solution of 4.17 can be simply used for the equation 4.16. It is only necessary to rewrite equation 4.16 to:

$$0 = e^{-2i\beta(f)l_t} + e^{-2i\beta(f)l_r} \quad (4.24)$$

$$0 = e^{-2i\beta(f)l_t} - e^{i\pi} e^{-2i\beta(f)l_r} \quad (4.25)$$

and remaining steps are the same as was used for previous equations 4.17 – 4.22

$$\Delta l = (l_t - l_r) = \frac{\pi \left(N_t - N_r - \frac{1}{2} \right)}{\beta} \quad (4.26)$$

and it can be simplified to $N = N_t - N_r$ so

$$\Delta l = (l_t - l_r) = \frac{\pi \left(N - \frac{1}{2} \right)}{\beta} \quad (4.27)$$

It's evident, that results for S_{11} and S_{21} measurement are very similar. Theoretical principle is again explained using vector in the Fig. 4.8 and 4.9.

The result 4.23 derived for S_{21} measurement apply also for S_{11} what can be shown using equation 4.27.

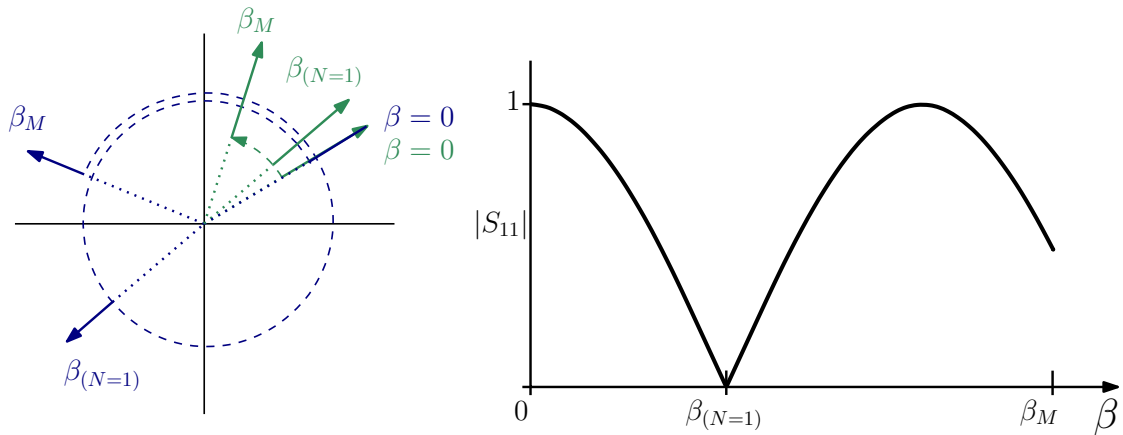


Figure 4.8. Vectors of waves from the *test* (blue) and *reference* (green) channels in the left figure, measured $|S_{11}|$ trace in the right.

The example of evaluation Δl based on measured minima is discussed in the section 4.1.3

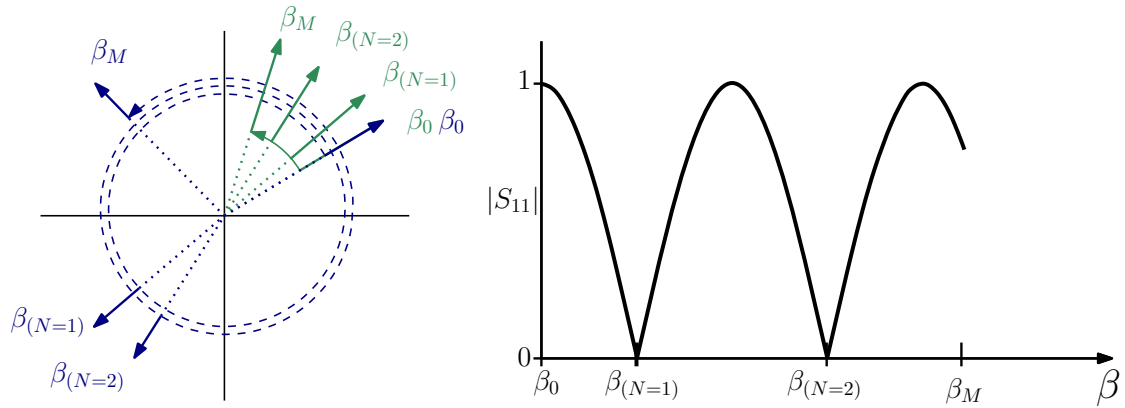


Figure 4.9. Vectors of waves from the *test* (blue) and *reference* (green) channels in the left figure, measured $|S_{11}|$ trace in the right. The case when the vectors differs more then one wavelength.

4.1.2. Terminating impedance

Until this moment, it was supposed that terminating impedances in *reference* and *test channels* are the same $\Gamma_T = \Gamma_R$. This assumption was convenient for derivation of the basic relations. However the effect of the different magnitudes of the reflections has not yet been investigated. It was only mentioned that matching of any channel prevents the interference.

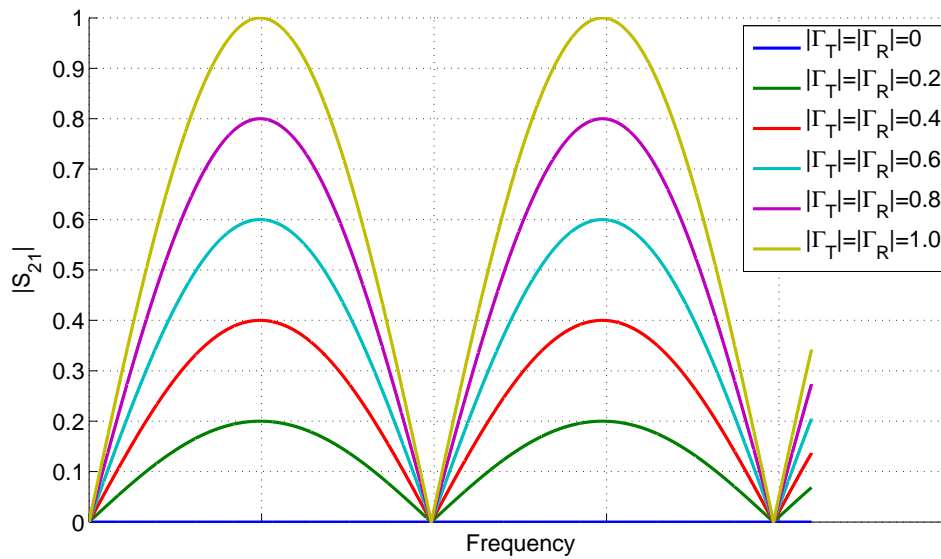


Figure 4.10. Effect of the reflection magnitude in the *test* and *reference* channel.

The following example again assume the ideal behavior of the interferometric system. In the Fig. 4.10 there are $|S_{21}|$ interferograms for the various scenarios. The condition $\Gamma_T = \Gamma_R$ is satisfied for all the measurements, but the magnitude of the reflection coefficient differs. It is evident that thanks to the fulfillment of given condition, there are sharp minima in the all interferograms and the value of the minima is exactly zero. But the maximum values in

interferograms is directly affected by the magnitude of the reflections. Also the steepness of the traces is smaller for the smaller reflection coefficient.

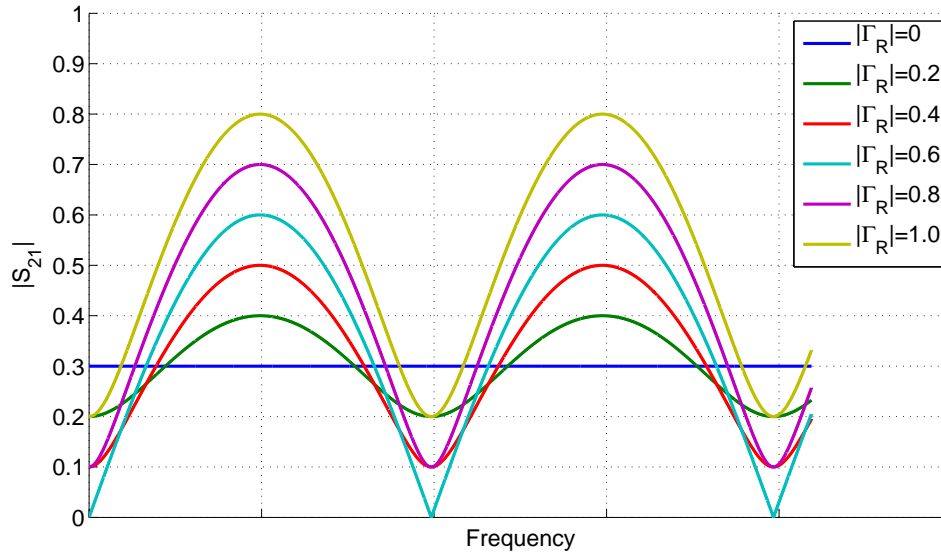


Figure 4.11. Effect of the reflection magnitude in *reference* channel for the case when the $\Gamma_T = 0.6$.

In the following case there is a measurement scenario with fixed reflection in the *test channel* so the magnitude of the reflection is $|\Gamma_R = 0.6|$. Then the aforementioned condition is satisfied only for one case where also *reference channel* reflection has a magnitude of 0.6 as shown in Fig. 4.11. For the other cases where $|\Gamma_R| \neq |\Gamma_T|$, there aren't sharp minima on interferograms. The minima are on identical frequencies but they are more flat and can cause uncertainty during measurement. From those two examples is clear, that for proper interferometric measurement it is need to satisfy at least the condition $|\Gamma_R| = |\Gamma_T|$ otherwise the frequency of the minima may not be clearly identified.

4.1.3. Effects of the finite frequency step size

This example shows the computer simulation using an ideal interferometer. Experiment is simulated in CST Design Studiocircuit simulator. The circuit simulator acts as an ideal VNA, which has no systematic or random errors. There is only one known error is caused by the finite frequency step size. Simulation is performed in the frequency range from $f = 1 \text{ GHz} \div 18 \text{ GHz}$ with 17000 points. It means that there is one simulated point per 1 MHz.

In the circuit there is an ideal 180° hybrid coupler. Two transmission lines (propagating TEM mode) act as *reference (TL1)* and *test channel (TL2)*. The $\Delta l = 40 \text{ mm}$. The lengths of transmission lines *TL1* and *TL2* were chosen randomly.

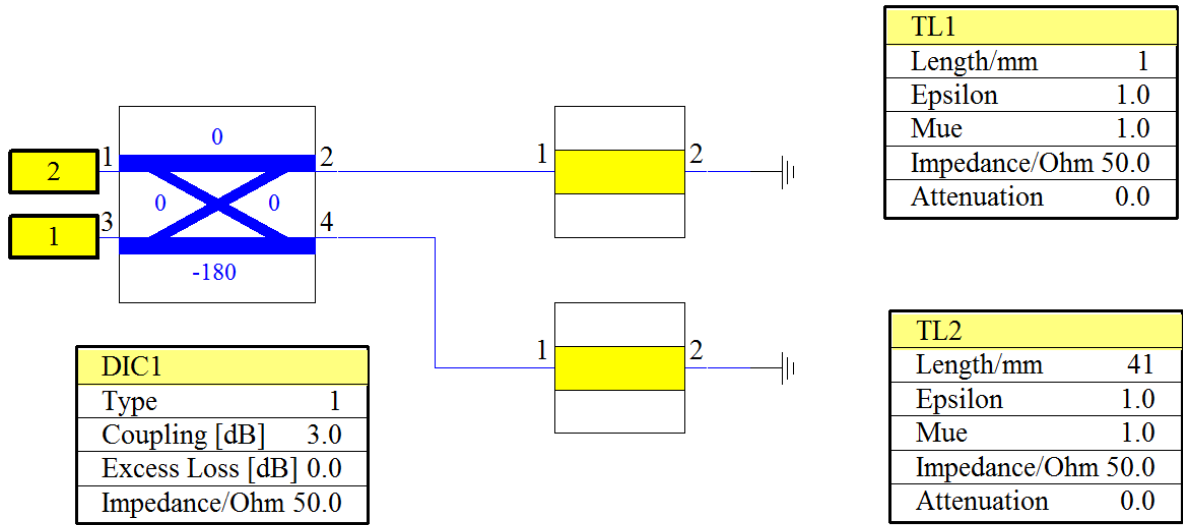


Figure 4.12. Circuit diagram in the CST Design Studio.

Resulting traces of $|S_{11}|$ and $|S_{21}|$ from the simulation are in the Fig.4.14 and 4.13 respectively. Frequencies at which minimum appeared are written to the corresponding table in the order of appearance. Then unknown Δl can be evaluated using 4.27 and 4.22.

Tables 4.2 and 4.1 compare theoretical values with the values obtained from circuit simulator and it also compares results (Δl) calculated from these frequencies. It is evident that the frequencies of the minima in the simulation are interpolated due to coarse frequency step size. One can assume that increasing the number of frequency points in the simulation increase the total precision, but during real measurement using VNA, there is also real limitation of available frequency points.

Increasing the number of frequency points during the real measurement cause a slower measurement which may be critical for some applications. Furthermore, some of VNAs have a limitation to the maximum number of frequency points due to limited resources of the control computer inside.

It is also clear, that real microwave components does not work from zero frequency to microwave band. So contrary this ideal example also bandwidth must be restricted. But then the exact order of visible minima may not be obvious. For these cases the equation 4.23 may be applied.

So in the case there are only two minima in the S_{21} measurement/simulation. It may not be clear their exact order, but it is clear that the difference between order of higher and of the lower minimum is just 1. Thus

$$\Delta l = \pi \frac{N_j - N_i}{\beta_j - \beta_i} = \pi \frac{1}{235.635 - 157.071} = 39.988 \text{ mm} \quad (4.28)$$

where β_j and β_i are the corresponding phase constants for the homogeneous line propagating TEM mode, with $\varepsilon = 1$, for the frequencies 11.232 GHz and 7.4944 GHz.

It is obvious that the result is far away from the expected value. It is a demonstration of the effect of coarse frequency step which is more noticeable here. That is because two minima (each influenced by coarse frequency step) were used for the calculation.

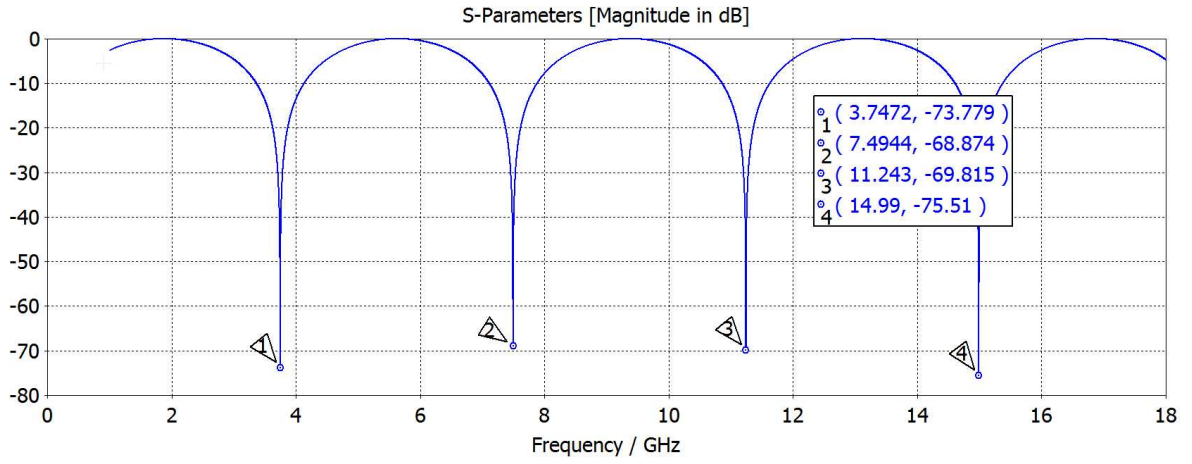


Figure 4.13. $|S_{21}|$ obtained from the simulation with an ideal 180° hybrid coupler.

	Expected value		Circuit simulator 17000 points		$ \delta f $ kHz	$ \delta \Delta l $ μm
	f (Hz)	Δl (mm)	f (Hz)	Δl (mm)		
1	3 747 405 725.00	40.000	3 747 200 000.00	40.002	205.725	≈ 2
2	7 494 811 450.00	40.000	7 494 400 000.00	40.002	411.450	≈ 2
3	11 242 217 175.00	40.000	11 243 000 000.00	39.997	782.852	≈ 3
4	14 989 622 900.00	40.000	14 990 000 000.00	39.998	377.100	≈ 2

Tab. 4.1. Theoretical and simulated values with the finite frequency step size - S_{21} .

	Expected value		Circuit simulator 17000 points		$ \delta f $ kHz	$ \delta \Delta l $ μm
	f (Hz)	Δl (mm)	f (Hz)	Δl (mm)		
1	1 873 702 862.00	40.000	1 874 100 000.00	39.992	397.137	≈ 8
2	5 621 108 587.00	40.000	5 621 300 000.00	39.999	191.412	≈ 1
3	9 368 514 312.00	40.000	9 368 500 000.00	40.000	14.312	< 1
4	13 115 920 037.00	40.000	13 116 000 000.00	39.999	79.962	≈ 1

Tab. 4.2. Theoretical and simulated values with the finite frequency step size - S_{11} .

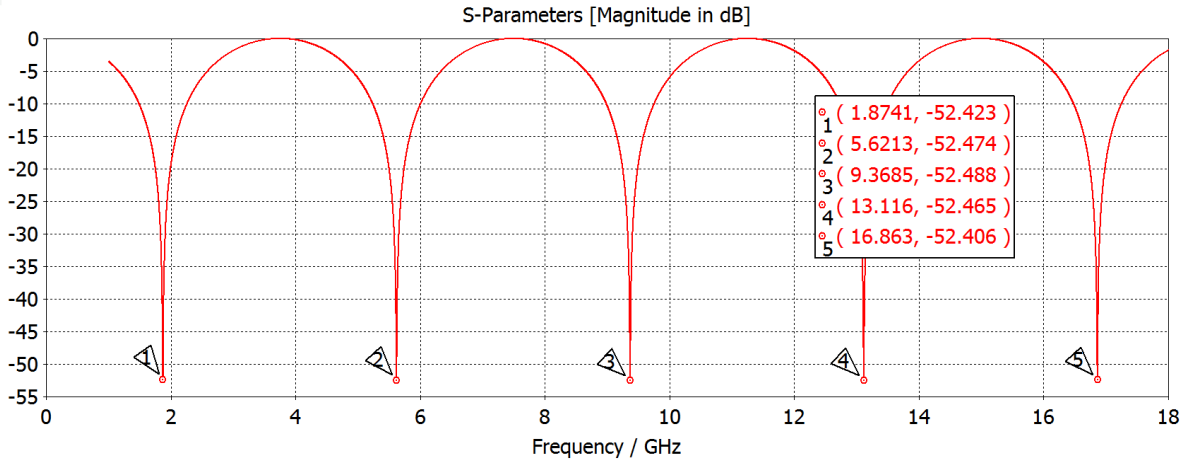


Figure 4.14. $|S_{11}|$ obtained from the simulation with an ideal 180° hybrid coupler.

This example briefly shown the principle of operation of an ideal interferometric system and pointed out the problem of finite frequency step size. Even though there is an ideal model of 180° hybrid coupler without reflections, cross-talks and other problems of real device, it is evident that even frequency step size can significantly affect the results.

4.1.4. Sensitivity analysis

During the design of the interferometric system or experiment, sensitivity analysis should be taken into account. It helps to design best solution (if it is possible) in terms of sensitivity to the measured phase. Obviously the aim is to achieve the greatest sensitivity as possible. So imagine the measurement according to the 4.15. Two identical interferometric setups differ in the physical length of the homogeneous line representing the *test channel*, so resulting $|S_{21}|$ interferograms have minimum slightly shifted about $\Delta\beta$.

The position of the minimum depends on the length difference in *test* and *reference channel* Δl and on the order N as shown in 4.22. Assuming that the order of the minima is still same then by differentiating the equation 4.22, the result 4.29 is obtained

$$\Delta\beta(f) = \frac{d\beta(f)}{d(\Delta l)} = -\frac{N\pi}{(\Delta l)^2} \quad (4.29)$$

This result shows that the sensitivity goes higher for the higher order of the minima N . However sensitivity also depends on $1/(\Delta l)^2$. Let start with first mentioned result. It is

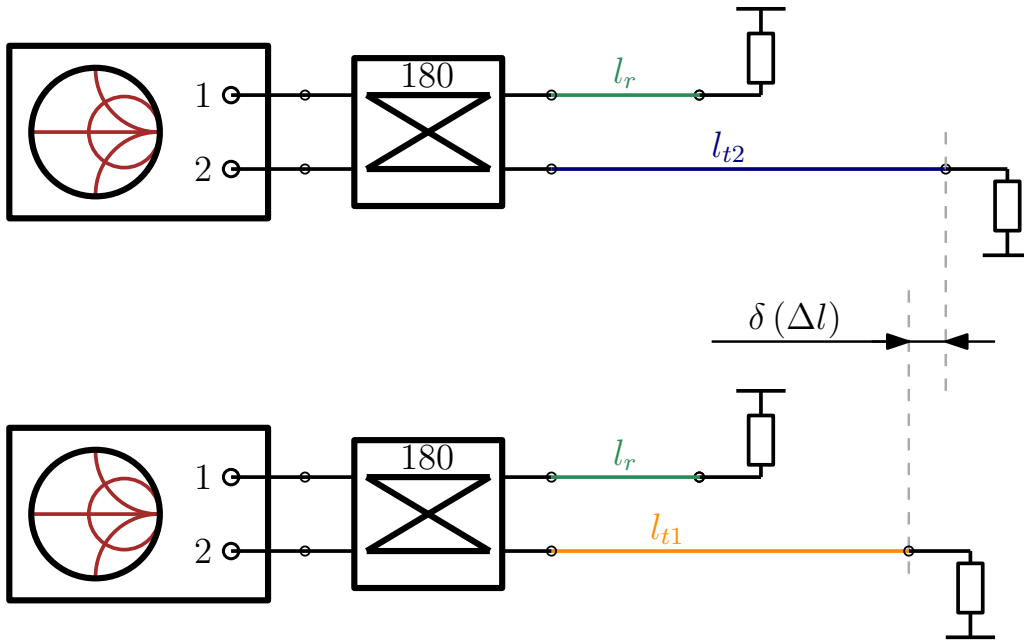


Figure 4.15. Two identical measurements with very small phase change in the *test channel*

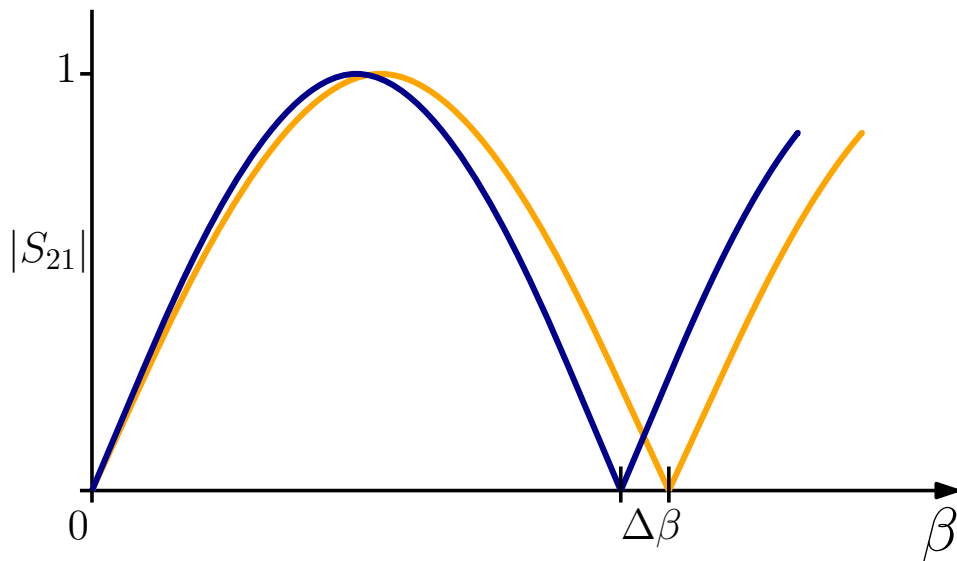


Figure 4.16. $|S_{21}|$ traces showing the frequency of the minima due to small phase change in the *test channel*

clearly shown in the Fig. 4.17. There are two simulations of the S_{21} . Both simulations use an ideal 180° hybrid coupler, identical *reference channel*, but the transmission line in the *test channel* differs in the length. The difference is $\delta\Delta l = 100 \mu\text{m}$. Results in the Fig. 4.17 are in accordance with the equation 4.29. While the frequency shift for the $N = 1$ is $\Delta f = 36.9 \text{ MHz}$, the frequency shift for the next minimum $N = 2$ is $\Delta f = 75 \text{ MHz}$.

At a first glance is evident, that the higher order of minima brings higher sensitivity, but it is not so unambiguous. It is clear that the measurement of the higher order of the minima

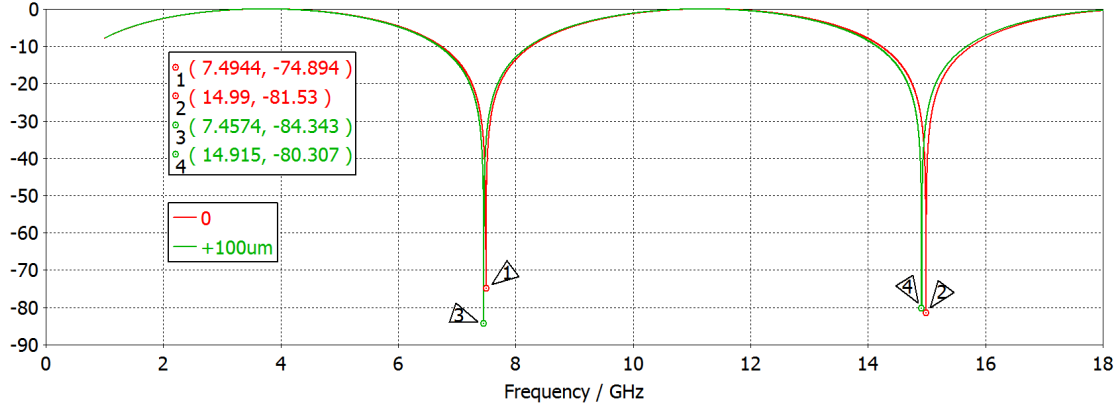


Figure 4.17. $|S_{21}|$ simulated in CST Design Studio assuming an ideal system. The $\delta\Delta l = 100 \mu\text{m}$.

also means measurement on the higher frequency. However, what about the case, when measurement bandwidth is limited?

Now let's assume the system which has limited bandwidth to the $6 \div 8$ GHz. So according to the Fig. 4.17 it is possible to measure only the first minimum. Nevertheless by adjusting the *reference channel* it is possible to shift the second minimum to the desired frequency band. It can be done with the change of the length difference between *reference* and *test channel*. Without any detailed information about this simulation, it can be written that the first minimum occurs for the phase coefficient:

$$\beta(f = 7.5\text{GHz}) = \frac{1\pi}{\Delta l_{7.5\text{GHz}}} \quad (4.30)$$

Now it is clear, that for shifting of the second minimum to the desired band can be done increasing the length difference between *reference* and *test channel* twice.

$$\beta(f = 7.5\text{GHz}) = \frac{1\pi}{\Delta l_{7.5\text{GHz}}} = \frac{2\pi}{2\Delta l_{7.5\text{GHz}}} \quad (4.31)$$

Then the result of such adjusted simulation is in the Fig 4.18, but the sensitivity is even worst! Contrary to the previous simulation the frequency shift $\Delta f = 18$ MHz!

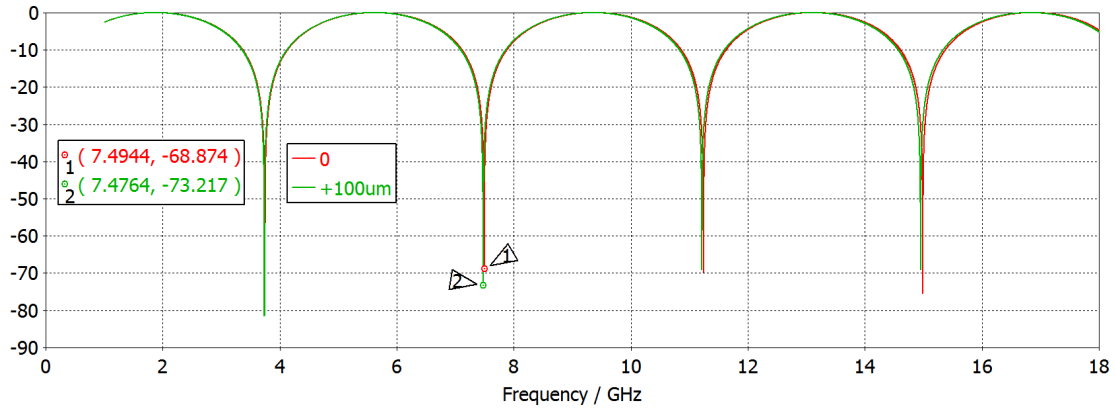


Figure 4.18. $|S_{21}|$ simulated in CST Design Studio assuming an ideal system. The $\delta\Delta l = 100 \mu\text{m}$.

The explanation is in the equation 4.32. The adjusting the second (or higher) minimum to the desired frequency band reduces the sensitivity by $1/N$.

$$\Delta\beta (7.5 \text{ GHz}) = \frac{2\pi}{(2\Delta l_{7.5\text{GHz}})^2} \delta\Delta l = \frac{1}{2} \frac{\pi}{(\Delta l_{7.5\text{GHz}})^2} \delta\Delta l \quad (4.32)$$

Generally it is evident that sensitivity for the case of limited bandwidth is given by following equation

$$\Delta\beta (f) = \frac{1}{N} \frac{\pi}{(\Delta L)^2} \delta\Delta L \quad (4.33)$$

where is clearly shown, that the sensitivity is the best only for the first minimum!

4.2. Ideal 90° interferometer

In this example there is the identical setup as was used in 4.1.3, except the hybrid coupler. In this case there is an ideal 90° hybrid coupler. According to the results it is evident, that the principle also works with this setup. But contrary to example in 4.1.3, the minima are shifted to different frequencies although the physical lengths of *test* and *reference* channels are the same. It is of course due to the fact that 90° hybrid coupler causes different phase shifts in the *reference* and *test* channel.

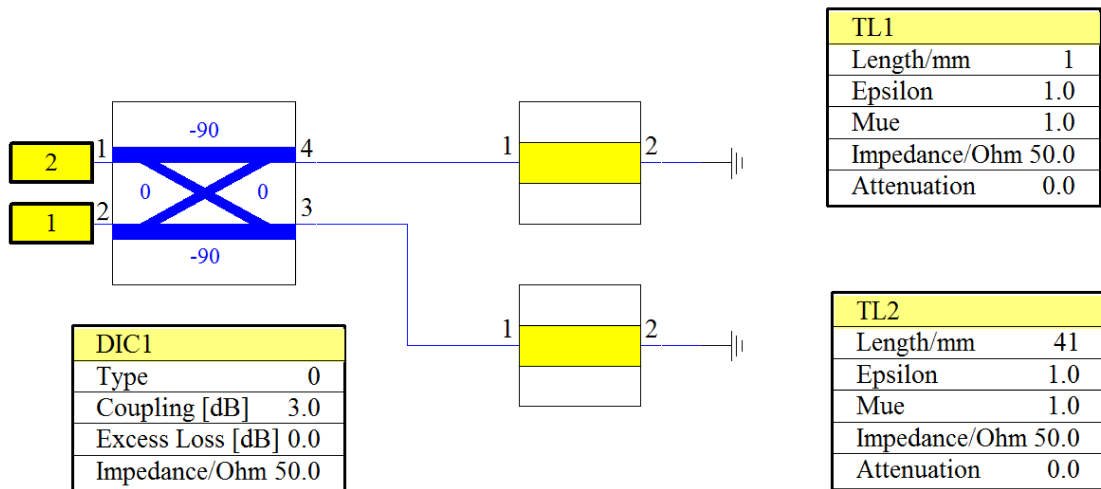


Figure 4.19. Circuit diagram in the CST Design Studio.

The results are in the Fig. 4.20. The effect of the frequency step size is here also evident. Simulated and expected values are in the tables 4.3 and 4.4.

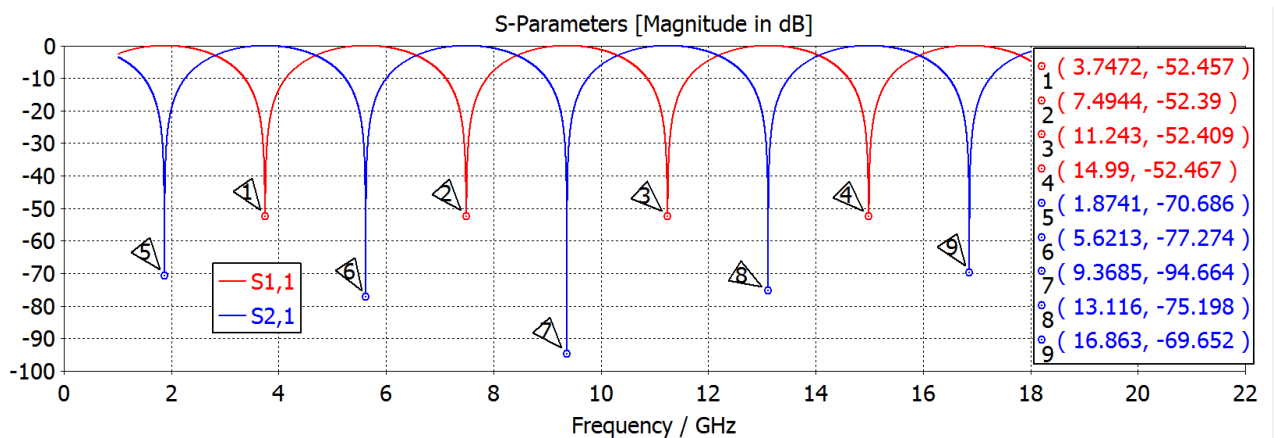


Figure 4.20. $|S_{11}|$ and $|S_{21}|$ obtained from the simulation with an ideal 90° hybrid coupler.

Assuming that the S-matrix of an ideal 90° hybrid coupler is 4.34

$$S_{h90}^{ideal} = \begin{pmatrix} 0 & 0 & -i\frac{1}{\sqrt{2}} & -\frac{1}{\sqrt{2}} \\ 0 & 0 & -\frac{1}{\sqrt{2}} & -i\frac{1}{\sqrt{2}} \\ -i\frac{1}{\sqrt{2}} & -\frac{1}{\sqrt{2}} & 0 & 0 \\ -\frac{1}{\sqrt{2}} & -i\frac{1}{\sqrt{2}} & 0 & 0 \end{pmatrix} \quad (4.34)$$

then without any derivation, the resulting equation describing expected minima in S_{21} measurement is

$$\beta(f)_{21} = \frac{\pi \left(N - \frac{1}{2}\right)}{\Delta l} \quad (4.35)$$

and for S_{11} measurement

$$\beta(f)_{11} = \frac{\pi N}{\Delta l} \quad (4.36)$$

	Expected value		Circuit simulator 17000 points		$ \delta f $ kHz	$ \delta \Delta l $ μm
	f (Hz)	Δl (mm)	f (Hz)	Δl (mm)		
1	3 747 405 725.00	40.000	3 747 200 000.00	40.002	205.725	≈ 2
2	7 494 811 450.00	40.000	7 494 400 000.00	40.002	411.450	≈ 2
3	11 242 217 175.00	40.000	11 243 000 000.00	39.997	782.852	≈ 3
4	14 989 622 900.00	40.000	14 990 000 000.00	39.998	377.100	≈ 2

Tab. 4.3. Theoretical and simulated values with the finite frequency step size - S_{11} .

	Expected value		Circuit simulator 17000 points		$ \delta f $ kHz	$ \delta \Delta l $ μm
	f (Hz)	Δl (mm)	f (Hz)	Δl (mm)		
1	1 873 702 862.00	40.000	1 874 100 000.00	39.992	397.137	≈ 8
2	5 621 108 587.00	40.000	5 621 300 000.00	39.999	191.412	≈ 1
3	9 368 514 312.00	40.000	9 368 500 000.00	40.000	14.312	< 1
4	13 115 920 037.00	40.000	13 116 000 000.00	39.999	79.962	≈ 1

Tab. 4.4. Theoretical and simulated values with the finite frequency step size - S_{21} .

This example serves as a proof that not only 180° hybrid coupler can be used for the interferometry purposes. The detailed derivation is not done for this case, because it would be very similar to the presented derivation for the 180° hybrid coupler.

4.3. Ideal 3dB divider interferometer

Here is presented the simulation of the 3 dB divider used as an interferometer. This example should serve only as a proof, that it is possible to use this circuit for the interferometry measurement. Since the *reference* and *test channels* are identical as in the simulation 4.1.3 the S_{11} results are the same as for the 180° hybrid coupler. It applies for the case that the circuit is ideal and its S-matrix is 4.37.

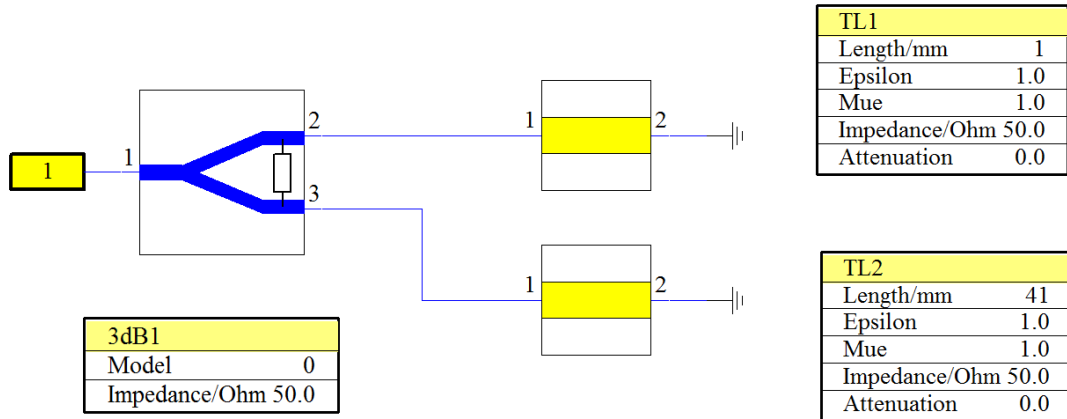


Figure 4.21. Circuit diagram in the CST Design Studio.

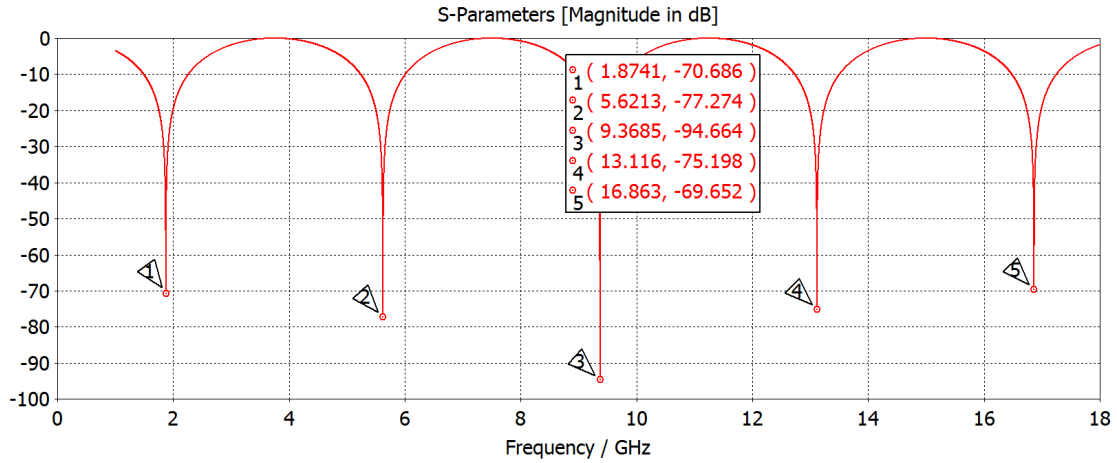


Figure 4.22. $|S_{11}|$ obtained from the simulation with an ideal 3 dB divider.

$$S_{div3dB}^{ideal} = \begin{pmatrix} 0 & \frac{-i}{\sqrt{2}} & \frac{-i}{\sqrt{2}} \\ \frac{-i}{\sqrt{2}} & 0 & 0 \\ \frac{-i}{\sqrt{2}} & 0 & 0 \end{pmatrix} \quad (4.37)$$

4.4. Non-ideal hardware

Until this moment, only ideal scenarios were discussed. According to issues discussed in the 2.3 it is evident that non-ideality of the real components causes systematic errors which lead to incorrect evaluation of measured phase. Here will be discussed several different scenarios that will reveal the influence of various parasitic parameters. Prior that, the general model will be proposed for a better comprehension the influence of parasitic properties.

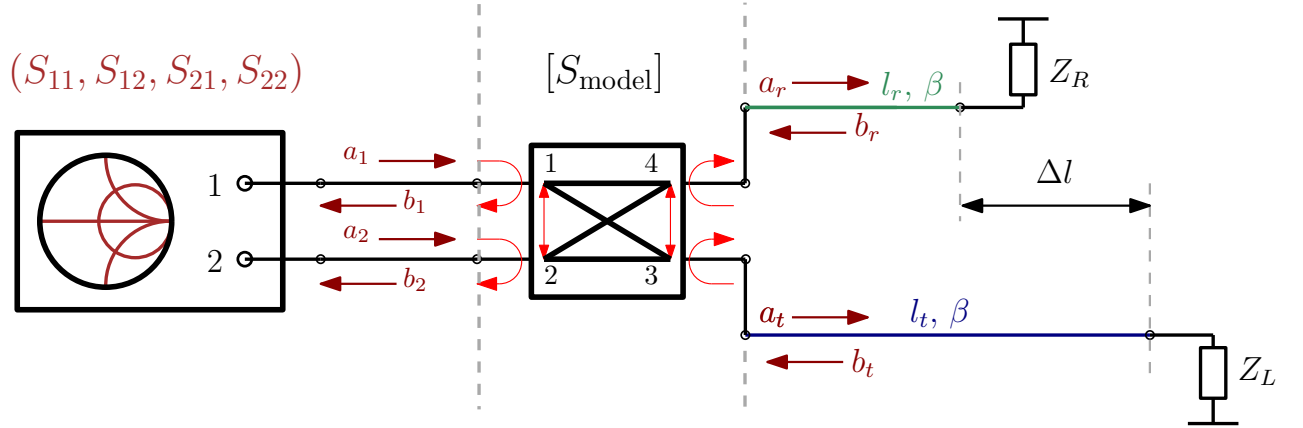


Figure 4.23. Measurement scenario with the non-ideal system where all parasitic terms are present.

Consider a general case when the interferometer is a four port device as shown in the Fig. 4.23. Two ports are used for the interconnection with the VNA and the remaining ports are used for the *test* and *reference channel*. The interferometer itself can be described using scattering matrix 4.38.

Scattering parameters in this matrix are marked as m_{jk} to be not confused with S_{jk} which represent scattering parameters measured by the VNA in the measurement setup. Thus, the terms $m_{13}, m_{14}, m_{23}, m_{24}$ and $m_{31}, m_{41}, m_{32}, m_{42}$ represent the direct paths in the interferometer – these are the only terms assumed for the ideal behavior, whereas m_{12}, m_{34} and m_{21}, m_{43} are the cross-talks whose values are usually much smaller in compare with the direct paths but for the sensitive interferometry technique their effect is very significant as will be presented. Finally the reflections on the ports are $m_{11}, m_{22}, m_{33}, m_{44}$.

$$S_{\text{model}} = \begin{pmatrix} m_{11} & m_{12} & m_{13} & m_{14} \\ m_{21} & m_{22} & m_{23} & m_{24} \\ m_{31} & m_{32} & m_{33} & m_{34} \\ m_{41} & m_{42} & m_{43} & m_{44} \end{pmatrix} \quad (4.38)$$

The advantage of this general model is, that it is applicable to an interferometer consisting of a 180° or 90° hybrid coupler as well as to any more complicated system consisting of multiple components. Based on this it can be derived the general formulation for any S-parameter measurement with an arbitrary interferometer.

4.4.1. The full 16-term model

The full 16-term model includes all parameters of an four port interferometer as written in the matrix 4.39. The signal flow graph for a four port interferometer is shown in the Fig. 4.24. The equations describing S_{11} and S_{21} measurement are 4.40 and 4.41. The all equations for the all four S-parameters are in the appendix A.1. Although, these equations represents full model of an four port interferometric system, they serve more like presentation of the complexity of the problem. However, the equation 4.40 points to the fact, that S_{11} measurement is not affected by m_{12} , m_{21} cross-talks. This information can be useful for the design of an interferometric system or for the design of an experiment. Contrary to this, the S_{21} measurement is affected by the all parasitic cross-talks as evident from the equation 4.41.

$$S_{\text{model}} = \begin{pmatrix} m_{11} & m_{12} & m_{13} & m_{14} \\ m_{21} & m_{22} & m_{23} & m_{24} \\ m_{31} & m_{32} & m_{33} & m_{34} \\ m_{41} & m_{42} & m_{43} & m_{44} \end{pmatrix} \quad (4.39)$$

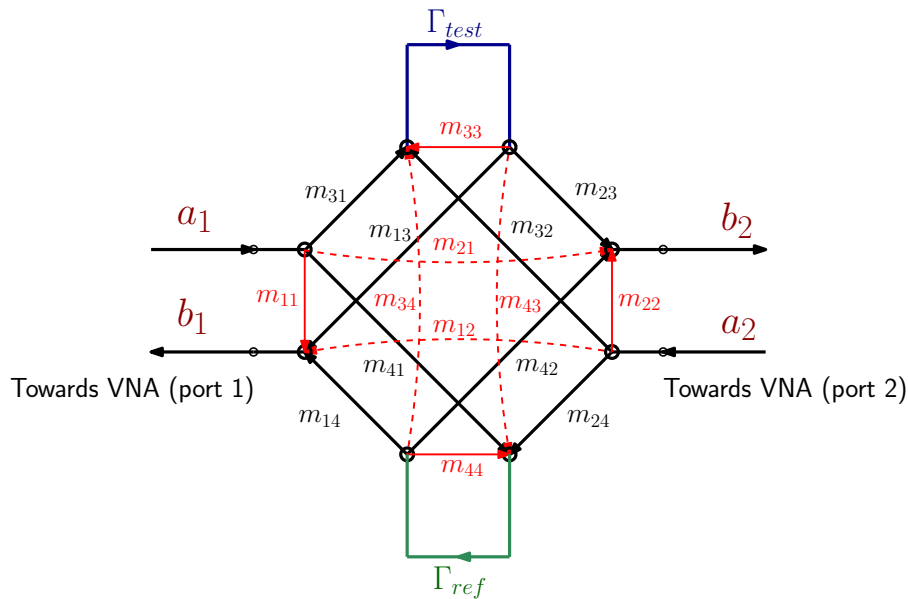


Figure 4.24. Flow graph for the full 16-term model of the interferometer.

$$\begin{aligned}
S_{11} = & -\frac{m_{11} - \Gamma_{test}m_{11}m_{33} + \Gamma_{test}m_{13}m_{31}}{\Gamma_{test}m_{33} + \Gamma_{ref}m_{44} - \Gamma_{ref}\Gamma_{test}m_{33}m_{44} + \Gamma_{ref}\Gamma_{test}m_{34}m_{43} - 1} \\
& +\frac{-\Gamma_{ref}m_{11}m_{44} + \Gamma_{ref}m_{14}m_{41} + \Gamma_{ref}\Gamma_{test}m_{11}m_{33}m_{44}}{\Gamma_{test}m_{33} + \Gamma_{ref}m_{44} - \Gamma_{ref}\Gamma_{test}m_{33}m_{44} + \Gamma_{ref}\Gamma_{test}m_{34}m_{43} - 1} \\
& +\frac{-\Gamma_{ref}\Gamma_{test}m_{11}m_{34}m_{43} - \Gamma_{ref}\Gamma_{test}m_{13}m_{31}m_{44}}{\Gamma_{test}m_{33} + \Gamma_{ref}m_{44} - \Gamma_{ref}\Gamma_{test}m_{33}m_{44} + \Gamma_{ref}\Gamma_{test}m_{34}m_{43} - 1} \\
& +\frac{\Gamma_{ref}\Gamma_{test}m_{13}m_{34}m_{41} + \Gamma_{ref}\Gamma_{test}m_{14}m_{31}m_{43}}{\Gamma_{test}m_{33} + \Gamma_{ref}m_{44} - \Gamma_{ref}\Gamma_{test}m_{33}m_{44} + \Gamma_{ref}\Gamma_{test}m_{34}m_{43} - 1} \\
& +\frac{-\Gamma_{ref}\Gamma_{test}m_{14}m_{33}m_{41}}{\Gamma_{test}m_{33} + \Gamma_{ref}m_{44} - \Gamma_{ref}\Gamma_{test}m_{33}m_{44} + \Gamma_{ref}\Gamma_{test}m_{34}m_{43} - 1}
\end{aligned} \tag{4.40}$$

$$\begin{aligned}
S_{21} = & -\frac{m_{21} - \Gamma_{test}m_{21}m_{33} + \Gamma_{test}m_{23}m_{31} - \Gamma_{ref}m_{21}m_{44} + \Gamma_{ref}m_{24}m_{41}}{\Gamma_{test}m_{33} + \Gamma_{ref}m_{44} - \Gamma_{ref}\Gamma_{test}m_{33}m_{44} + \Gamma_{ref}\Gamma_{test}m_{34}m_{43} - 1} \\
& +\frac{\Gamma_{ref}\Gamma_{test}m_{21}m_{33}m_{44} - \Gamma_{ref}\Gamma_{test}m_{21}m_{34}m_{43}}{\Gamma_{test}m_{33} + \Gamma_{ref}m_{44} - \Gamma_{ref}\Gamma_{test}m_{33}m_{44} + \Gamma_{ref}\Gamma_{test}m_{34}m_{43} - 1} \\
& +\frac{-\Gamma_{ref}\Gamma_{test}m_{23}m_{31}m_{44} + \Gamma_{ref}\Gamma_{test}m_{23}m_{34}m_{41}}{\Gamma_{test}m_{33} + \Gamma_{ref}m_{44} - \Gamma_{ref}\Gamma_{test}m_{33}m_{44} + \Gamma_{ref}\Gamma_{test}m_{34}m_{43} - 1} \\
& +\frac{\Gamma_{ref}\Gamma_{test}m_{24}m_{31}m_{43} - \Gamma_{ref}\Gamma_{test}m_{24}m_{33}m_{41}}{\Gamma_{test}m_{33} + \Gamma_{ref}m_{44} - \Gamma_{ref}\Gamma_{test}m_{33}m_{44} + \Gamma_{ref}\Gamma_{test}m_{34}m_{43} - 1}
\end{aligned} \tag{4.41}$$

4.4.2. The reciprocal model with omitted reflections

Although the full 16-term model provides a complete description of the problem it may be inappropriate for the calibration or data evaluation, because of its complexity. If the interferometer is a passive reciprocal circuit the model can be simplified in the way that $m_{ij} = m_{ji}$. For the further simplification the reflections coefficients are omitted for this model. The matrix describing this model is 4.42 and signal flow graph in the Fig. 4.25. Corresponding equations for the S_{21} and S_{11} measurements are 4.44 and 4.43 respectively.

$$S_{\text{model}} = \begin{pmatrix} 0 & m_{12} & m_{13} & m_{14} \\ m_{12} & 0 & m_{23} & m_{24} \\ m_{13} & m_{23} & 0 & m_{34} \\ m_{14} & m_{24} & m_{34} & 0 \end{pmatrix} \tag{4.42}$$

$$S_{11} = -\frac{\Gamma_{test}m_{13}^2 + 2\Gamma_{ref}\Gamma_{test}m_{34}m_{13}m_{14} + \Gamma_{ref}m_{14}^2}{\Gamma_{ref}\Gamma_{test}m_{34}^2 - 1} \tag{4.43}$$

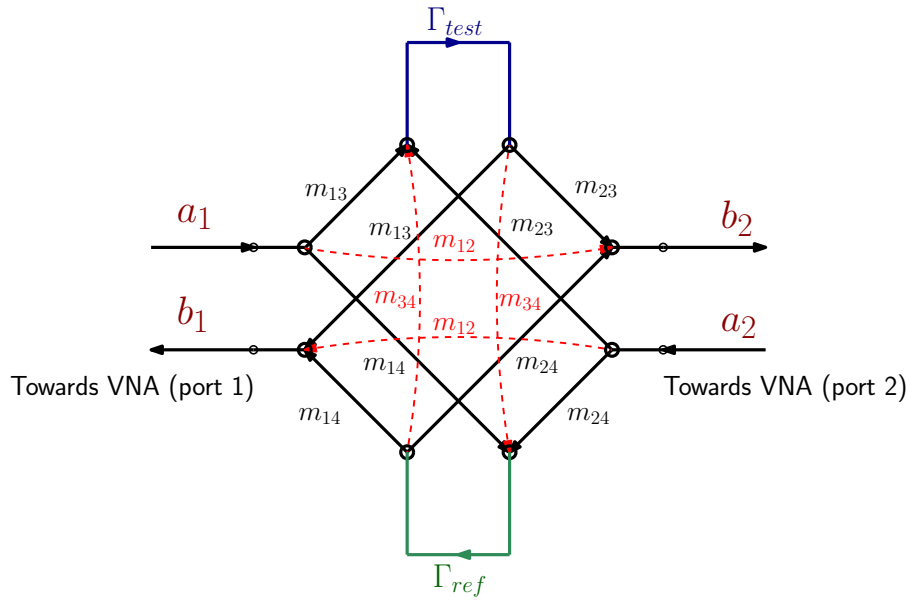


Figure 4.25. Flow graph for the reciprocal model with omitted reflections

$$S_{21} = m_{21} - \frac{m_{34}(\Gamma_{ref}\Gamma_{test}m_{13}m_{24} + \Gamma_{ref}\Gamma_{test}m_{14}m_{23})}{\Gamma_{ref}\Gamma_{test}m_{34}^2 - 1} + \frac{\Gamma_{test}m_{13}m_{23} + \Gamma_{ref}m_{14}m_{24}}{\Gamma_{ref}\Gamma_{test}m_{34}^2 - 1} \quad (4.44)$$

4.4.3. Influence of parasitic terms to the result

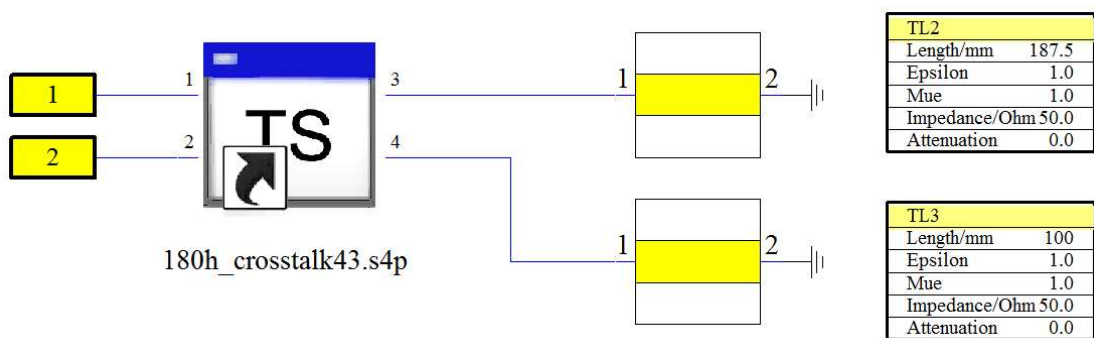


Figure 4.26. Circuit simulation in CST Design Studio.

In the following simulations the 180° hybrid coupler will be investigated, but the results are valid for 90° hybrid coupler as well. The scenarios were simulated in CST Design Studio assuming the interferometer setups are described by matrices 4.45, 4.46, 4.47 and the values of the all scattering parameters in these matrices are constant over the frequency.

For the all setups, the identical homogeneous lines were connected to the test and reference

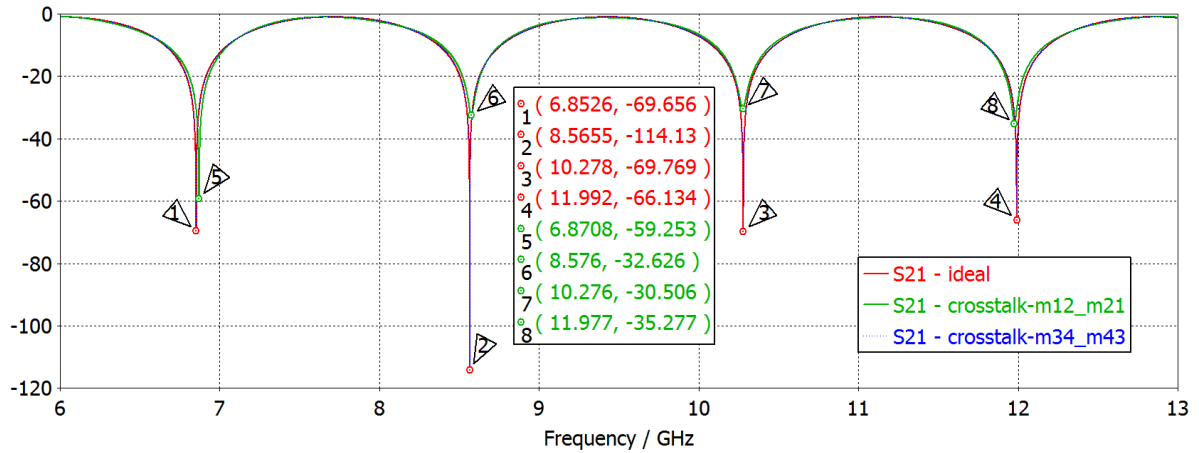


Figure 4.27. Simulated $|S_{21}|$ (dB) traces for an ideal and non-ideal cases of interferometric system.

N	Ideal f_{ideal} (GHz)	Including cross-talks			
		m_{12}, m_{21}		m_{34}, m_{43}	
		f_{m12} (GHz)	$f_{m21} - f_{ideal}$ (MHz)	f_{m34} (GHz)	$f_{m34} - f_{ideal}$ (MHz)
1	6.8526	6.8708	18.2	6.8526	0
2	8.5655	8.576	10.5	8.5655	0
3	10.278	10.276	-2.0	10.278	0
4	11.992	11.997	5.0	10.992	0

Tab. 4.5. Comparison of cancellation frequencies of S_{21} simulations.

port of the interferometer. Figure 4.27 shows simulated traces of $|S_{21}|$ for this three mentioned cases. The red curve represents the ideal case. This is the case when the scattering matrix of the interferometer corresponds to the matrix 4.45. In the two remaining cases the interferometer contains a parasitic cross-talks. The green curve represents case according to the matrix 4.46. Where $P_1 < \frac{1}{\sqrt{2}}$ and $C_1 = 0.03 \angle 60^\circ$ which is roughly -30 dB. This value was selected based on experiences with various interferometric systems. This value can be higher or lower for some specific cases. The goal of this example is generally shows the effect of such cross-talk. Finally the blue curve is for the case, when scattering matrix 4.47 is used. This example clearly shows that the presence a non-zero values in the terms m_{12}, m_{21} cause the significant systematic error in S_{21} measurement, while the presence of the terms m_{34}, m_{43} does not affect $|S_{21}|$ measurement. The frequency of the minima are listed in the tab. 4.5. This table clearly depicts the effects of cross-talks in the interferometer. Nevertheless in these cases all reflection were omitted, but it points to the effects of the cross-talks.

$$S_{h180}^{ideal} = \begin{pmatrix} 0 & 0 & \frac{1}{\sqrt{2}} & \frac{-1}{\sqrt{2}} \\ 0 & 0 & \frac{1}{\sqrt{2}} & \frac{1}{\sqrt{2}} \\ \frac{1}{\sqrt{2}} & \frac{1}{\sqrt{2}} & 0 & 0 \\ \frac{-1}{\sqrt{2}} & \frac{1}{\sqrt{2}} & 0 & 0 \end{pmatrix} \quad (4.45)$$

$$S_{h180}^{ct_{12}} = \begin{pmatrix} 0 & C_1 & P_1 & -P_1 \\ C_1 & 0 & P_1 & P_1 \\ P_1 & P_1 & 0 & 0 \\ -P_1 & P_1 & 0 & 0 \end{pmatrix} \quad (4.46)$$

$$S_{h180}^{ct_{34}} = \begin{pmatrix} 0 & 0 & P_1 & -P_1 \\ 0 & 0 & P_1 & P_1 \\ P_1 & P_1 & 0 & C_1 \\ -P_1 & P_1 & C_1 & 0 \end{pmatrix} \quad (4.47)$$

Contrary to the $|S_{21}|$ simulation, the Fig 4.28 shows that $|S_{11}|$ measurement is not affected by m_{12}, m_{21} , while cross-talks m_{34}, m_{43} play a major role for $|S_{11}|$ results as shown in the detail 4.29.

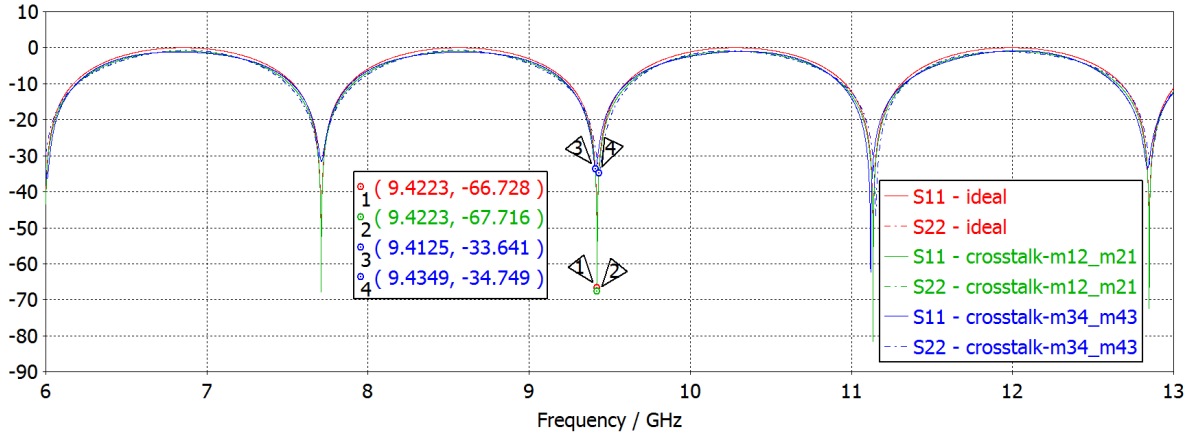


Figure 4.28. Simulated $|S_{11}|$ (dB) traces for an ideal and non-ideal cases of interferometric system

The almost realistic case is described in the matrix 4.48. Here, only cross-talks m_{12}, m_{21} are omitted. While the cross-talks m_{34}, m_{43} and direct paths are the same with the previous cases, there are additional reflections on the all ports and each reflection has different value but all values are in the range $-18 \div -22$ dB. The resulting $|S_{21}|$ is compared with the ideal case in the Fig. 4.30. At first glance, it is clear that the results are different. Values $|S_{21}| > -20$ dB differ definitely. But the position of minima are the same. This is very

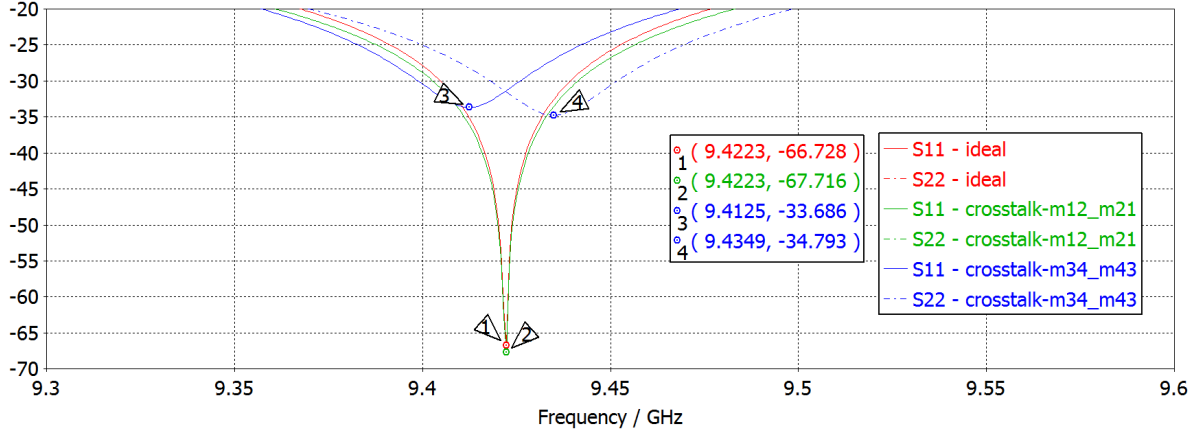


Figure 4.29. Detail of simulated $|S_{11}|$ (dB) traces for an ideal and non-ideal cases of interferometric system.

important result. Even if the entire interferometer include parasitic properties, the existence of cross-talks m_{12}, m_{21} has the crucial influence on the S_{21} measurement even the value of cross-talks is small.

$$S_{h180}^{ct_{12}omitt} = \begin{pmatrix} R_1 & 0 & P_1 & -P_1 \\ 0 & R_2 & P_1 & P_1 \\ P_1 & P_1 & R_3 & C_1 \\ -P_1 & P_1 & C_1 & R_4 \end{pmatrix} \quad (4.48)$$

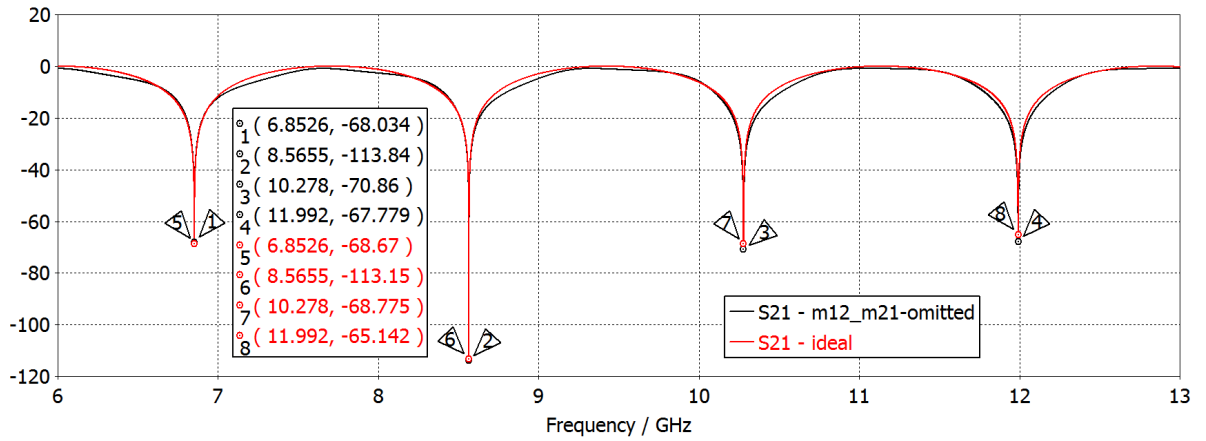


Figure 4.30. Simulated $|S_{21}|$ (dB) traces for an ideal case and case where only cross-talks m_{12}, m_{21} are omitted.

5. System calibration

The usage of the calibration techniques is an integral part of the any precise measurement using the VNA. The aim of the calibration techniques is to get rid of systematic errors in the measurement process. Systematic errors are mainly caused by non-ideal hardware of the VNA. Historically, the importance of the calibration techniques arose after the first VNA was introduced. The most common calibration technique is *open-short-match*, which was designed for the calibration of the 1-port VNA. It assumes that all standards are very well known. Basically it means that the measurement result is strongly dependent on the precise knowledge of the actual reflection coefficient of all the standards. If this condition is met, the calibration technique exactly evaluates the error model of the VNA and, therefore, all the following measurements are free of systematic errors [36, 37],[38]. Nevertheless, in the practice it may be very tricky to meet this condition. Leaving aside the fact that characterization of the standards is very difficult process, there are still another obstacles which can affect the measurement process even if the definition values of the standards are in perfect agreement with the actual values.

Repeatability of the connection cause that every time the standard is connected to the VNA, the measured value contains a small random error and thus the VNA measures the different value then the actual one [39, 40],[1]. It leads to incorrect error model evaluation and thus to incorrect measurement. Nevertheless, during the measurement with the VNA the repeatability effects are usually small and they are usually neglected. Contrary to the calibration techniques which require the precise knowledge of the actual parameters of the standards, there are techniques which does not require precise knowledge about standards [41],[42],[43] such as *thru-reflect-line* or *unknown thru*. They can evaluate the error model (or its part) just based on the measurement. Parameters of standards are used only for the root selection purposes, because there are equations which produce multiple solutions and thus it is necessary to choose proper one. But numerically it is calculated just from the measured data. No definition data enters to the computation process. This makes these calibration techniques a more robust [44, 45], but they are not resistant to random errors due to repeatability.

However, there are techniques that are trying to deal with the repeatability problems. One of such a technique is the *Multiline-TRL* calibration [46, 47]. This technique offers the possibility of measuring more standards, than would be required to calculate the error model. It can be said that this technique uses overdetermined set of input data. Based on this, it is possible to deal repeatability problems.

Basically, this knowledge led to design of the calibration technique for the interferometer. The proposed calibration technique also trying to deal with random errors using an overdetermined set of data.

5.1. Model based auto-calibration

The proposed calibration technique takes into account the known issues with interferometry measurements. Since all these interferometry techniques are very sensitive, all repeatability effects play bigger role in contrast to ordinary VNA measurement. This technique does not require precise knowledge about the standards and use overdetermined set of data as well.

This technique is not only a calibration technique in the meaning of the procedure which is used for error model computation. This technique is so-called auto calibration technique because it can deal with the systematic errors and determine the error model, however, it also returns the information about the used calibration standards as well. Basically it means that it is not necessary to have fully known calibrations standards for the calibration. It is important for this technique to have a proper frequency dependent model of the calibration standard. But values of parameters of such a model may not be known exactly. The exact values are found during the calibration process.

In the comparison with the common calibration techniques, this technique does not calculate the error model analytically using linear equations. In this technique the non-linear least squares optimization is used for the curve fitting. Therefore it is very important for this technique to use data over the entire frequency range.

So the goal is to minimize the sum according to the equation 5.49.

$$E = \sum_{k=1}^q W_k(f) (r_k(f))^2 \quad (5.49)$$

where q is number of the measurements and

$$r_k(f) = S_k(f) - g\left(m_{ij}(f), \Gamma_k^{test}(f), \Gamma_k^{ref}(f)\right) \quad (5.50)$$

where the $g(\dots)(f)$ is the function describing the one measurement using interferometer. Generally $m_{ij}(f)$ are the error terms ($m_{11}(f), m_{12}(f), \dots, m_{44}(f)$) of the interferometer model. $\Gamma^{test}(f)$ and $\Gamma^{ref}(f)$ are the frequency dependent models of standards used in the *test* and *reference channel*, respectively. In this chapter will be shown an example where standards used for the calibration are the offset shorts, thus $\Gamma^{test}(f)$ as well as $\Gamma^{ref}(f)$ will be described using a lossless model of the homogeneous line with only one unknown parameter - the length.

S_i is one of measured S-parameters. Usually it is S_{21} , but as it was shown in this work, it is possible to use S_{11} as well. Or it is also possible to use more then one root function and optimize the problem based on the measured S_{21} and S_{11} .

Finally, the W_i is the weighting coefficient which takes into account the nature of measured data. It is described in the Fig. 5.31. The minima are measured with the smallest uncertainty, but there is very strong effect of the finite frequency step-size, so here the uncertainty is given by the coarseness of the frequency step-size. Therefore the data which are close to the minima should be weighted using smaller weighting coefficient because they can produce higher uncertainty in the results. Contrary to this, the data in the area where the trace of $|S_{21}|$ is below the certain limit are still measured with sufficient uncertainty as shown in Fig. 3.15. Moreover, the number of frequency points does not affect the slope of the curve, so the data in this area are very suitable for the fitting. The area where the trace of $|S_{21}|$ is above a certain limit is measured with the high uncertainty as was shown in Fig. 3.16, so data in this region should be also weighted using smaller weighting coefficient. The mentioned

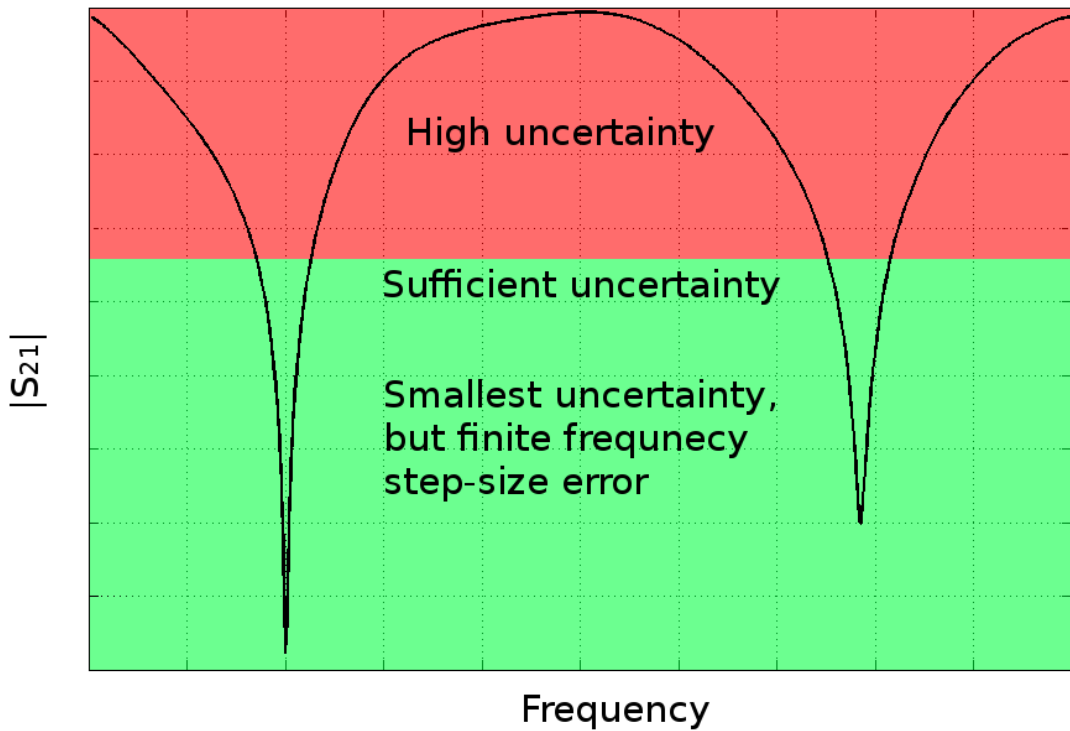


Figure 5.31. Uncertainty areas in S_{21} measurement.

limit mainly depends on the VNA. According to the datasheet values for the R&S ZVA67, this limit is ≈ -10 dB.

During the calibration process the parameters of the function $g(\dots)(f)$ are optimized to minimize differences compared to measurement. Although the exact parameters of the standards are not known or are incorrectly characterized, it is possible to determine their parameters more accurately. The same applies for the error model of the interferometer.

5.2. Experimental verification

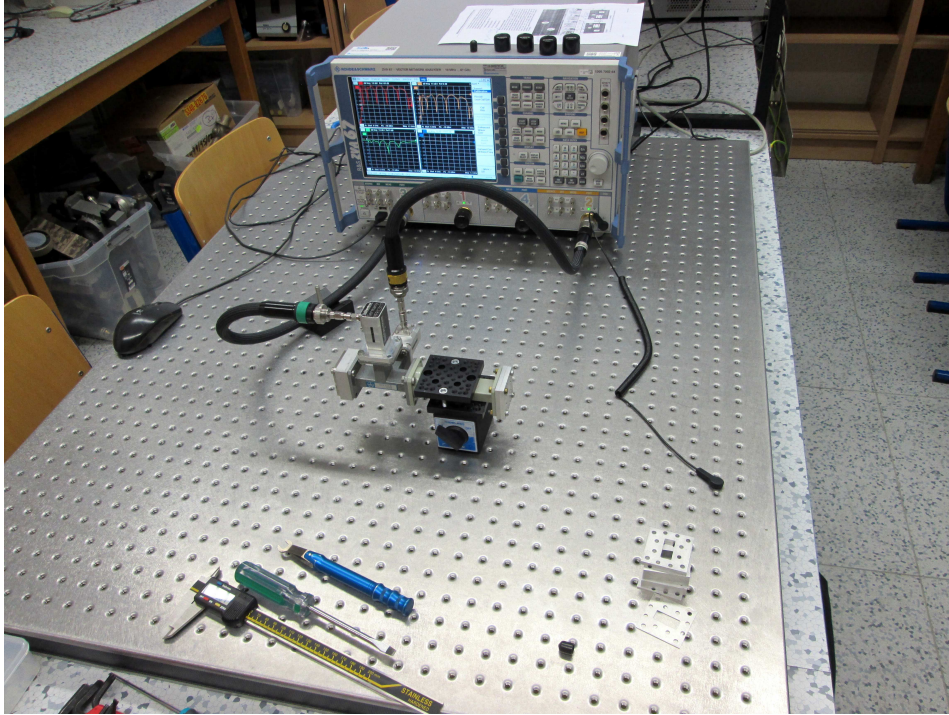


Figure 5.32. Experimental verification using VNA and WR90 interferometer.

The proposed calibration technique was experimentally verified on the interferometry system assembled from WR90 waveguide components. As an interferometer itself the WR90 180° hybrid coupler was used. As a *reference* and *test channel* the short-circuited segments of WR90 were used. The length of the segment used for the *reference channel* was chosen so that there were at least two minima in the measured frequency range. It was because of the possibility to evaluate the measured data using proposed calibration technique as well as idealized approach discussed in 4.1.1.

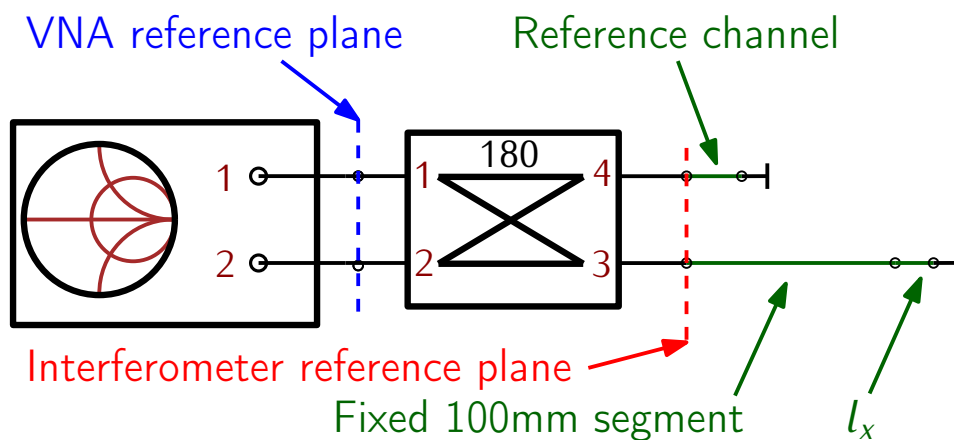


Figure 5.33. Experimental verification — measurement setup.

The VNA R&S ZVA67 was used for the entire experiment as shown in the Fig. 5.32. The VNA was connected to the waveguide transitions and it was calibrated using the TRL technique in the planes of the waveguide transitions as can be seen in the detail in the Fig. 5.34 and 5.33. The measured frequency range was $8 \div 10$ GHz, the power level on the VNA was set to -10 dBm and RBW filter was set to 10 Hz; exactly the same conditions for which the datasheet uncertainties are valid. Since the span was 2 GHz the number of measured points was chosen as 20000 so the frequency step was 100 kHz per frequency point. Thanks to this very fine setting the time required for one measurement sweep was about 30 minutes!

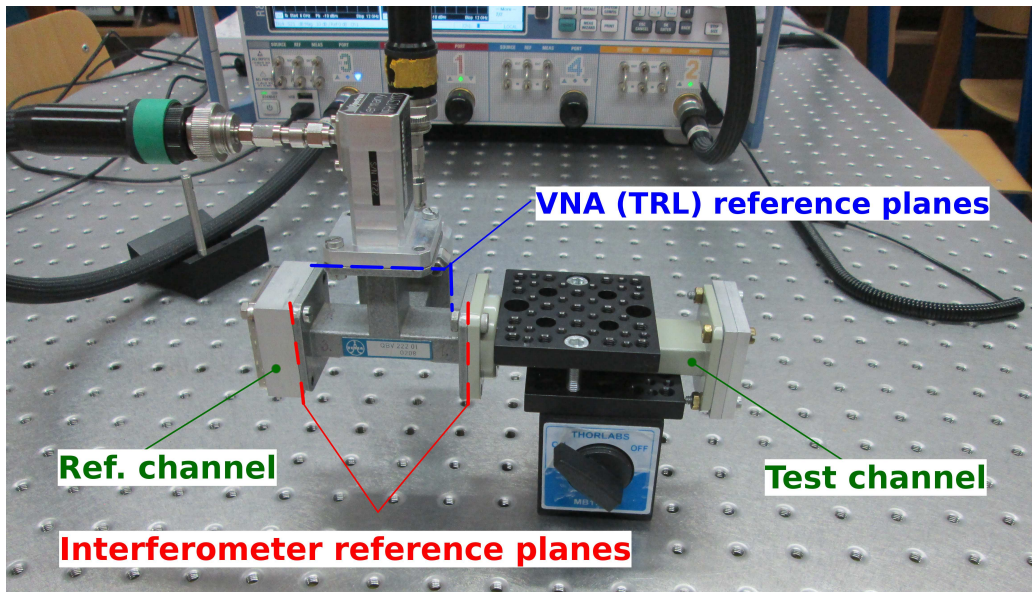


Figure 5.34. Experimental verification — setup in detail

The *reference channel* was fixed for the experiment duration. In the test port there was fixed WR90 line of length 100 mm. Then the further various WR90 segments (listed in table 5.7) were connected to the end of this line. So seven different measurements were performed exactly in the accordance with the table 5.6. The lengths of the WR90 segments were measured using a mechanical caliper, but the uncertainty of the measurement using this caliper was neglected. Entire system was fixed on the table, to avoid any movement with the phase stable cables of the VNA. Segments were mounted using torque screwdriver. Thanks to this the random errors were reduced in maximum extent possible. The all measured S-parameters for the one measurement are shown in the Fig. 5.35. The remaining results are in the appendix A.3.

Setup no.	Reference channel (mm)	Test channel (mm)	WR90 segments used
1	14.980	100.880	100 + 1
2	14.980	101.900	100 + 2
3	14.980	104.870	100 + 5
4	14.980	109.980	100 + 10
5	14.980	114.980	100 + 15
6	14.980	149.940	100 + 50
7	14.980	99.990	100 + 0

Tab. 5.6. Measured set-ups.

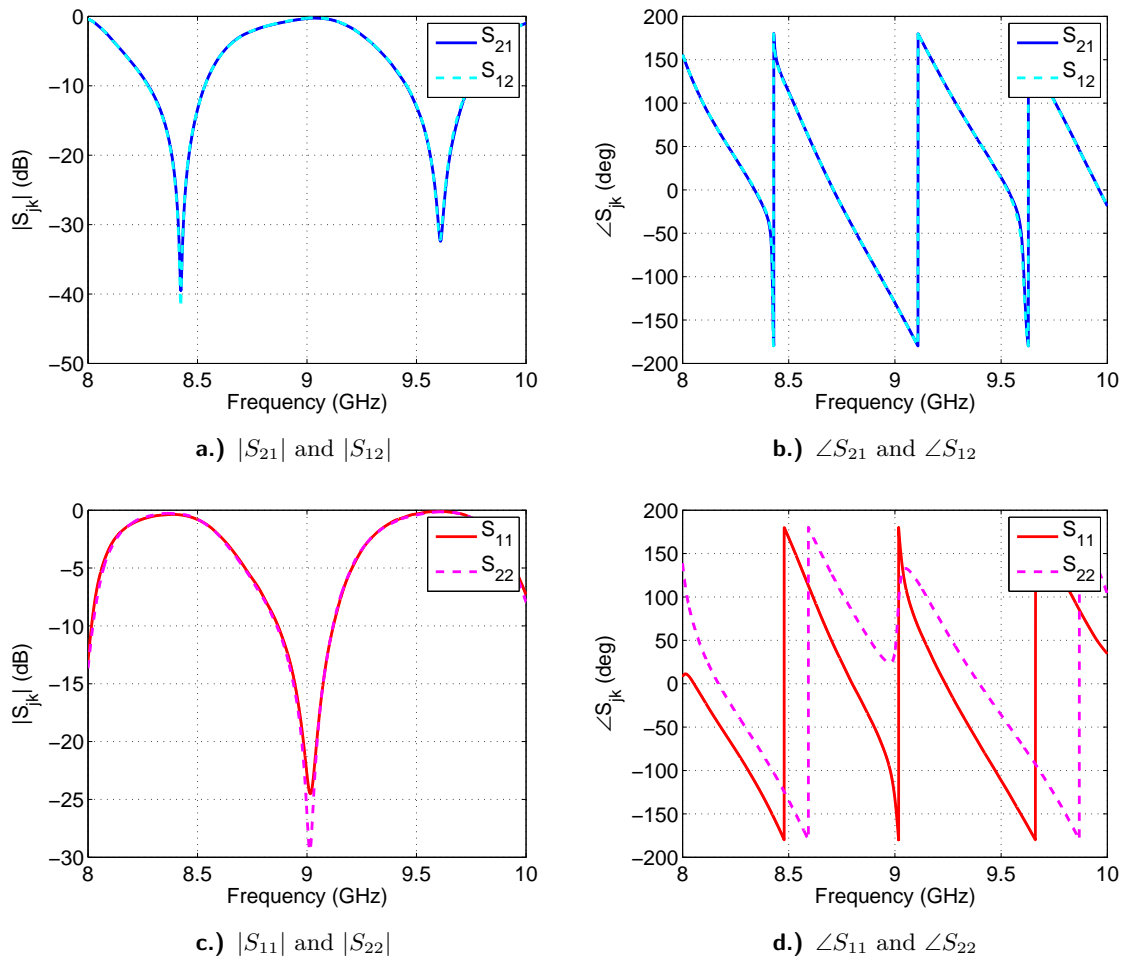
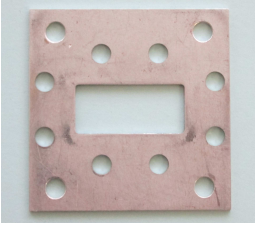

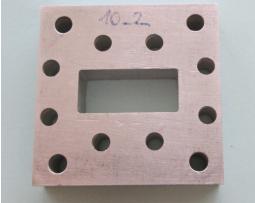
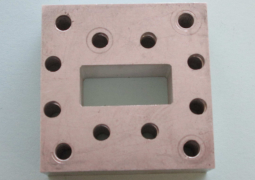


Figure 5.35. Complete S-matrix data for the first data set

	Nominal length (mm)	Actual length (mm)
	1.000	0.890
	2.000	1.910
	5.000	4.880
	10.000	9.990
	15.000	14.980
	50.000	49.920
	100.000	99.990

Tab. 5.7. WR90 segments used for the experimental verification

5.2.1. The results obtained by idealized approach

Prior to using the proposed calibration technique, the data were evaluated using the formula 4.23 which describes general behavior of such interferometer but it does not take into account the parasitic properties of the hardware.

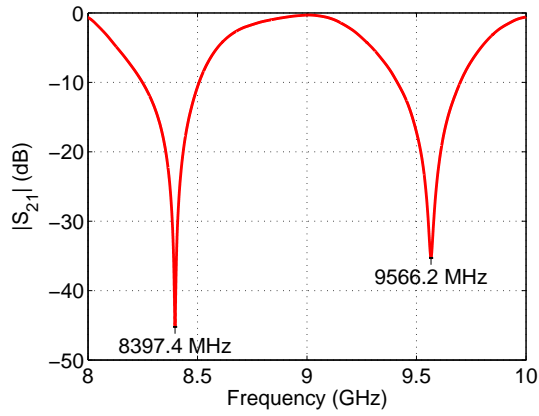
Thanks to the fact that one measurement sweep contains 20000 frequency points, the interpolation effects could be neglected. It means that there is one frequency point per 100 kHz. As shown in the example 4.1.3, in the simulation with the frequency step of 1 MHz and in the similar frequency range, the error caused by the finite frequency step is about several microns. With respect to the uncertainty of the mechanical measurement, the error which can be caused by the finite frequency step is much smaller so it can be neglected.

The all measured traces of the $|S_{21}|$ parameter are shown in the Fig. 5.36. In the each measurement there are two markers on the trace indicating the frequency where the minimum occurs. Based on this information, the results are evaluated and compared in the table 5.8. It is evident, that despite the all advantages of the interferometric system, the effect of the systematic errors is very high and therefore the difference between expected values and evaluated values is in the range of millimeters! The table 5.8 also lists the phase differences in the degrees at the frequency 8.5 GHz. It is clear that these results are worse then worst case for direct VNA measurement.

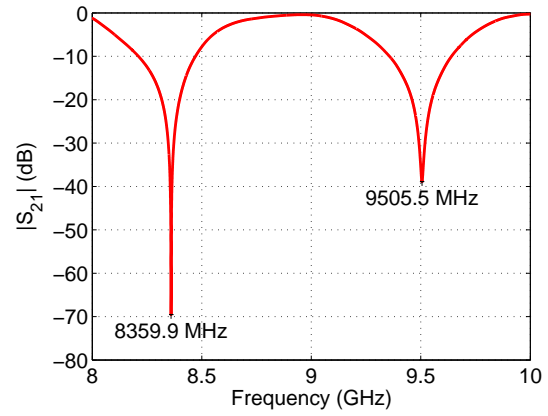
	Expected value (mm)	Evaluated value (mm)	Difference (μm)	Phase error at 8.5 GHz ($^\circ$)
1	100.880	102.160	1280.6	16.63
2	101.900	103.360	1461.5	18.98
3	104.870	106.940	2066.2	26.83
4	109.980	113.010	3033.2	39.39
5	114.980	114.320	-663.06	8.61
6	149.940	151.170	1227.6	15.93
7	99.990	101.320	1325.5	17.21

Tab. 5.8. Evaluated values from the measurement

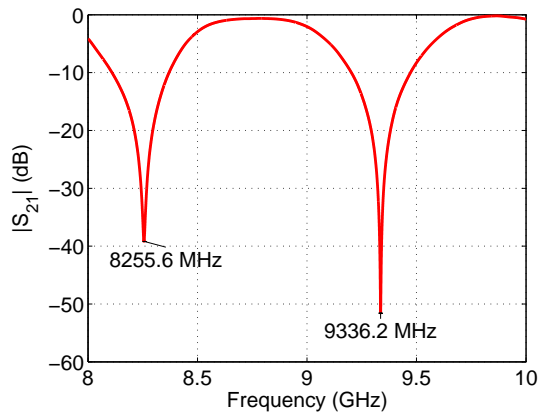
From this real measurement it is evident, that for absolute measurement, the direct use of any interferometer can bring poor results despite the fact, that for relative measurement it can bring superb results and sensitivity [17].



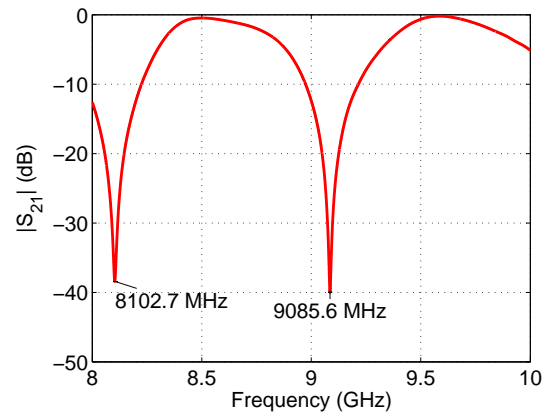
a.) Setup 1. $l_{test} = 100.880$ mm



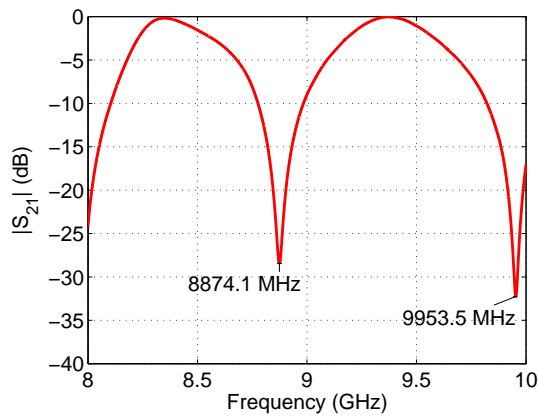
b.) Setup 2. $l_{test} = 101.900$ mm



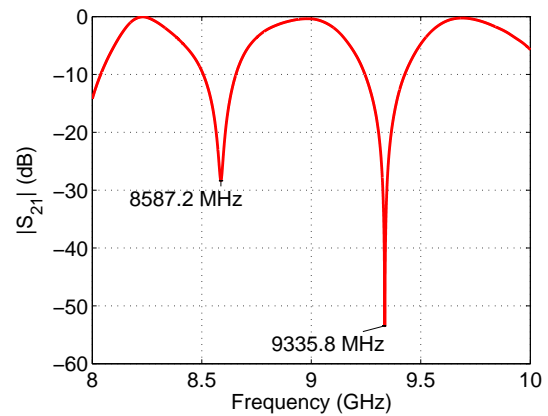
c.) Setup 3. $l_{test} = 104.870$ mm



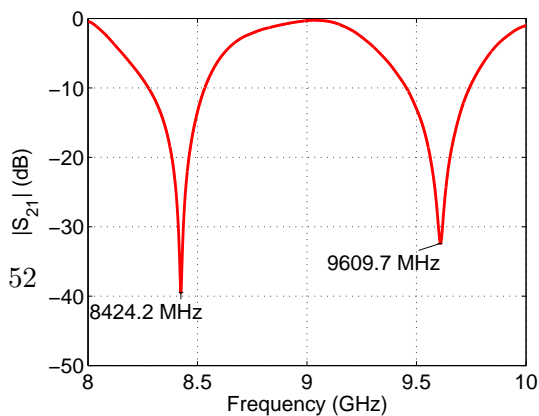
d.) Setup 4. $l_{test} = 109.980$ mm



e.) Setup 5. $l_{test} = 114.980$ mm



f.) Setup 6. $l_{test} = 149.980$ mm



g.) Setup 7. $l_{test} = 99.99$ mm

5.2.2. The results obtained using proposed calibration technique

Once the raw data from the interferometer were measured, they could be evaluated using several different ways. Here will be presented results given by the proposed calibration technique. For the calibration the model was used which includes only the main paths in the interferometer and the most critical parasitic term for S_{21} measurement - the term m_{12} . To simplify the problem, it was assumed that the used hardware is reciprocal. So the S-matrix 5.51 describes the model used for the calibration.

$$S_{\text{model}} = \begin{pmatrix} 0 & m_{12} & m_{13} & m_{14} \\ m_{12} & 0 & m_{23} & m_{24} \\ m_{13} & m_{23} & 0 & 0 \\ m_{14} & m_{24} & 0 & 0 \end{pmatrix} \quad (5.51)$$

Thus, it can be simply written that the model used for the calibration is

$$S_k^{21}(f) = e_1(f) \Gamma_k^{ref}(f) + e_2(f) \Gamma_k^{test}(f) + ec_1(f) \quad (5.52)$$

where e_1 , e_2 and ec_1 are:

$$e_1(f) = m_{14}(f) m_{24}(f) \quad (5.53)$$

$$e_2(f) = m_{13}(f) m_{23}(f) \quad (5.54)$$

and finally the term

$$ec_1(f) = m_{12}(f) \quad (5.55)$$

It was assumed, that the reflection coefficient in the *reference channel* is the same and known during all the measurements

$$\Gamma_k^{ref}(f) = -e^{-2il_k^{ref} \beta^{TE_{10}}(f)} \quad (5.56)$$

where $\beta^{TE_{10}}(f)$ is the phase constant of the TE_{10} mode in the rectangular waveguide.

Contrary to the *reference channel* the reflection in the *test channel* was different for each measurement, because there was a different offset short with the offset of l_k^{test} for each measurement.

$$\Gamma_k^{test}(f) = -e^{-2il_k^{test} \beta^{TE_{10}}(f)} \quad (5.57)$$

Firstly, let's assume that the terms Γ_k^{test} and Γ_k^{ref} are fully known, because they are measured using mechanical caliper. Since the equation 5.52 consists of five frequency dependent terms, so there are three remaining unknown complex terms $e_1(f)$, $e_2(f)$ and $ec_1(f)$. For this case, three different measurements of the S_{21} are sufficient to compute the unknown error terms. In that scenario the calibration result will be solely dependent on agreement between the calibration standards definition values Γ_k^{ref} , Γ_k^{test} and the actual values. In that case, the calibration results would reflect the random error caused by repeatability connection or incorrectly characterized standards.

Now consider, there is data set contains four different S_{21} measurements. Then it is an

overdetermined set of the data and it enables to determine more then the mentioned error terms. Thanks to this all offset lengths l_k^{test} may be considered as unknown.

Since the parameters l_k^{test} are scalar values, only condition for this assumption is that the number of measured frequency points per one sweep have to be greater than number of unknown offsets. Otherwise the data set is not overdetermined.

For the implementation of this technique the MATLAB was used and for the optimization the *lsqnonlin* function was used. The equation 5.52 was given as a root function and all seven data sets were used for the entire calibration process. Weighting coefficient $W_i(f)$ was chosen in the following way.

$$W_k(f) = \begin{cases} 1, & \text{if } |S_k^{21}(f)| < -10 \text{ dB.} \\ 0.5, & \text{otherwise.} \end{cases} \quad (5.58)$$

This decision was based on the parameters of VNA ZVA67 discussed in the chapter 3, but the values of the weighting coefficient (1 and 0.5) were selected ad-hoc.

	Expected value (mm)	Obtained from the calibration (mm)	Difference (μm)	Phase error on 8.5GHz ($^\circ$)
1	100.880	100.830	46.049	0.5981
2	101.900	101.880	17.852	0.2319
3	104.870	104.960	87.726	1.1395
4	109.980	109.980	3.4033	0.0442
5	114.980	114.910	72.426	0.9408
6	149.940	150.090	145.110	1.8848
7	99.990	100.100	112.290	1.4585

Tab. 5.9. The results given using the proposed calibration technique 20000 points.

The results of the optimization are in the table 5.9. The table lists the lengths of the offset shorts obtained from the calibration. These values are compared with the expected values, which were measured using mechanical caliper. And the difference is listed in the length units as well as in degrees at the frequency 8.5 GHz. It is evident that these results are definitely better in comparison with direct VNA measurement. The measured and fitted traces of $|S_{21}|$ are in figures 5.37, 5.37, 5.37 as well as the residual least square error of measurement and fit. From these differences is evident that the best fit is close to the minima and conversely the worst fit is at the frequencies where values of $|S_{21}|$ are highest, which is in the accordance with weighting criterion 5.58.

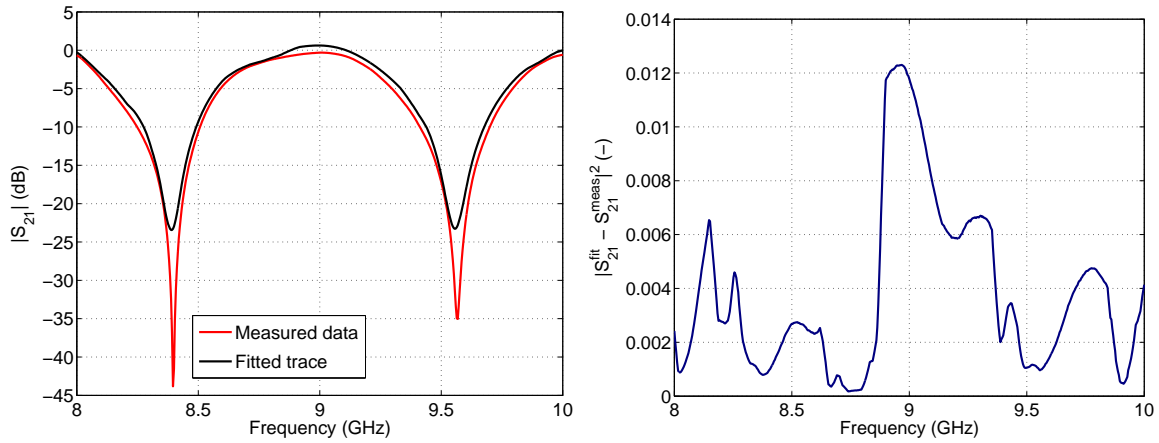
In the Fig. 5.40, there are resulting error terms of the interferometer. They are compared with the values of the identical interferometer (a WR90 180° hybrid coupler) which were obtained by the direct four-port measurement using VNA. The all measured parameters of this hybrid coupler are in the appendix A.2. From the results it is evident that the phases of the error terms are fitted very well, but there are quite a high discrepancy in the magnitudes. However, the term m_{12} is in good agreement with the direct measurement. This reflects the fact, that the term m_{12} has a significant impact on the S_{21} measurement.

Finally, for the use with the proposed calibration technique the data sets containing 20000 frequency points, were reduced without interpolation to the data sets containing 500 data points per one measurement sweep. It was because the seven data sets containing 20000 points

	Expected value (mm)	Obtained from the calibration (mm)	Difference (μm)	Phase error on 8.5GHz ($^\circ$)
1	100.880	100.880	4.4887	0.0583
2	101.90	101.930	29.407	0.3819
3	104.870	105.010	137.78	1.7897
4	109.980	110.040	60.732	0.7889
5	114.980	114.960	21.141	0.2746
6	149.940	150.130	188.05	2.4427
7	99.990	100.140	151.32	1.9656

Tab. 5.10. The results given using the proposed calibration technique 500 points

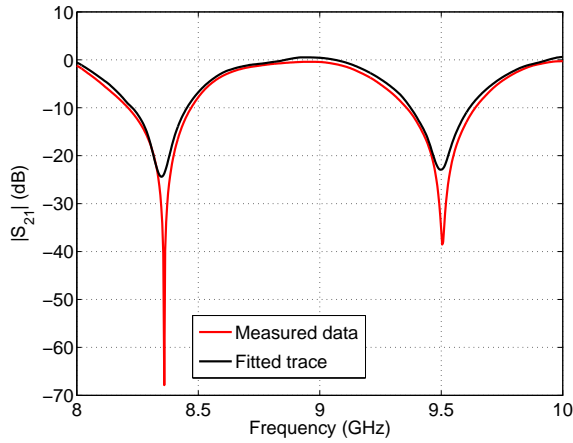
each, are slightly huge and thus optimization procedure spend very long time. Moreover, on the following results is apparent how well this technique can deal with repeatedly mentioned problem of the finite frequency step size. In the data set containing 500 frequency points, the frequency step size is 20 MHz. Despite very coarse frequency step size, the results 5.10 given using this calibration technique are very well.



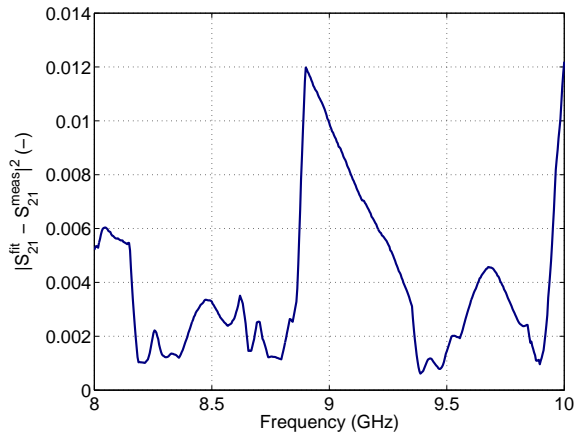
a.) Setup 1. $l_{test} = 100.880$ mm, measured and fitted trace obtained from the calibration

b.) Setup 1. Least square error

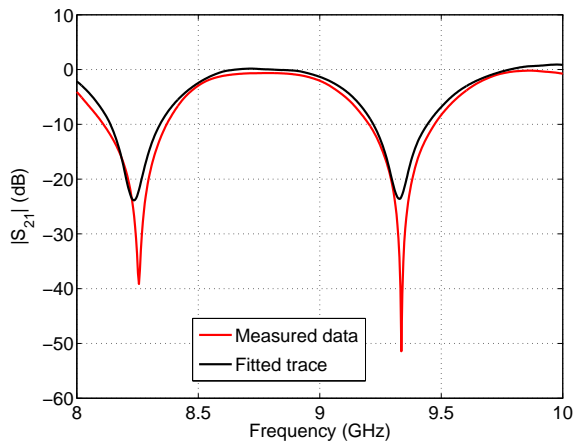
Figure 5.37. Measured $|S_{21}|$ and fitted trace obtained from the calibration and corresponding least square error.



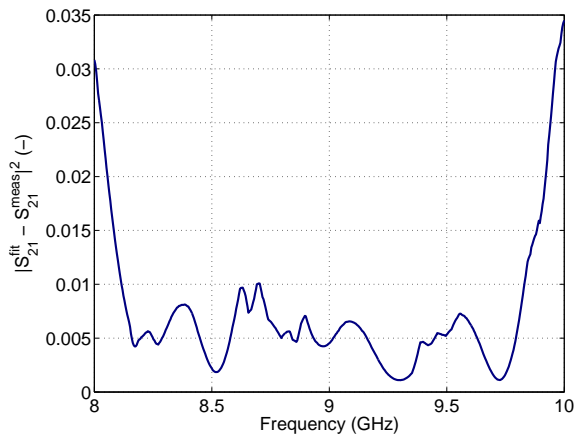
a.) Setup 2. $l_{test} = 101.900$ mm, measured and fitted trace obtained from the calibration



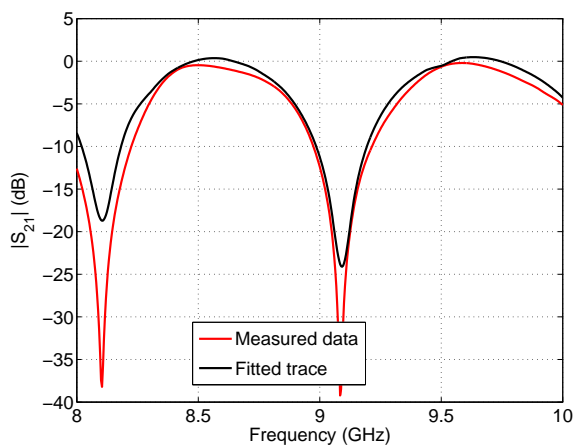
b.) Setup 2. Least square error



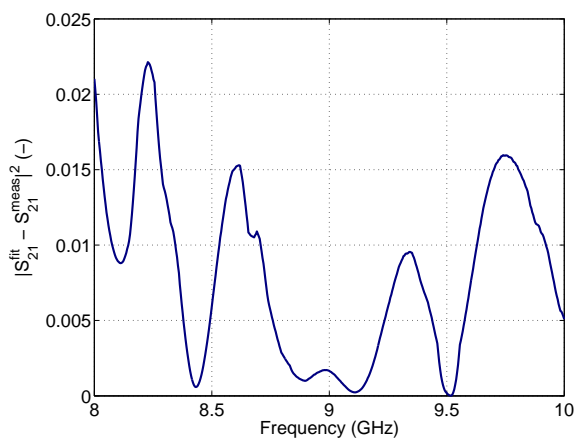
c.) Setup 3. $l_{test} = 104.870$ mm, measured and fitted trace obtained from the calibration



d.) Setup 3. Least square error

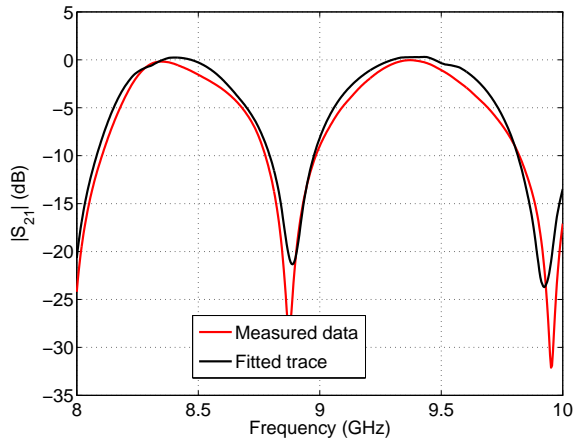


e.) Setup 4. $l_{test} = 109.980$ mm, measured and fitted trace obtained from the calibration

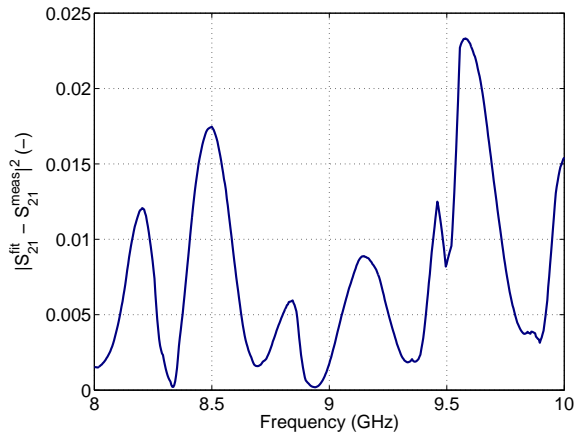


f.) Setup 4. Least square error

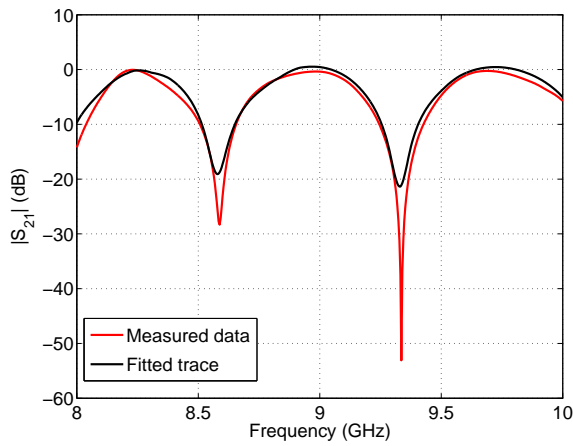
Figure 5.38. Measured $|S_{21}|$ and fitted trace obtained from the calibration and corresponding least square error.



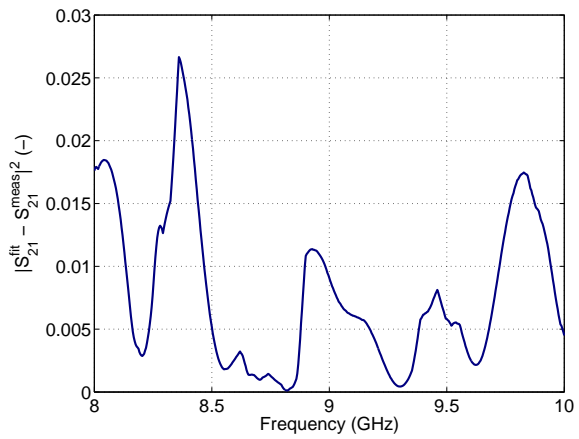
a.) Setup 5. $l_{test} = 114.980$ mm, measured and fitted trace obtained from the calibration



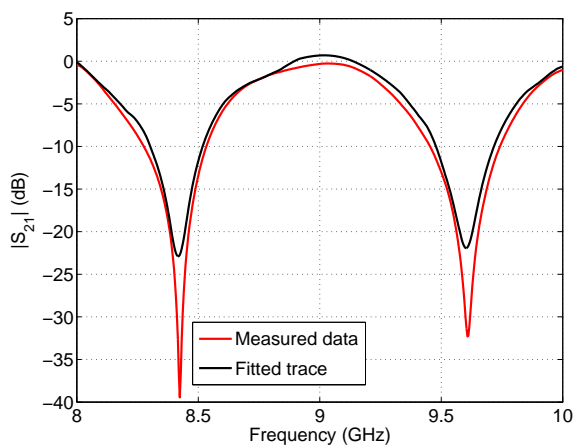
b.) Setup 5. Least square error



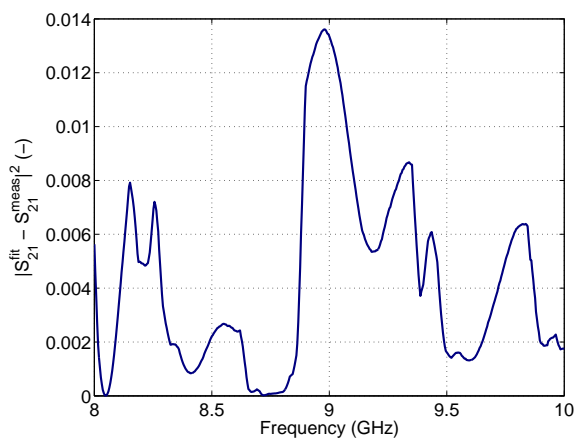
c.) Setup 6. $l_{test} = 149.980$ mm, measured and fitted trace obtained from the calibration



d.) Setup 6. Least square error

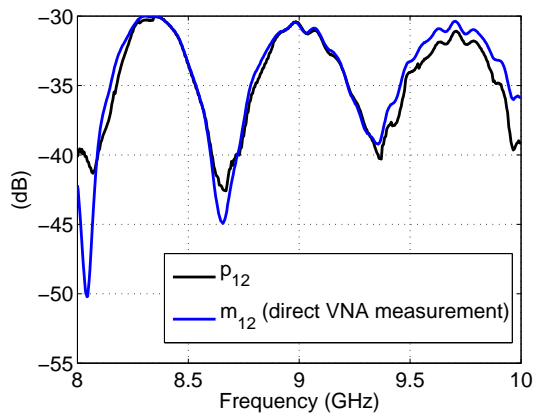


e.) Setup 7. $l_{test} = 99.99$ mm, measured and fitted trace obtained from the calibration

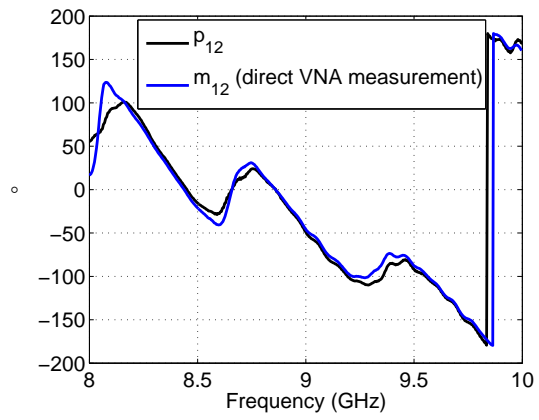


f.) Setup 7. Least square error

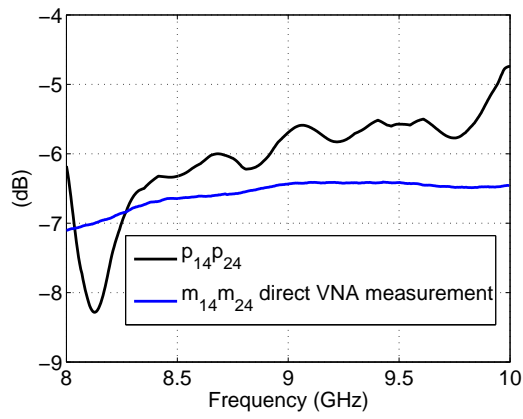
Figure 5.39. Measured $|S_{21}|$ and fitted trace obtained from the calibration and corresponding least square error.



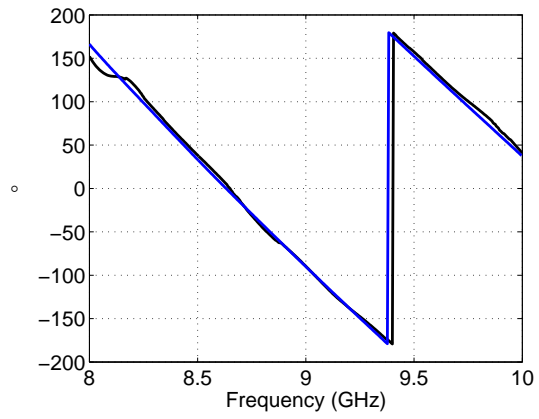
a.) $|m_{12}|$



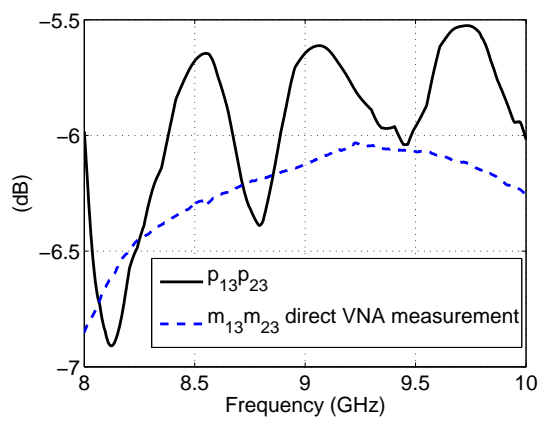
b.) $\angle m_{12}$



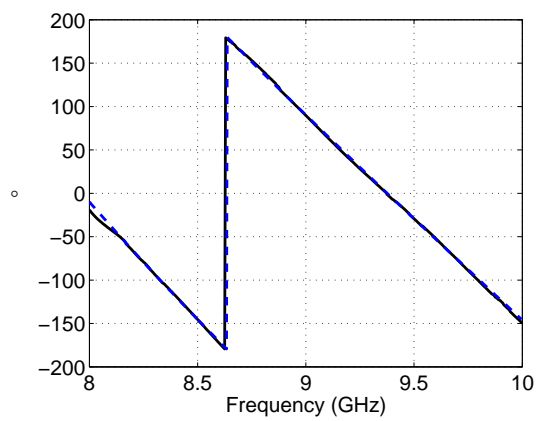
c.) $|m_{14}m_{24}|$



d.) $\angle m_{14}m_{24}$



e.) $|m_{13}m_{23}|$



f.) $\angle m_{13}m_{23}$

Figure 5.40. Error terms of the interferometer. Values obtained from the direct measurement on the VNA versus values returned from calibration technique

5.2.3. Summary

In this chapter the new calibration technique was presented. This calibration technique were designed especially for the usage with microwave interferometer. It was shown, that it is not possible to use the interferometer for the absolute phase measurement without this calibration technique. The results in 5.2.1 clearly prove that.

In the section 5.2.2 was shown how the proposed calibration technique can increase the precision for the absolute phase measurement. From the table 5.9 it is evident, that in the worst case the deviation was $\approx 1.8^\circ$ and average deviation is less then 1° .

Although the magnitudes of the error terms of the interferometer were evaluated with quite high discrepancy (Fig. 5.40), the phases of mentioned terms obtained from the calibration process are in good agreement with the values measured directly on the VNA. This is in the accordance with the fact, that the phases of the error terms play significant role for the precise phase measurement of the reflection coefficients in the *reference* and *test channel*, while the magnitudes not. The discrepancies in the magnitudes are due to the use of the simplified model, which was used as a root function for the optimizer. This model does not contain reflections as well as cross-talks m_{34} , m_{43} , but the measured data contain the influence of these terms. So it is clear, that the mentioned discrepancies in the magnitudes reflect the effects of these omitted terms. It is evident that for the precise evaluation of the error model of the interferometer, the more complex model as a root function should be used.

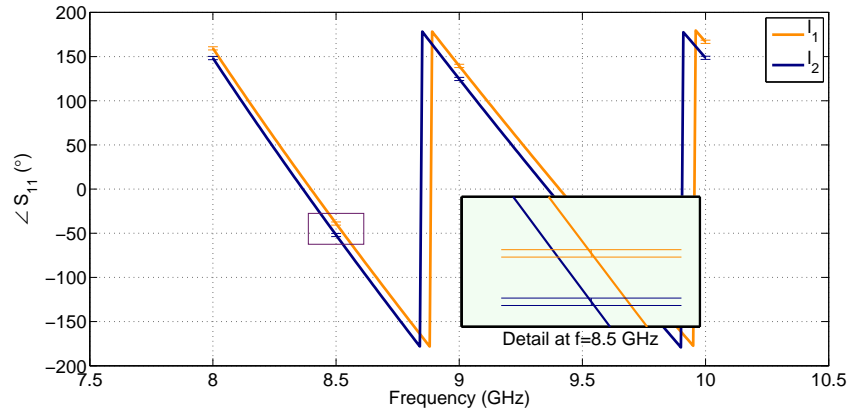


Figure 5.41. Resulting phase diagrams for the WR90 offset short 100 mm and 101 mm

Finally, in the Fig 5.41, there are depicted two traces of the phase of the reflection coefficient for two measured sort-circuited WR90 segments. Uncertainty regions are also in this figure. The worst case of deviation was used as a uncertainty value. From this figure it is clear, that interferometry technique with the proposed calibration technique enables the precise measurement of the phase of the reflection coefficient.

6. Conclusion

This thesis introduced the principle of microwave interferometric measurement focused on the measurement of the phase of the reflection coefficient. Starting with the uncertainty analysis it was demonstrated that this approach can decrease the measurement uncertainty in comparison with the direct VNA measurement.

Furthermore, it was shown which errors arise during this measurement and how they can affect the results. Thanks to this analysis, it was possible to design new calibration procedure, which is designed especially for the usage with such a system. Besides this, the knowledge about the systematic errors should be taken into account during the design of such a system and experiment aimed to reach better results.

The proposed calibration technique is the most important piece of this thesis. This technique solves a number of serious problems simultaneously. From the most serious issue, it solves effects of the systematic errors which are caused by the non-ideal hardware. The calibration technique does not require the precise knowledge about the parameters of the calibration standards since they are described by the proper frequency dependent model. The actual parameters of the standards are given by the calibration technique itself. Finally it solves the problem of the finite frequency step-size. Besides this, the calibration technique also solves the problem of the absolute measurement, because it returns the optimized parameters of calibration standards.

While in the case of direct measurement using VNA the worst case of the uncertainty of the phase measurement is about 3° , the worst deviation given by this calibration technique was about 1.8° , which is roughly two times better. But the average deviation over all the data was $\approx 1^\circ$. Moreover, these results were given using the incomplete model for the calibration and some of the parasitic properties were neglected. It might be supposed that including additional parasitic properties to the model, the deviation should be smaller. The importance of the calibration technique can be illustrated on the experimental results evaluated using the idealized approach. Despite the fact, that entire interferometry approach should improve the properties of the VNA, the results obtained using idealized approach are very poor even worst that can be expected from the direct VNA measurement.

Thus it can be concluded, that the interferometry technique improves the properties of the VNA in term of the precise measurement of the phase, but for the real interferometric systems including parasitic properties, the system must be calibrated to overcome the systematic errors.

6.1. Additional remarks and the future work

It was shown that the proposed calibration technique can improve the precision of the phase measurement using an interferometer, however there are still several problems should be solved in the future. Like in the case of one-port VNA offset-short calibration or calibration using TRL or Multiline TRL, it is necessary to take into account the optimal lengths of the offsets or lines. It is clear, that proper selection can increase the bandwidth as well as precision. For the experimental verification which has been presented in this thesis, the lengths of the offset shorts were selected ad-hoc. The next important step should be more sophisticated verification. The lengths of the offset shorts obtained from the calibration were compared with the lengths obtained from the mechanical measurement using a caliper, but uncertainty of the mechanical measurement was neglected. So it should be taken into account in the future.

6.2. Authored and co-authored results dealing with the topic of the dissertation

- **M. Prihoda** and K. Hoffmann, "Self-calibrating evaluation method for microwave interferometry measurements," in *Electronics Letters*, vol. 49, no. 5, pp. 356-358, February 28 2013.
doi: 10.1049/el.2012.3122
URL: <http://ieeexplore.ieee.org/stamp/stamp.jsp?tp=&arnumber=6473956&isnumber=6473925>
- K. Hoffmann, Z. Skvor and **M. Prihoda**, "Precise microwave measurement of liquid level," *Microwave Measurement Conference (ARFTG)*, 2012 79th ARFTG, Montreal, QC, 2012, pp. 1-2.
doi: 10.1109/ARFTG79.2012.6291194
URL: <http://ieeexplore.ieee.org/stamp/stamp.jsp?tp=&arnumber=6291194&isnumber=6291173>

6.3. Other authored or co-authored and published results

- **M. Prihoda** and K. Hoffmann, "Novel Multimode Planar Absorbing Structure," in *IEEE Microwave and Wireless Components Letters*, vol. 23, no. 1, pp. 7-9, Jan. 2013.
doi: 10.1109/LMWC.2012.2234093
URL: <http://ieeexplore.ieee.org/stamp/stamp.jsp?tp=&arnumber=6392225&isnumber=6409984>
- **M. Příhoda** and K. Hoffmann, "New multimode planar structure," *Microwave Measurement Symposium (ARFTG)*, 2011 78th ARFTG, Tempe, AZ, 2011, pp. 1-4.
doi: 10.1109/ARFTG78.2011.6183884
URL: <http://ieeexplore.ieee.org/stamp/stamp.jsp?tp=&arnumber=6183884&isnumber=6183857>
- **M. Příhoda**, O. Morávek and K. Hoffmann, "Study of absorber materials usable on microstrip and their attribute improvements," *Radioelektronika (RADIOELEKTRONIKA)*, 2011 21st International Conference, Brno, 2011, pp. 1-3.
doi: 10.1109/RADIOELEK.2011.5936448

URL: <http://ieeexplore.ieee.org/stamp/stamp.jsp?tp=&arnumber=5936448&isnumber=5936384>

- O. Moravek, **M. Prihoda** and K. Hoffmann, "Verification technique of on-planar VNA calibration," Radioelektronika (RADIOELEKTRONIKA), 2012 22nd International Conference, Brno, 2012, pp. 1-4.
URL: <http://ieeexplore.ieee.org/stamp/stamp.jsp?tp=&arnumber=6207654&isnumber=6207636>
- P. Valtr, P. Pechac, T. Korinek, O. Moravek and **M. Prihoda**, "Measurement of window blind attenuation at 5–50 GHz," Antennas and Propagation (EuCAP), 2013 7th European Conference on, Gothenburg, 2013, pp. 3790-3793.
URL: <http://ieeexplore.ieee.org/stamp/stamp.jsp?tp=&arnumber=6547019&isnumber=6546197>

Bibliography

- [1] M. Hiebel. *Fundamentals of Vector Network Analysis*. Rohde & Schwarz, 2007. ISBN: 9783939837060. URL: <https://books.google.cz/books?id=jYG2PQAACAAJ>.
- [2] J. C. Booth et al. “Quantitative Permittivity Measurements of Nanoliter Liquid Volumes in Microfluidic Channels to 40 GHz”. In: *IEEE Transactions on Instrumentation and Measurement* 59.12 (Dec. 2010), pp. 3279–3288. ISSN: 0018-9456.
- [3] J. Roelvink, S. Trabelsi, and S. O. Nelson. “A Planar Transmission-Line Sensor for Measuring the Microwave Permittivity of Liquid and Semisolid Biological Materials”. In: *IEEE Transactions on Instrumentation and Measurement* 62.11 (Nov. 2013), pp. 2974–2982. ISSN: 0018-9456.
- [4] P. F. X. Neumaier et al. “Application of multivariate analysis to gas-phase spectroscopy at 245 GHz”. In: *Infrared, Millimeter, and Terahertz waves (IRMMW-THz), 2014 39th International Conference on*. Sept. 2014, pp. 1–2.
- [5] S. Fabiani et al. “Broadband Scanning Microwave Microscopy investigation of graphene”. In: *Microwave Symposium Digest (MTT), 2011 IEEE MTT-S International*. June 2011, pp. 1–4.
- [6] S. Gu et al. “Setting Parameters Influence on Accuracy and Stability of Near-Field Scanning Microwave Microscopy Platform”. In: *IEEE Transactions on Instrumentation and Measurement* 65.4 (Apr. 2016), pp. 890–897. ISSN: 0018-9456.
- [7] H. Bakli, K. Haddadi, and T. Lasri. “Interferometric Technique for Scanning Near-Field Microwave Microscopy Applications”. In: *Instrumentation and Measurement, IEEE Transactions on* 63.5 (May 2014), pp. 1281–1286. ISSN: 0018-9456.
- [8] S. Gu et al. “Measurement accuracy and repeatability in near-field scanning microwave microscopy”. In: *Instrumentation and Measurement Technology Conference (I2MTC), 2015 IEEE International*. May 2015, pp. 1735–1740.
- [9] A. Imtiaz, T. M. Wallis, and P. Kabos. “Near-Field Scanning Microwave Microscopy: An Emerging Research Tool for Nanoscale Metrology”. In: *IEEE Microwave Magazine* 15.1 (Jan. 2014), pp. 52–64. ISSN: 1527-3342.
- [10] H. Happy et al. “Measurement Techniques for RF Nanoelectronic Devices: New Equipment to Overcome the Problems of Impedance and Scale Mismatch”. In: *Microwave Magazine, IEEE* 15.1 (Jan. 2014), pp. 30–39. ISSN: 1527-3342.
- [11] M. Randus and K. Hoffmann. “A simple method for extreme impedances measurement - experimental testing”. In: *Microwave Measurement Symposium, 2008 72nd ARFTG*. Dec. 2008, pp. 40–44.
- [12] M. Randus and K. Hoffmann. “A Method for Direct Impedance Measurement in Microwave and Millimeter-Wave Bands”. In: *Microwave Theory and Techniques, IEEE Transactions on* 59.8 (Aug. 2011), pp. 2123–2130. ISSN: 0018-9480.

- [13] K. Haddadi and T. Lasri. “Interferometric technique for microwave measurement of high impedances”. In: *Microwave Symposium Digest (MTT), 2012 IEEE MTT-S International*. June 2012, pp. 1–3.
- [14] K. Haddadi and T. Lasri. “Three-paths microwave interferometric system based on a six-port technique”. In: *Radar Conference (EuRAD), 2013 European*. Oct. 2013, pp. 291–294.
- [15] S. Gu et al. “Near-field scanning microwave microscope for subsurface non-destructive characterization”. In: *Microwave Conference (EuMC), 2015 European*. Sept. 2015, pp. 155–158.
- [16] K. Haddadi and T. Lasri. “Interferometer-Based Microwave Microscopy Operating in Transmission Mode”. In: *IEEE Sensors Journal* 14.7 (July 2014), pp. 2226–2227. ISSN: 1530-437X.
- [17] K. Hoffmann and Z. Skvor. “Contactless distance measurement method”. In: *Microwave Measurement Conference (ARFTG), 2011 77th ARFTG*. June 2011, pp. 1–4.
- [18] K. Hoffmann, Z. Skvor, and M. Prihoda. “Precise microwave measurement of liquid level”. In: *Microwave Measurement Conference (ARFTG), 2012 79th ARFTG*. June 2012, pp. 1–2.
- [19] K. Hoffmann and Z. Skvor. “Microwave interferometric method for metal sheet thickness measurement”. In: *Microwave Measurement Conference (ARFTG), 2013 81st ARFTG*. June 2013, pp. 1–3.
- [20] K. Will and A. Omar. “Phase Measurement of RF Devices Using Phase-Shifting Interferometry”. In: *Microwave Theory and Techniques, IEEE Transactions on* 56.11 (Nov. 2008), pp. 2642–2647. ISSN: 0018-9480.
- [21] Martin Randus. “Methods for measurement of extreme impedances”. Doctoral Thesis. Czech Technical University in Prague, May 2012.
- [22] M. Haase and K. Hoffmann. “Study of calibration standards for extreme impedances measurement”. In: *Microwave Measurement Conference (ARFTG), 2014 83rd ARFTG*. June 2014, pp. 1–6.
- [23] M. Haase and K. Hoffmann. “Calibration/verification standards for measurement of extremely high impedances”. In: *Microwave Measurement Conference, 2015 86th ARFTG*. Dec. 2015, pp. 1–4.
- [24] *Scanning Microwave Microscopy (SMM) Modei - Highly Sensitive Imaging Mode for Complex, Calibrated Electrical and Spatial Measurements*. Agilent Technologies, 2014. URL: <http://cp.literature.agilent.com/litweb/pdf/5989-8817EN.pdf>.
- [25] A. Schicht et al. “Absolute Phase-Based Distance Measurement for Industrial Monitoring Systems”. In: *IEEE Sensors Journal* 9.9 (Sept. 2009), pp. 1007–1013. ISSN: 1530-437X.
- [26] G.S. Woods, D.L. Maskell, and M.V. Mahoney. “A high accuracy microwave ranging system for industrial applications”. In: *Instrumentation and Measurement, IEEE Transactions on* 42.4 (Aug. 1993), pp. 812–816. ISSN: 0018-9456.
- [27] A. Stelzer et al. “A microwave position sensor with submillimeter accuracy”. In: *IEEE Transactions on Microwave Theory and Techniques* 47.12 (Dec. 1999), pp. 2621–2624. ISSN: 0018-9480.

- [28] B.D. Hall. “Notes on complex measurement uncertainty—part 1”. In: *MSL, Lower Hutt, New Zealand, Tech. Rep* 2483 (2010).
- [29] B. D. Hall. “Notes on complex measurement uncertainty—part 2”. In: *MSL, Lower Hutt, New Zealand, Tech. Rep* 2557 (2010).
- [30] B. D. Hall. “Using uncertain complex numbers with VNA measurements”. In: *ARFTG Microwave Measurement Conference, 2008 71st*. June 2008, pp. 1–3.
- [31] N. M. Ridler and M. J. Salter. “Propagating S-parameter uncertainties to other measurement quantities”. In: *ARFTG Conference Digest-Fall, 58th*. Vol. 40. Nov. 2001, pp. 1–19.
- [32] M. Garelli and A. Ferrero. “A Unified Theory for S-Parameter Uncertainty Evaluation”. In: *IEEE Transactions on Microwave Theory and Techniques* 60.12 (Dec. 2012), pp. 3844–3855. ISSN: 0018-9480.
- [33] *R&S®ZVA Vector Network Analyzer Specifications*. Rohde & Schwarz. URL: http://www2.rohde-schwarz.com/file%5C_18299/ZVA%5C_dat-sw%5C_en.pdf.
- [34] *N5247A PNA-X Microwave Network Analyzer, 67 GHz*. Keysight. URL: <http://literature.cdn.keysight.com/litweb/pdf/N5247-90002.pdf>.
- [35] *N5227A PNA Microwave Network Analyzer, 67 GHz*. Keysight. URL: <http://literature.cdn.keysight.com/litweb/pdf/N5227-90002.pdf>.
- [36] Stig Rehnmark. “On the Calibration Process of Automatic Network Analyzer Systems (Short Papers)”. In: *Microwave Theory and Techniques, IEEE Transactions on* 22.4 (Apr. 1974), pp. 457–458. ISSN: 0018-9480.
- [37] W. Kruppa and K. F. Sodomsky. “An Explicit Solution for the Scattering Parameters of a Linear Two-Port Measured with an Imperfect Test Set (Correspondence)”. In: *IEEE Transactions on Microwave Theory and Techniques* 19.1 (Jan. 1971), pp. 122–123. ISSN: 0018-9480.
- [38] A. Ferrero and U. Pisani. “QSOLT: A New Fast Calibration Algorithm for Two Port S Parameter Measurements”. In: *ARFTG Conference Digest-Winter, 38th*. Vol. 20. Dec. 1991, pp. 15–24.
- [39] U. Stumper. “Influence of TMSO calibration standards uncertainties on VNA S-parameter measurements”. In: *IEEE Transactions on Instrumentation and Measurement* 52.2 (Apr. 2003), pp. 311–315. ISSN: 0018-9456.
- [40] U. Stumper and T. Schrader. “Influence of Different Configurations of Nonideal Calibration Standards on Vector Network Analyzer Performance”. In: *IEEE Transactions on Instrumentation and Measurement* 61.7 (July 2012), pp. 2034–2041. ISSN: 0018-9456.
- [41] Glenn F. Engen and Cletus A. Hoer. “Thru-Reflect-Line: An Improved Technique for Calibrating the Dual Six-Port Automatic Network Analyzer”. In: *Microwave Theory and Techniques, IEEE Transactions on* 27.12 (Dec. 1979), pp. 987–993. ISSN: 0018-9480.
- [42] A. Ferrero and U. Pisani. “Two-port network analyzer calibration using an unknown ‘thru’”. In: *Microwave and Guided Wave Letters, IEEE* 2.12 (Dec. 1992), pp. 505–507. ISSN: 1051-8207.
- [43] K. J. Silvonen. “A general approach to network analyzer calibration”. In: *IEEE Transactions on Microwave Theory and Techniques* 40.4 (Apr. 1992), pp. 754–759. ISSN: 0018-9480.

- [44] U. Stumper. “Influence of Non-Ideal TRL Calibration Items on VNA S-Parameter Measurements”. In: *Precision Electromagnetic Measurements Digest, 2004 Conference on*. June 2004, pp. 109–110.
- [45] U. Stumper. “Influence of Nonideal Calibration Items on S-Parameter Uncertainties Applying the SOLR Calibration Method”. In: *IEEE Transactions on Instrumentation and Measurement* 58.4 (Apr. 2009), pp. 1158–1163. ISSN: 0018-9456.
- [46] Roger B. Marks. “A multiline method of network analyzer calibration”. In: *Microwave Theory and Techniques, IEEE Transactions on* 39.7 (July 1991), pp. 1205–1215. ISSN: 0018-9480.
- [47] D. C. DeGroot, J. A. Jargon, and R. B. Marks. “Multiline TRL revealed”. In: *ARFTG Conference Digest, Fall 2002. 60th*. Dec. 2002, pp. 131–155.

Appendix A.

Appendix

A.1. 16-term model of an four port interferometer

$$S_{\text{model}} = \begin{pmatrix} m_{11} & m_{12} & m_{13} & m_{14} \\ m_{21} & m_{22} & m_{23} & m_{24} \\ m_{31} & m_{13} & m_{33} & m_{34} \\ m_{41} & m_{23} & m_{43} & m_{44} \end{pmatrix}$$

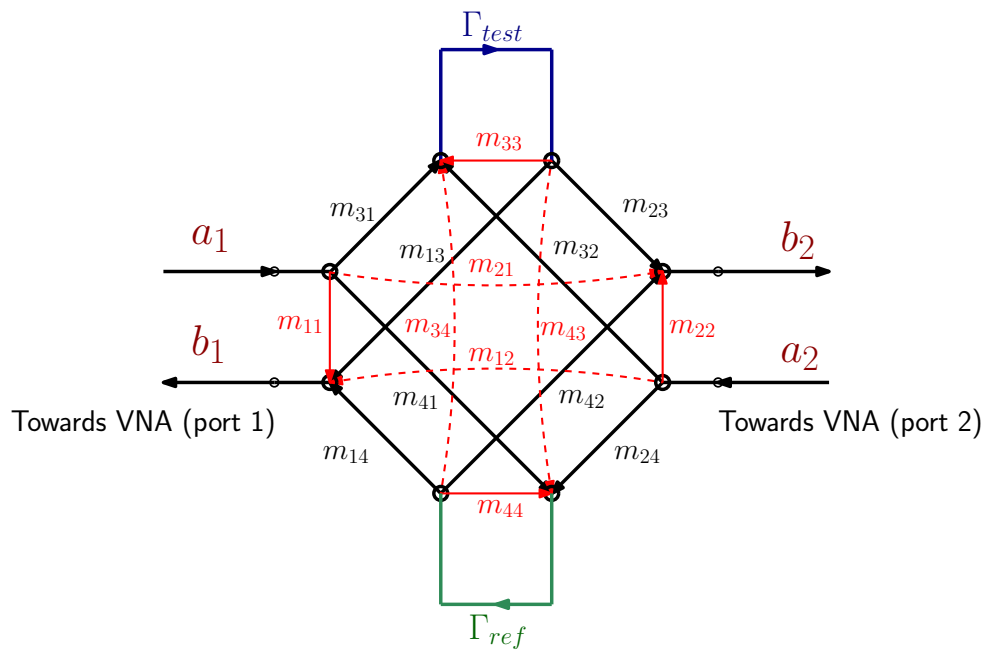


Figure A.42. Flow graph for the full 16-term model of the interferometer

$$\begin{aligned}
S_{11} = & -\frac{m_{11} - \Gamma_{test}m_{11}m_{33} + \Gamma_{test}m_{13}m_{31}}{\Gamma_{test}m_{33} + \Gamma_{ref}m_{44} - \Gamma_{ref}\Gamma_{test}m_{33}m_{44} + \Gamma_{ref}\Gamma_{test}m_{34}m_{43} - 1} \\
& + \frac{-\Gamma_{ref}m_{11}m_{44} + \Gamma_{ref}m_{14}m_{41} + \Gamma_{ref}\Gamma_{test}m_{11}m_{33}m_{44}}{\Gamma_{test}m_{33} + \Gamma_{ref}m_{44} - \Gamma_{ref}\Gamma_{test}m_{33}m_{44} + \Gamma_{ref}\Gamma_{test}m_{34}m_{43} - 1} \\
& + \frac{-\Gamma_{ref}\Gamma_{test}m_{11}m_{34}m_{43} - \Gamma_{ref}\Gamma_{test}m_{13}m_{31}m_{44}}{\Gamma_{test}m_{33} + \Gamma_{ref}m_{44} - \Gamma_{ref}\Gamma_{test}m_{33}m_{44} + \Gamma_{ref}\Gamma_{test}m_{34}m_{43} - 1} \\
& + \frac{\Gamma_{ref}\Gamma_{test}m_{13}m_{34}m_{41} + \Gamma_{ref}\Gamma_{test}m_{14}m_{31}m_{43}}{\Gamma_{test}m_{33} + \Gamma_{ref}m_{44} - \Gamma_{ref}\Gamma_{test}m_{33}m_{44} + \Gamma_{ref}\Gamma_{test}m_{34}m_{43} - 1} \\
& + \frac{-\Gamma_{ref}\Gamma_{test}m_{14}m_{33}m_{41}}{\Gamma_{test}m_{33} + \Gamma_{ref}m_{44} - \Gamma_{ref}\Gamma_{test}m_{33}m_{44} + \Gamma_{ref}\Gamma_{test}m_{34}m_{43} - 1}
\end{aligned} \tag{A.59}$$

$$\begin{aligned}
S_{21} = & -\frac{m_{21} - \Gamma_{test}m_{21}m_{33} + \Gamma_{test}m_{23}m_{31} - \Gamma_{ref}m_{21}m_{44} + \Gamma_{ref}m_{24}m_{41}}{\Gamma_{test}m_{33} + \Gamma_{ref}m_{44} - \Gamma_{ref}\Gamma_{test}m_{33}m_{44} + \Gamma_{ref}\Gamma_{test}m_{34}m_{43} - 1} \\
& + \frac{\Gamma_{ref}\Gamma_{test}m_{21}m_{33}m_{44} - \Gamma_{ref}\Gamma_{test}m_{21}m_{34}m_{43}}{\Gamma_{test}m_{33} + \Gamma_{ref}m_{44} - \Gamma_{ref}\Gamma_{test}m_{33}m_{44} + \Gamma_{ref}\Gamma_{test}m_{34}m_{43} - 1} \\
& + \frac{-\Gamma_{ref}\Gamma_{test}m_{23}m_{31}m_{44} + \Gamma_{ref}\Gamma_{test}m_{23}m_{34}m_{41}}{\Gamma_{test}m_{33} + \Gamma_{ref}m_{44} - \Gamma_{ref}\Gamma_{test}m_{33}m_{44} + \Gamma_{ref}\Gamma_{test}m_{34}m_{43} - 1} \\
& + \frac{\Gamma_{ref}\Gamma_{test}m_{24}m_{31}m_{43} - \Gamma_{ref}\Gamma_{test}m_{24}m_{33}m_{41}}{\Gamma_{test}m_{33} + \Gamma_{ref}m_{44} - \Gamma_{ref}\Gamma_{test}m_{33}m_{44} + \Gamma_{ref}\Gamma_{test}m_{34}m_{43} - 1}
\end{aligned} \tag{A.60}$$

$$\begin{aligned}
S_{12} = & -\frac{m_{12} - \Gamma_{test}m_{12}m_{33} + \Gamma_{test}m_{13}m_{32} - \Gamma_{ref}m_{12}m_{44}}{\Gamma_{test}m_{33} + \Gamma_{ref}m_{44} - \Gamma_{ref}\Gamma_{test}m_{33}m_{44} + \Gamma_{ref}\Gamma_{test}m_{34}m_{43} - 1} \\
& + \frac{\Gamma_{ref}m_{14}m_{42} + \Gamma_{ref}\Gamma_{test}m_{12}m_{33}m_{44} - \Gamma_{ref}\Gamma_{test}m_{12}m_{34}m_{43}}{\Gamma_{test}m_{33} + \Gamma_{ref}m_{44} - \Gamma_{ref}\Gamma_{test}m_{33}m_{44} + \Gamma_{ref}\Gamma_{test}m_{34}m_{43} - 1} \\
& + \frac{-\Gamma_{ref}\Gamma_{test}m_{13}m_{32}m_{44} + \Gamma_{ref}\Gamma_{test}m_{13}m_{34}m_{42}}{\Gamma_{test}m_{33} + \Gamma_{ref}m_{44} - \Gamma_{ref}\Gamma_{test}m_{33}m_{44} + \Gamma_{ref}\Gamma_{test}m_{34}m_{43} - 1} \\
& + \frac{\Gamma_{ref}\Gamma_{test}m_{14}m_{32}m_{43} - \Gamma_{ref}\Gamma_{test}m_{14}m_{33}m_{42}}{\Gamma_{test}m_{33} + \Gamma_{ref}m_{44} - \Gamma_{ref}\Gamma_{test}m_{33}m_{44} + \Gamma_{ref}\Gamma_{test}m_{34}m_{43} - 1}
\end{aligned} \tag{A.61}$$

$$\begin{aligned}
S_{22} = & -\frac{m_{22} - \Gamma_{test}m_{22}m_{33} + \Gamma_{test}m_{23}m_{32} - \Gamma_{ref}m_{22}m_{44}}{\Gamma_{test}m_{33} + \Gamma_{ref}m_{44} - \Gamma_{ref}\Gamma_{test}m_{33}m_{44} + \Gamma_{ref}\Gamma_{test}m_{34}m_{43} - 1} \\
& + \frac{\Gamma_{ref}m_{24}m_{42} + \Gamma_{ref}\Gamma_{test}m_{22}m_{33}m_{44} - \Gamma_{ref}\Gamma_{test}m_{22}m_{34}m_{43}}{\Gamma_{test}m_{33} + \Gamma_{ref}m_{44} - \Gamma_{ref}\Gamma_{test}m_{33}m_{44} + \Gamma_{ref}\Gamma_{test}m_{34}m_{43} - 1} \\
& + \frac{-\Gamma_{ref}\Gamma_{test}m_{23}m_{32}m_{44} + \Gamma_{ref}\Gamma_{test}m_{23}m_{34}m_{42}}{\Gamma_{test}m_{33} + \Gamma_{ref}m_{44} - \Gamma_{ref}\Gamma_{test}m_{33}m_{44} + \Gamma_{ref}\Gamma_{test}m_{34}m_{43} - 1} \\
& + \frac{\Gamma_{ref}\Gamma_{test}m_{24}m_{32}m_{43} - \Gamma_{ref}\Gamma_{test}m_{24}m_{33}m_{42}}{\Gamma_{test}m_{33} + \Gamma_{ref}m_{44} - \Gamma_{ref}\Gamma_{test}m_{33}m_{44} + \Gamma_{ref}\Gamma_{test}m_{34}m_{43} - 1}
\end{aligned} \tag{A.62}$$

A.2. Measured parameters of the WR90 interferometer (180° hybrid coupler)

The 180° hybrid coupler used for the experimental verification of the proposed calibration technique was measured using four port VNA R&S ZVA67. VNA was calibrated using TRL technique on the reference plane of the WR90 waveguide.

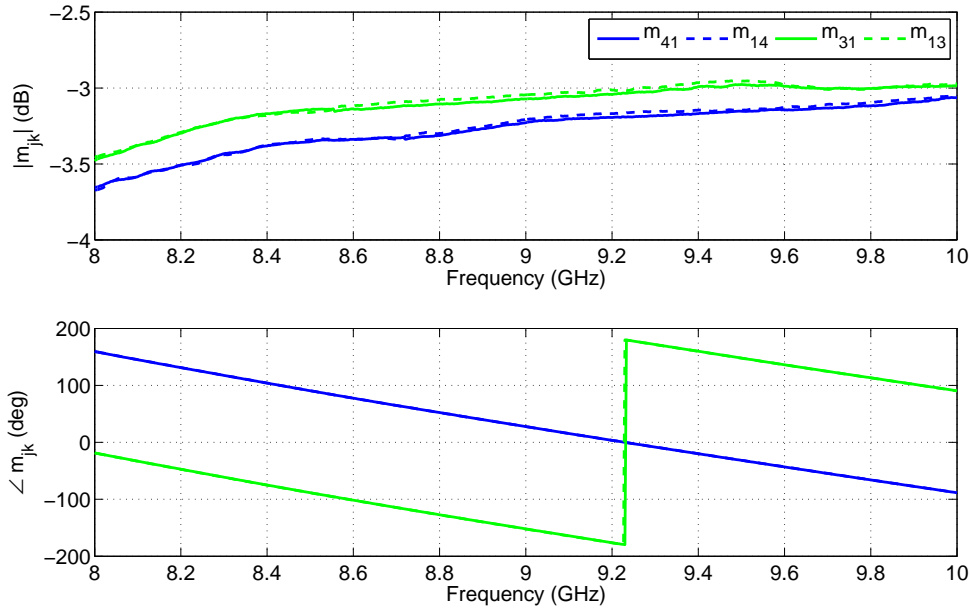


Figure A.43. Parameters m_{41} and m_{31} , magnitude and phase

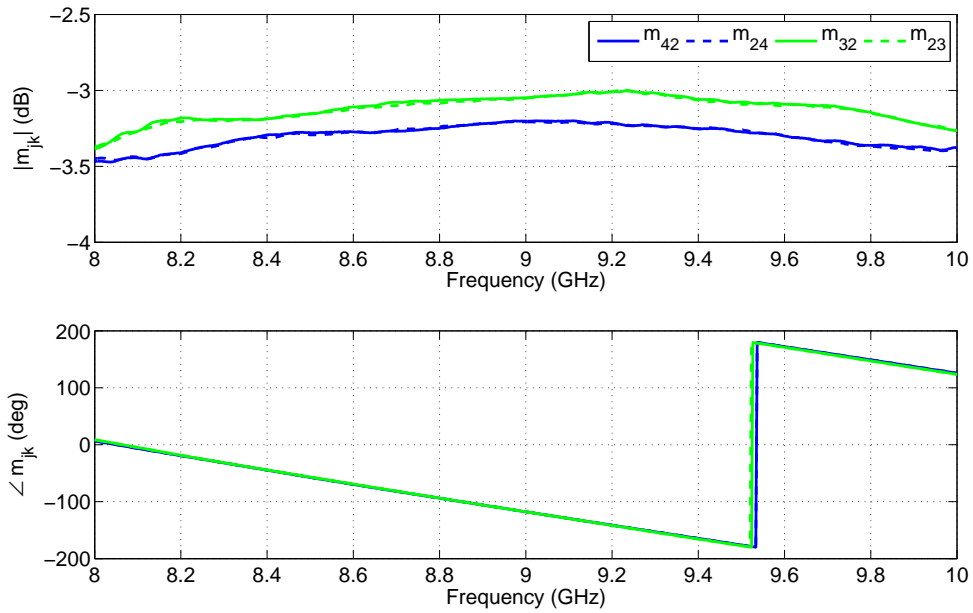


Figure A.44. Parameters m_{42} and m_{32} , magnitude and phase

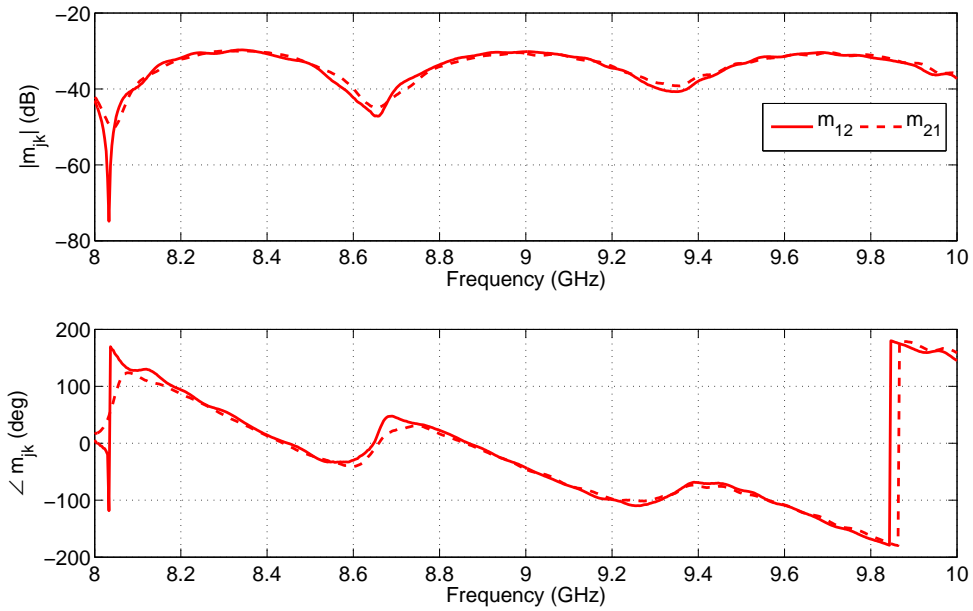


Figure A.45. Cross-talk m_{12} and m_{21} , magnitude and phase

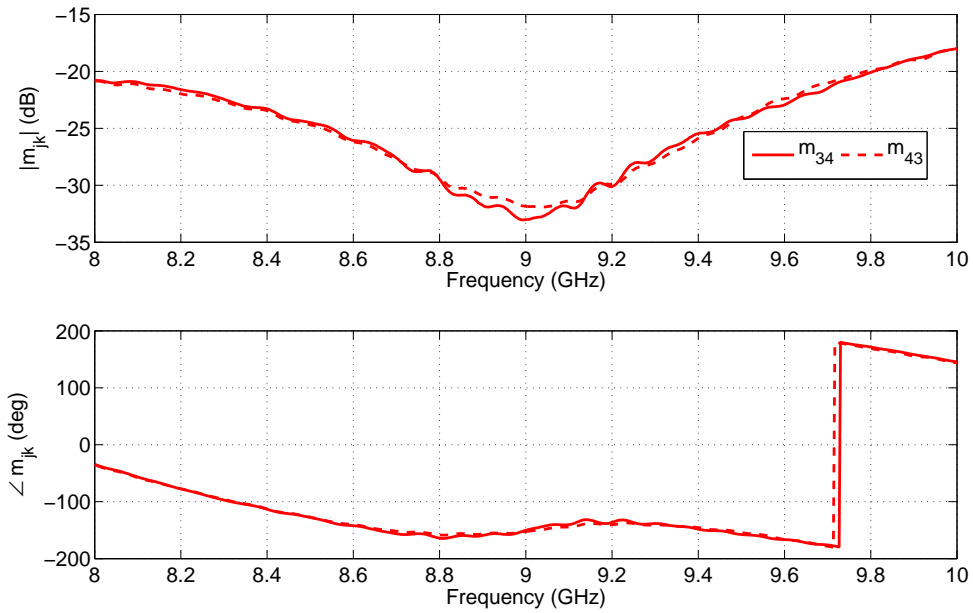


Figure A.46. Cross-talk m_{34} and m_{43} , magnitude and phase

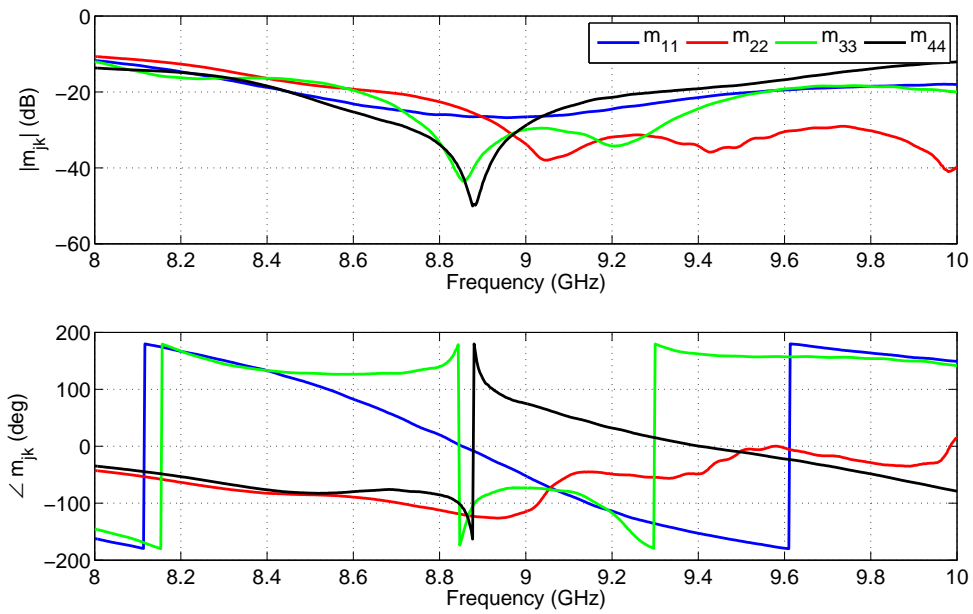


Figure A.47. Reflections m_{11} , m_{22} , m_{33} , m_{44} , magnitude and phase

A.3. Measured S-parameters for each setup

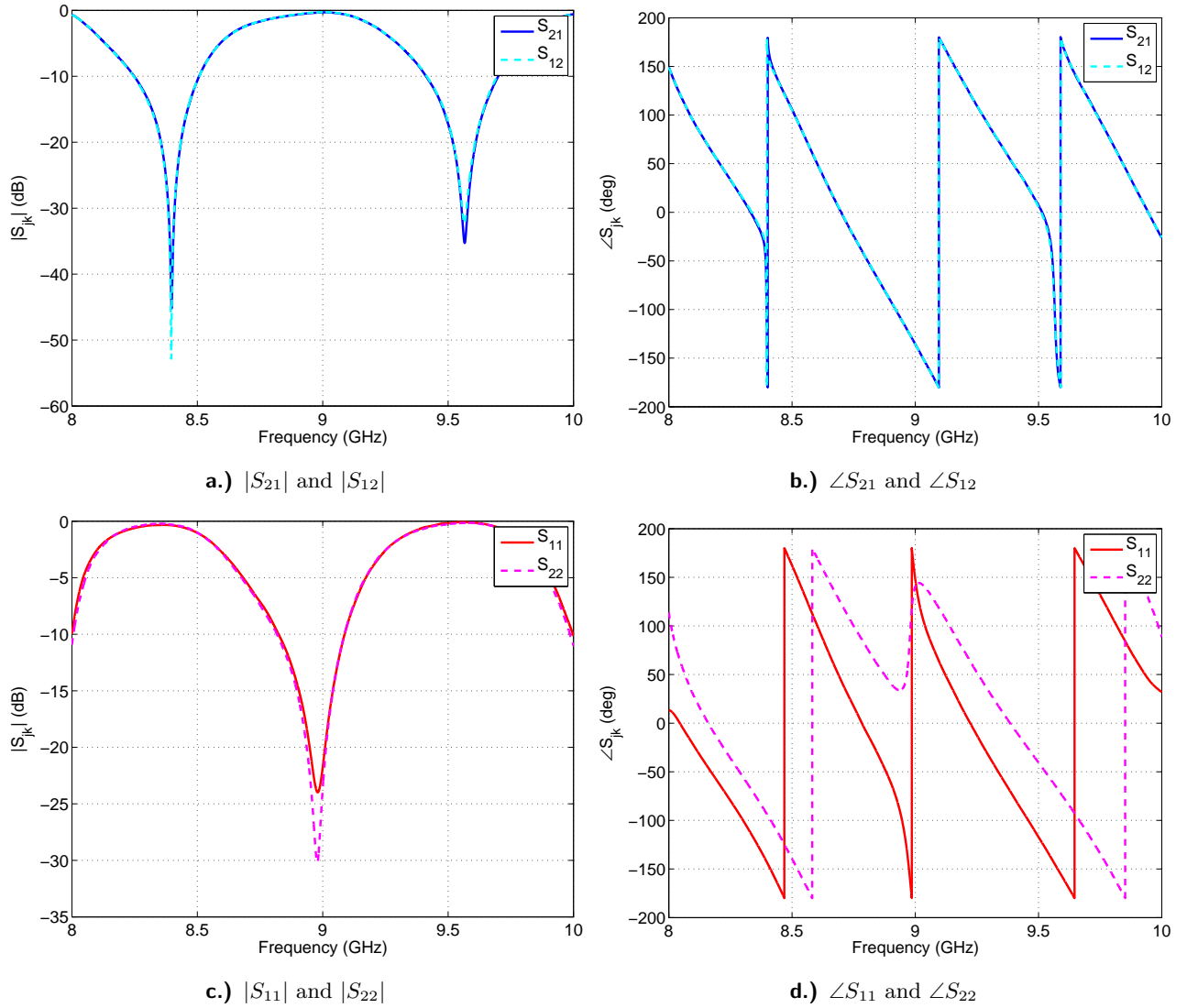
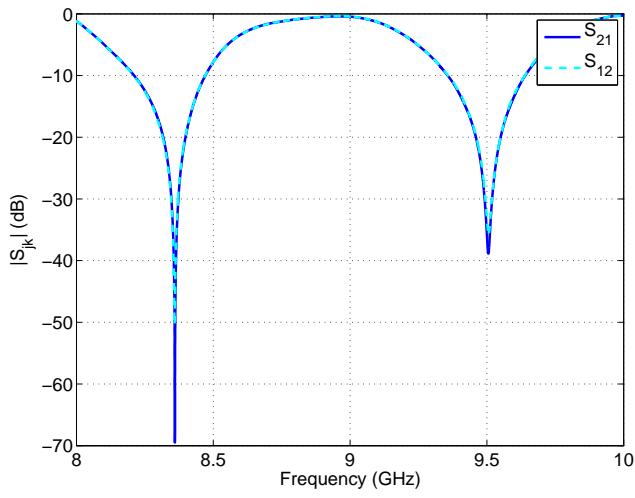
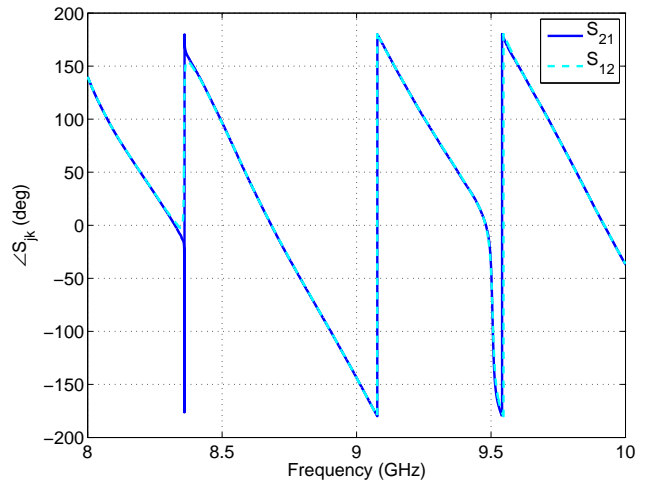


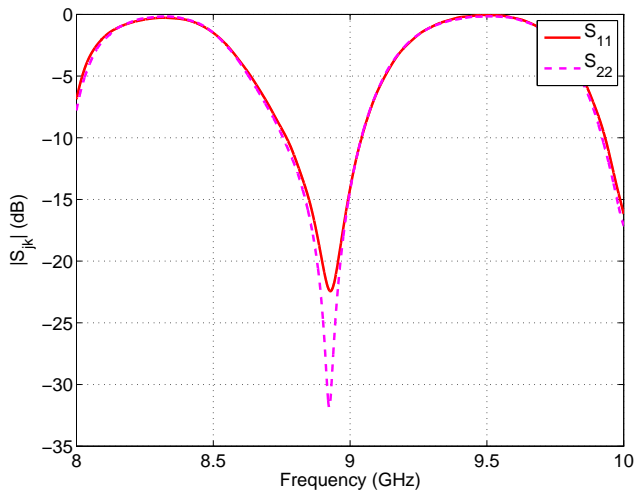
Figure A.48. Setup 1. Four measured S-parameters.



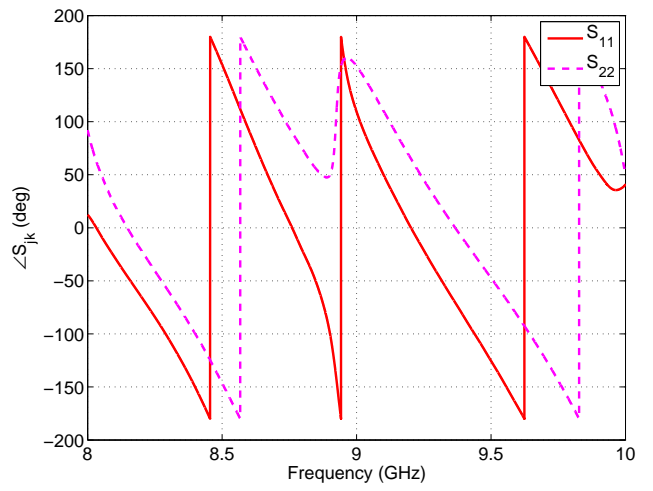
a.) $|S_{21}|$ and $|S_{12}|$



b.) $\angle S_{21}$ and $\angle S_{12}$

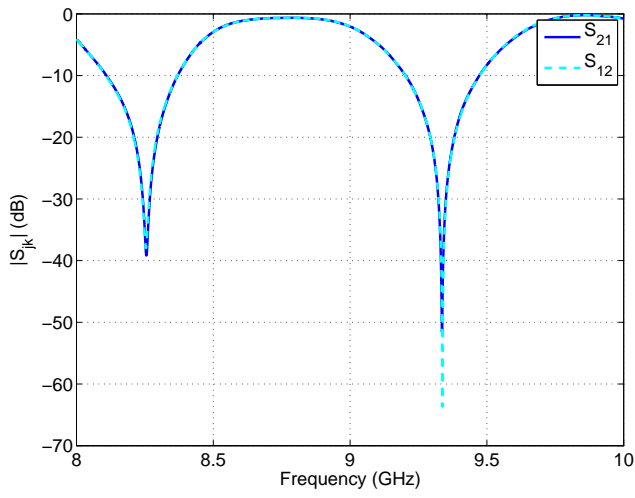


c.) $|S_{11}|$ and $|S_{22}|$

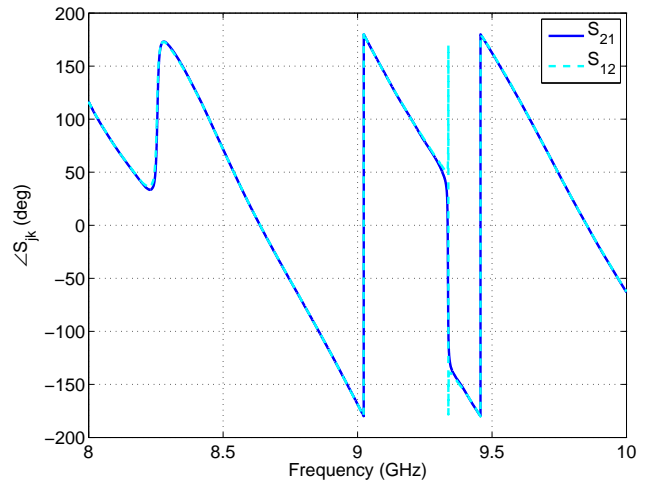


d.) $\angle S_{11}$ and $\angle S_{22}$

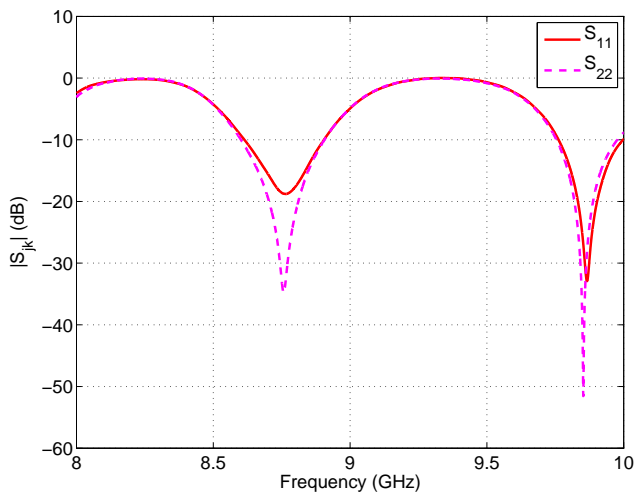
Figure A.49. Setup 2. Four measured S-parameters.



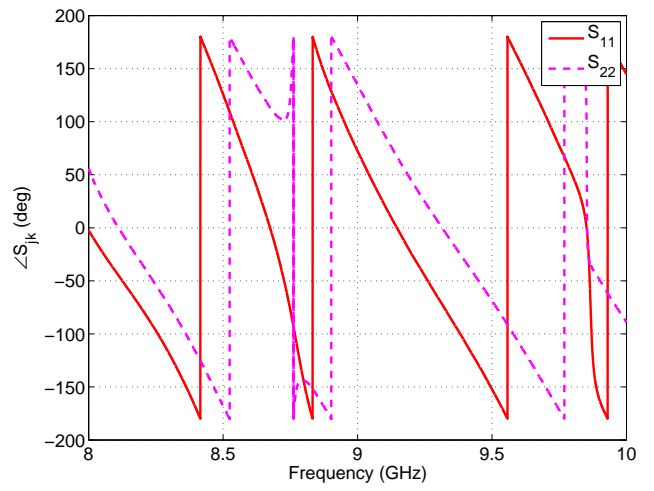
a.) $|S_{21}|$ and $|S_{12}|$



b.) $\angle S_{21}$ and $\angle S_{12}$

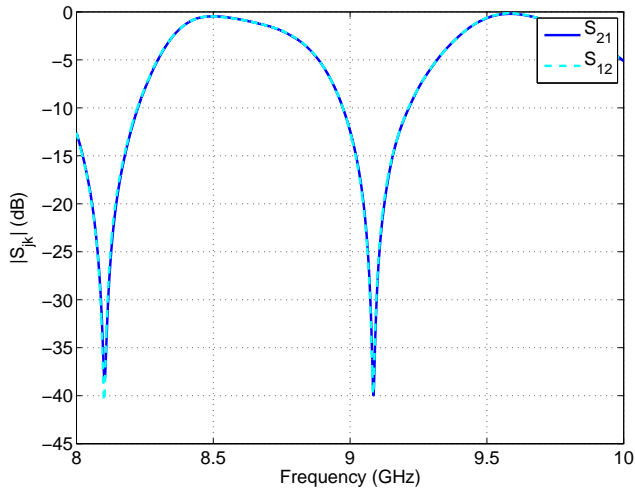


c.) $|S_{11}|$ and $|S_{22}|$

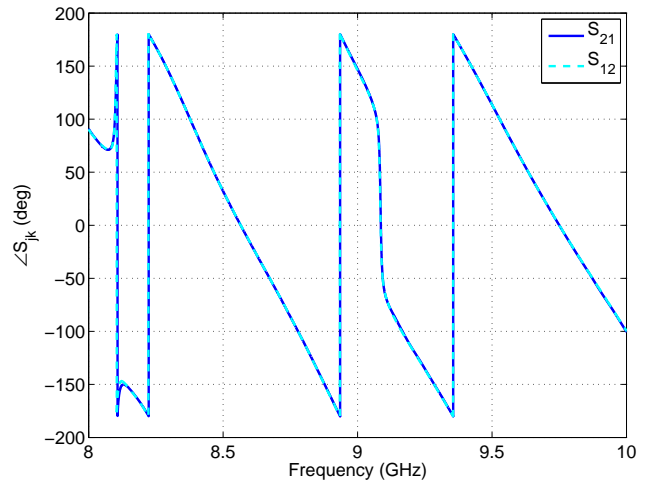


d.) $\angle S_{11}$ and $\angle S_{22}$

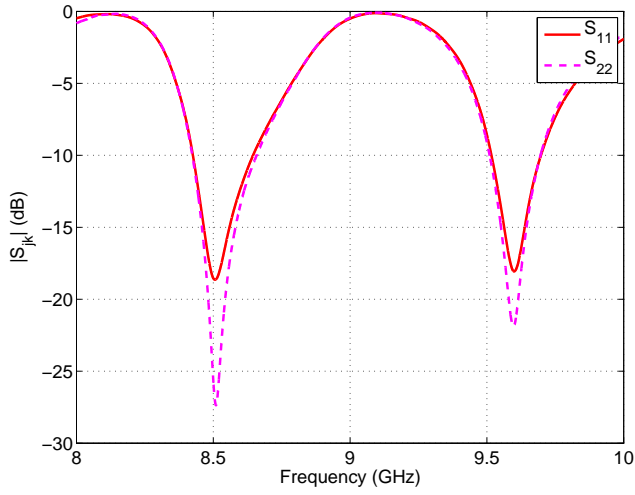
Figure A.50. Setup 3. Four measured S-parameters.



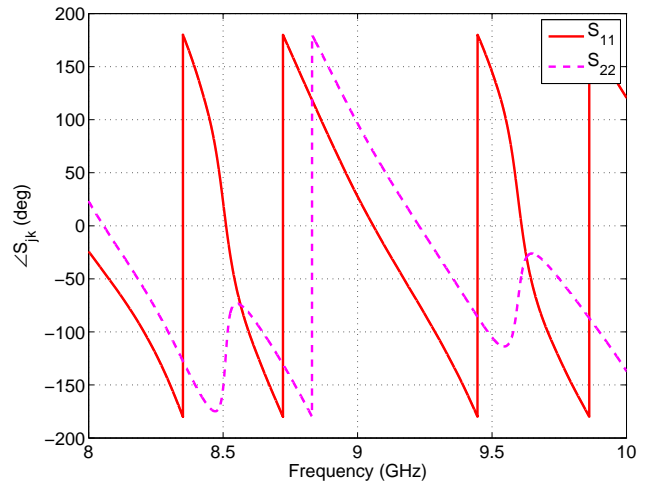
a.) $|S_{21}|$ and $|S_{12}|$



b.) $\angle S_{21}$ and $\angle S_{12}$

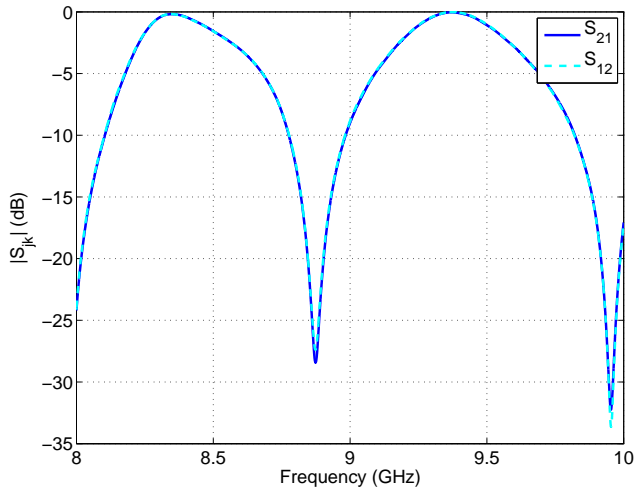


c.) $|S_{11}|$ and $|S_{22}|$

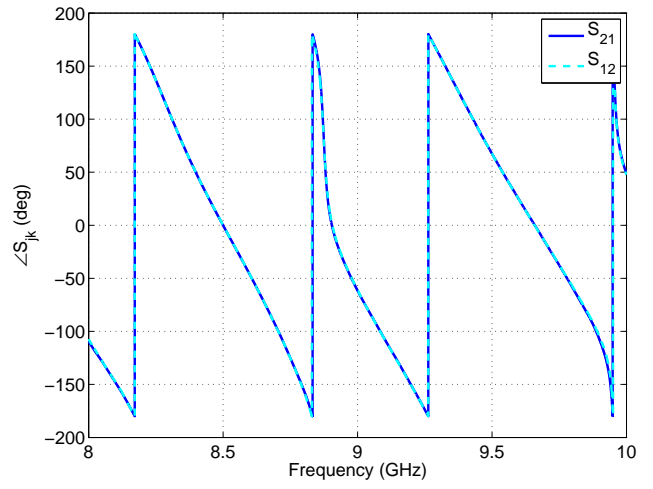


d.) $\angle S_{11}$ and $\angle S_{22}$

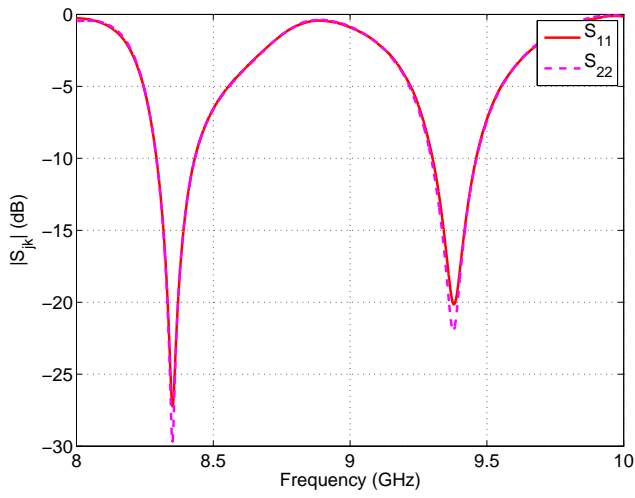
Figure A.51. Setup 4. Four measured S-parameters.



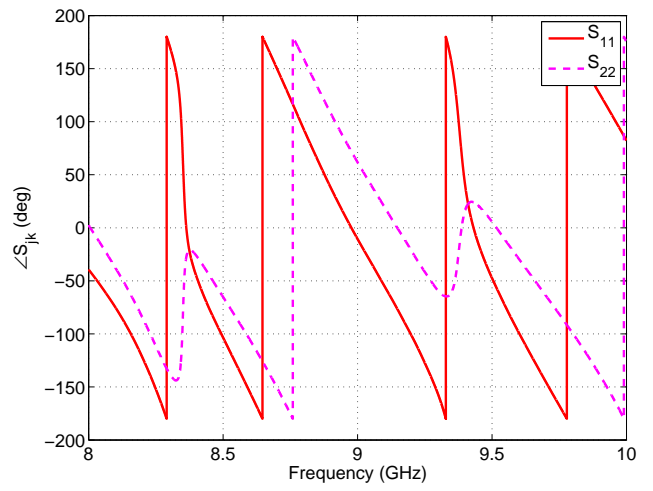
a.) $|S_{21}|$ and $|S_{12}|$



b.) $\angle S_{21}$ and $\angle S_{12}$

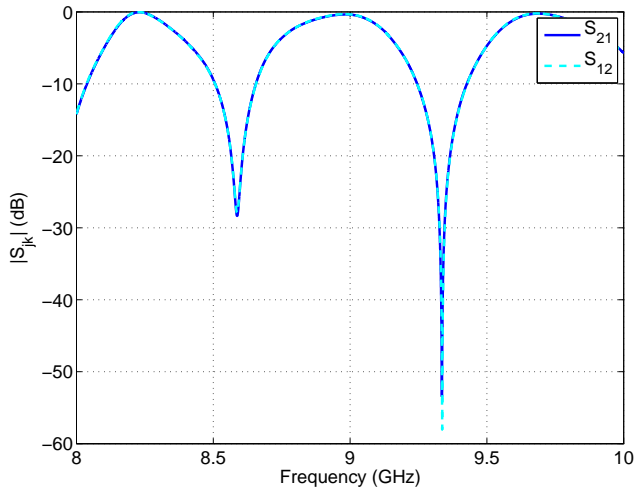


c.) $|S_{11}|$ and $|S_{22}|$

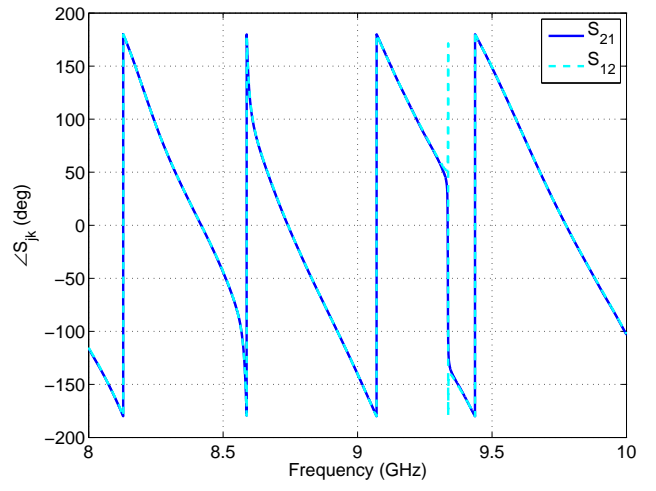


d.) $\angle S_{11}$ and $\angle S_{22}$

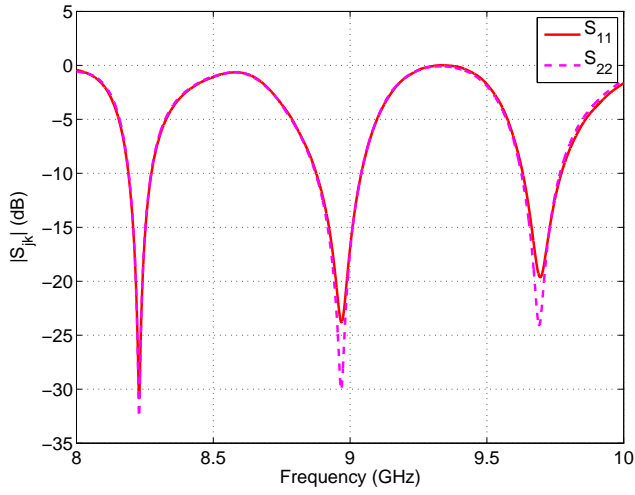
Figure A.52. Setup 5. Four measured S-parameters.



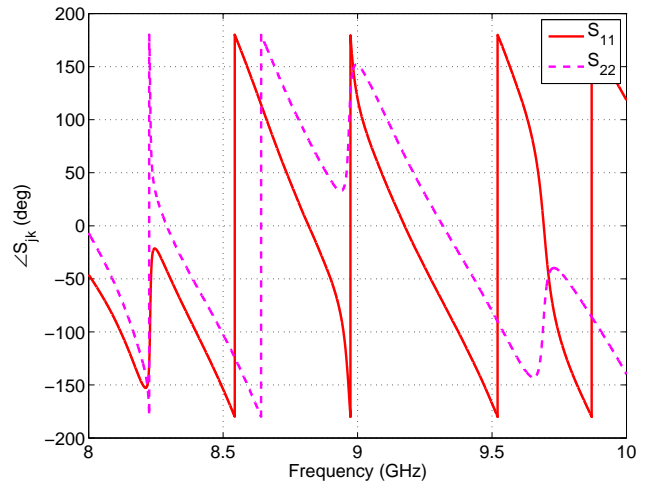
a.) $|S_{21}|$ and $|S_{12}|$



b.) $\angle S_{21}$ and $\angle S_{12}$

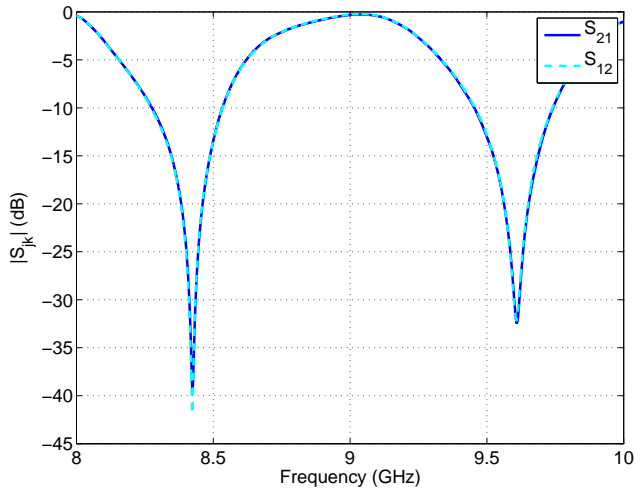


c.) $|S_{11}|$ and $|S_{22}|$

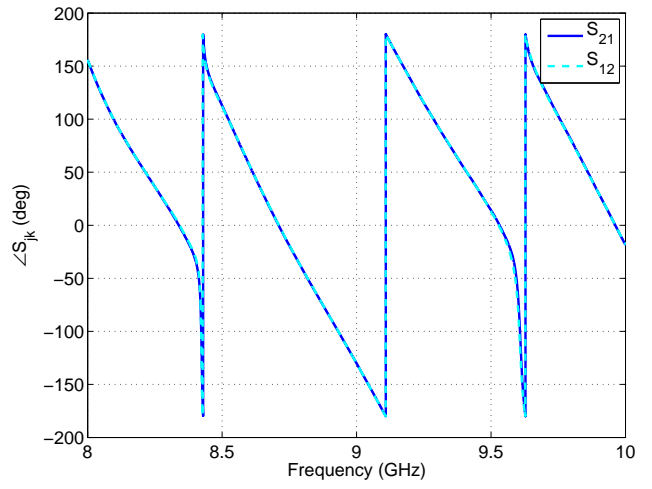


d.) $\angle S_{11}$ and $\angle S_{22}$

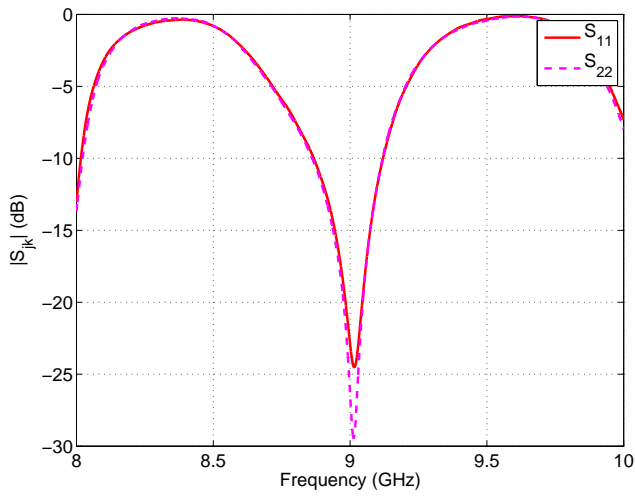
Figure A.53. Setup 6. Four measured S-parameters.



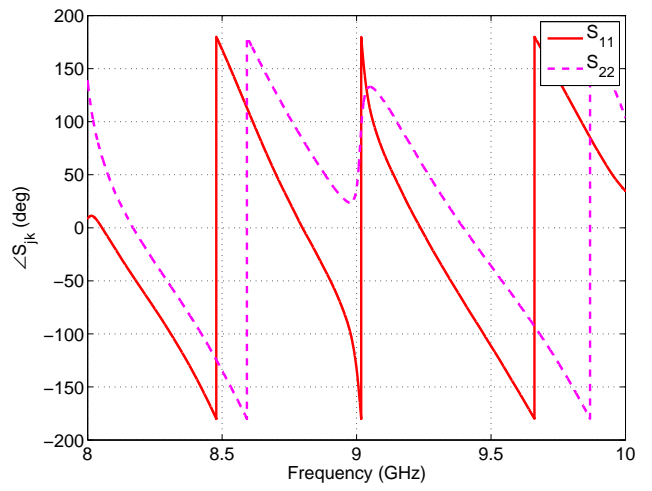
a.) $|S_{21}|$ and $|S_{12}|$



b.) $\angle S_{21}$ and $\angle S_{12}$



c.) $|S_{11}|$ and $|S_{22}|$



d.) $\angle S_{11}$ and $\angle S_{22}$

Figure A.54. Setup 7. Four measured S-parameters.

A.4. Calibration results

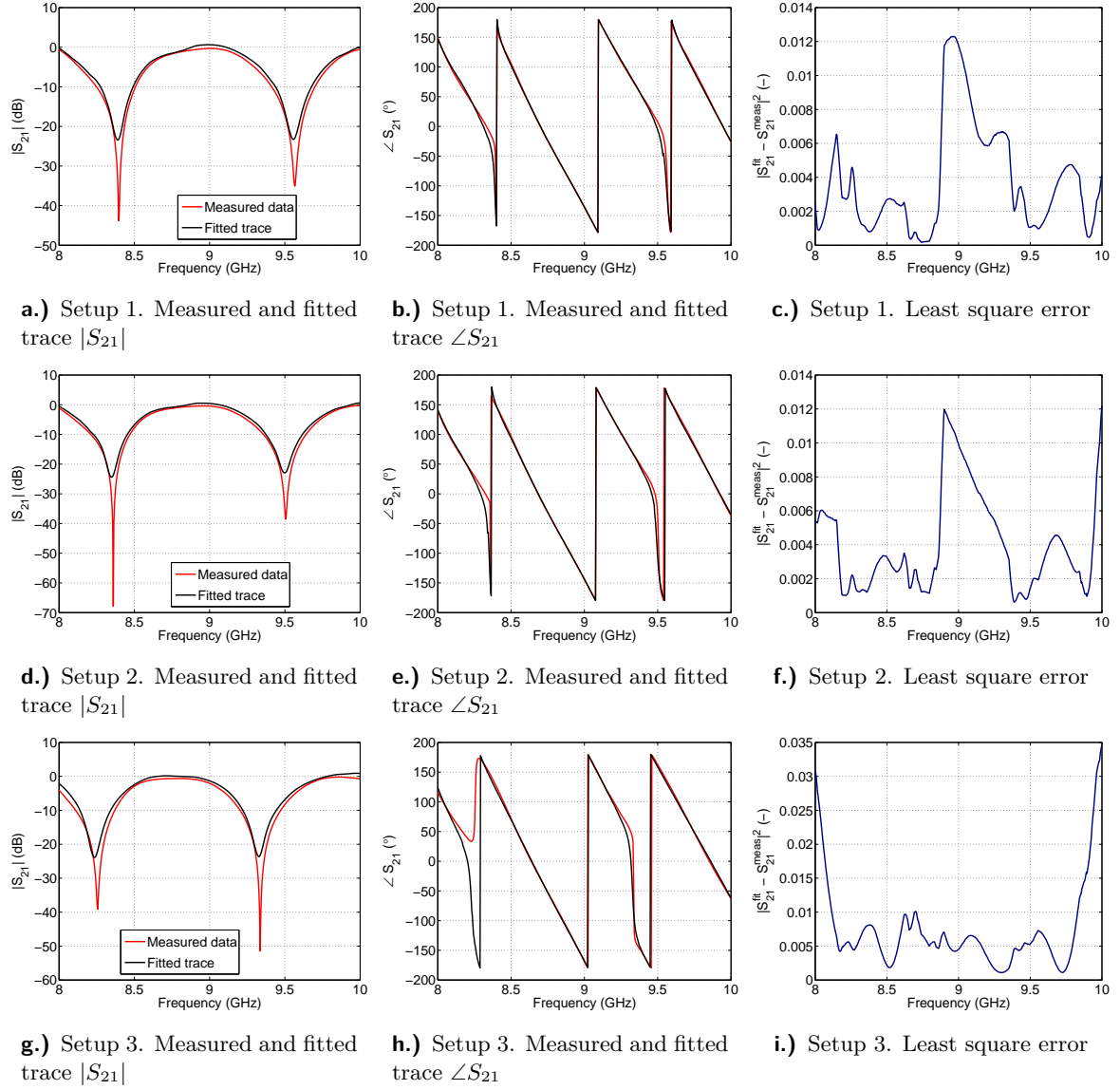


Figure A.55. Measured S_{21} and fitted trace obtained from the calibration and corresponding least square error.

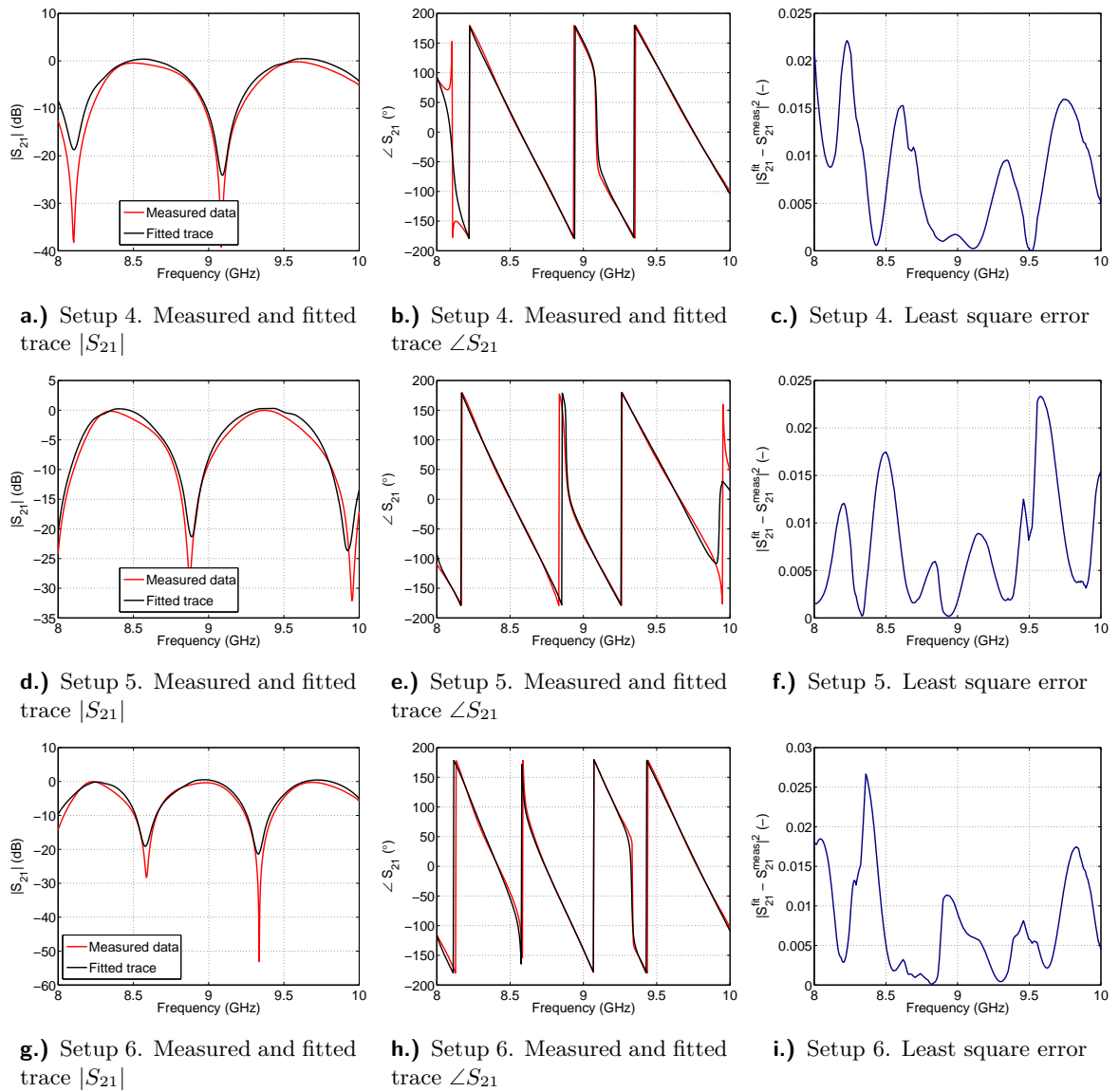
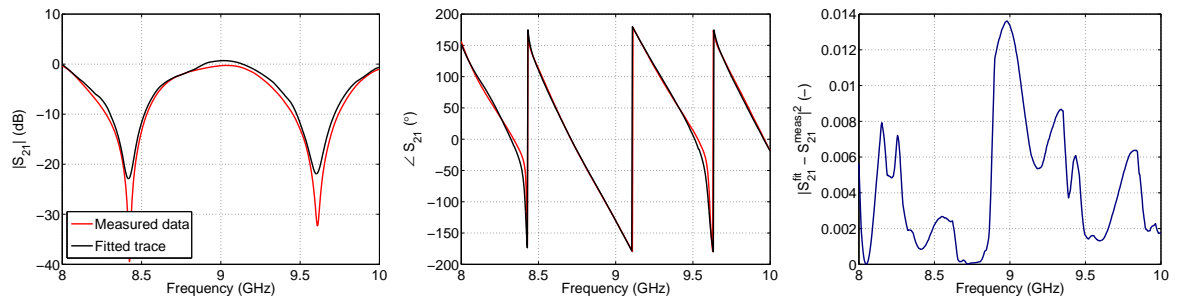


Figure A.56. Measured S_{21} and fitted trace obtained from the calibration and corresponding least square error.



a.) Setup 7. Measured and fitted trace $|S_{21}|$ b.) Setup 7. Measured and fitted trace $\angle S_{21}$ c.) Setup 7. Least square error

Figure A.57. Measured S_{21} and fitted trace obtained from the calibration and corresponding least square error.

Appendix B.

List of candidates's works relating to the doctoral thesis

B.1. Publications in impacted journals

- **M. Prihoda** and K. Hoffmann, "Self-calibrating evaluation method for microwave interferometry measurements," in Electronics Letters, vol. 49, no. 5, pp. 356-358, February 28 2013.
doi: 10.1049/el.2012.3122
author contribution: 50%

B.2. Publications in WOS database

none

B.3. Peer-reviewed publications

- K. Hoffmann, Z. Skvor and **M. Prihoda**, "Precise microwave measurement of liquid level," Microwave Measurement Conference (ARFTG), 2012 79th ARFTG, Montreal, QC, 2012, pp. 1-2.
doi: 10.1109/ARFTG79.2012.6291194
author contribution: 34%

B.4. Other publications

none

B.5. Responses and citations

none